Measurement of the Lifetimes of $D+_3$ and $D+$ Mesons in High Energy Photoproduction

By

John DeAndrea Cunningham, B.S.

LIBOFFCE
FERMILAB
THESIS

E-687

A MEASUREMENT OF THE LIFETIMES OF D_s^+ AND D^+ MESONS IN HIGH ENERGY PHOTOPRODUCTION

A Dissertation

Submitted to the Graduate School
of the University of Notre Dame
in Partial Fulfillment of the Requirements
for the Degree of

Doctor of Philosophy

by

John DeAndrea Cunningham, B.S.

Director

Department of Physics
Notre Dame, Indiana

November, 1990

A0031672

FERMILAB
LIBRARY

A MEASUREMENT OF THE LIFETIMES OF

D_s^+ AND D^+ MESONS

IN HIGH ENERGY PHOTOPRODUCTION

Abstract

by

John DeAndrea Cunningham, B.S.

Measurements of the lifetimes of the D_s^+ and D^+ mesons are described. Both charmed mesons are observed to decay to the state $\phi^0\pi^+$. The data were obtained in Fermilab experiment E687, a photoproduction experiment with a mean photon energy of 220 GeV. The lifetimes were obtained by using a maximum likelihood technique on an event by event basis for the mass and proper time. This measurement produced a D_s^+ lifetime of $0.50 \pm 0.06 \pm 0.03$ picoseconds and a D^+ lifetime of $0.90 \pm 0.10 \pm 0.05$ picoseconds. (The first error is statistical error, while the second is systematic error.) Another decay mode of the D_s^+ meson, where the D_s^+ decays to $\phi^0\pi^+\pi^-\pi^+$, was also observed. The branching fraction of this mode relative to the $D_s^+ \rightarrow \phi^0\pi^+$ mode was measured to be $0.58 \pm 0.20 \pm 0.10$. An upper limit for this ratio was determined for the D^+ mode of $\phi^0\pi^+\pi^-\pi^+$ compared to $D^+ \rightarrow \phi^0\pi^+$ of 0.60 (90% confidence level). The lifetime and branching ratio measurements are compared to other experimental results as well as the theoretical considerations.

TO MY SISTER DEANN

AND HER MANY ACHIEVEMENTS

TABLE OF CONTENTS

LIST OF FIGURES vi

LIST OF TABLES xi

ACKNOWLEDGEMENTS xiv

1 INTRODUCTION 1

1.1 The Photoproduction of Charm 2

1.1.1 Vector Meson Dominance 2

1.1.2 Photon-Gluon Fusion 3

1.2 Weak Decay of Charmed Mesons 4

1.3 Charmed Meson Lifetime Measurements in E687 14

2 BEAM LINE AND SPECTROMETER 15

2.1 The Photon Beam 15

2.1.1 The Accelerator 16

2.1.2 Beam Transport 17

2.2 E687 Spectrometer 24

2.2.1 Beam Tagging System 26

2.2.2 Targets 28

2.2.3 Trigger Counters 30

2.2.4 The Microstrip Detector 32

2.2.5 Analyzing Magnets and PWC's 33

2.2.6 Čerenkov Counters 34

3 THE DATA SET 43

3.1 Data Run 43

3.1.1 Spectrometer and Beam Conditions 43

3.1.2 Triggering 44

3.2 Data Acquistion 47

3.3 Data Reconstruction 49

3.3.1 PASS1 49

3.3.2 Microstrip Tracking 50

3.3.3 PWC Tracking 51
3.3.4 Momentum Analysis 52
3.3.5 Linking Algorithm 52
3.3.6 Čerenkov Algorithm 53

4 DATA ANALYSIS 56
4.1 Data Reduction 56
4.1.1 E687 Skim Routines 57
4.1.2 ϕ^0 Skim 58
4.2 Signal Extraction 61
4.2.1 Vertex Considerations 62
4.2.2 Kinematic Requirement 68
4.3 Signal Study 72
4.4 Efficiency Study 81

5 LIFETIME ANALYSIS 87
5.1 Lifetime Measurement Technique 87
5.1.1 Maximum Likelihood Method 87
5.1.2 Construction of the Likelihood Function 90
5.2 Lifetime Measurement Results 109
5.2.1 The Standard Function 110
5.2.2 $f(t_i)$ Study 111
5.2.3 Single Exponential Background 116
5.2.4 Parameterization in t' 118
5.2.5 Comparison of Results 121
5.3 Errors in the Lifetime Results 125
5.3.1 Statistical Errors 125
5.3.2 Systematic Errors 127
5.3.3 Conclusions 133

6 BRANCHING RATIO ANALYSIS 138
6.1 Analysis Cuts 138
6.2 Branching Ratio Analyses 143
6.2.1 $\mathrm{BR}(D_s^+ \to \phi^0\pi^+\pi^-\pi^+)/\mathrm{BR}(D_s^+ \to \phi^0\pi^+)$ Measurement . . . 143
6.2.2 $\mathrm{BR}(D^+ \to \phi^0\pi^+\pi^-\pi^+)/\mathrm{BR}(D^+ \to \phi^0\pi^+)$ Measurement . . . 145

7 CONCLUSIONS 147
7.1 Recapitulation of Results 147
7.2 Comparisons to Other Measurements 148
7.2.1 Lifetimes 148
7.2.2 Branching Ratios 151

7.3 Final Comments 152

BIBLIOGRAPHY 153

LIST OF FIGURES

1.1 Diagram of Vector Meson Dominance. 3

1.2 Lowest Order Diagram of Photon-Gluon Fusion. 4

1.3 Spectator Diagram of the D_s^+ meson. 5

1.4 Spectator Diagram of the D^+ meson. 5

1.5 Weak Decay Mechanisms of Charmed Mesons 7

1.6 Spectator Diagrams (lowest order) for D^0, D_s^+ and D^+ Mesons. . . . 9

1.7 Lowest Order Diagrams for Charm Decays 11

2.1 Beamlines at Fermilab. 18

2.2 The Steps to Produce Photons from Protons 21

2.3 Electron Beam Energy Distribution 23

2.4 Photon Spectrum from 350 GeV/c Electrons. 23

2.5 Tagged Photon Spectrum. 24

2.6 The E687 Spectrometer 25

2.7 The E687 Target and Microstrip Region 26

2.8 A Schematic of the 5 Stack Beryllium Target. 29

2.9 Z-coordinate Vertex Positions for each of the Three Target Configurations 31

2.10 A Schematic of C2 (view from above). 36

2.11 Schematic of 2 Inch Tube Base Design Used on Thorn EMI 9939A PMTs. 37

2.12 Schematic of 5 inch Tube Base Design Used on RCA 8854 PMTs. . . 38

2.13 Photographic Survey Results Showing the Cell/Cone Structure of C2. 40

3.1 Trigger and Readout Schematic 48

4.1 Kaon Identification as a Function of Momentum 59

4.2 Phi Meson Study 60

4.3 The $\phi\pi^+$ Invariant Mass. 62

4.4 Distribution of L/σ_L 64

4.5 Separation between Primary and Secondary Vertices 65

4.6 Secondary Vertex Z-coordinate Position 66

4.7 Distribution of χ^2/DOF for the Secondary Vertices. 67

4.8 The cosθ Distributions 69

4.9 $\phi^0\pi^+$ Mass Distributions with and without a Cosθ Cut 70

4.10 Fitted $\phi\pi^+$ Invariant Mass Distributions for Various L/σ_L Cuts. . . 70

4.11 Proper Time Distributions 73

4.12 Multiplicity of Charged Tracks in the PWC's. 74

4.13 Multiplicity of Charged Tracks in the Microstrip Detector. 75

4.14 Multiplicity of Charged Tracks at the Primary Vertex. 76

4.15 L and σ_L for D_s^+ and D^+ Samples. 77

4.16 Momentum Distributions of D_s^+ and D^+ Events. 78

4.17 Resulting ϕ^0 Mass after Cuts. 78

4.18 RESH Photon Energy Distributions 79

4.19 A Comparison of Charged Modes 80

4.20 Comparisons between Data and Monte Carlo Event Samples 83

4.21 Momentum Distribution of D_s^+ Comparing Data to Monte Carlo . . 84

4.22 Comparisons in D_s^+ Mass Resolution in Data and MC 84

5.1 The Background Mass Region (1.75 GeV/c^2 to 1.85 GeV/c^2) Proper Times Fit to Three Different Functions. 92

5.2 The Background Event Time Distribution for Four Mass Regions ($L/\sigma_L > 3$) Fit to a Double Exponential. 93

5.3 Proper Time Distribution of Monte Carlo Events and of Background Events from the Data. 95

5.4 Monte Carlo Data with Maximum Likelihood Fits Using an Exponential Distribution and a Gaussian Distribution. 95

5.5 Monte Carlo Events with the Maximum Likelihood Fit Using a Sum of Two Exponentials 96

5.6 Input Monte Carlo Proper Time Distribution. 99

5.7 Decays in the Target Region. 99

5.8 The X-, Y- coordinate Positions of Tracks at the Secondary Vertex and at the Exit of the Target for each Target. 102

5.9 The Probability of Survival (No Absorption) as a Function of Proper Time in the 5BE Target. 103

5.10 The Probability of Survival (No Absorption) as a Function of Proper Time in the SILI Target. 103

5.11 Efficiency Study (Part I) 105

5.12 Efficiency Study (Part II) 106

5.13 Proper Time Acceptance Functions for all 3 Target Configurations. . 107

5.14 MINUIT Command File 109

5.15 Fits to the Data ($f(t_i)$ included and double exponential background proper time parameterization.) 112

5.16 Fits to Background Proper Times ($f(t_i)$ included and double exponential background proper time parameterization.) 113

5.17 Fits to the Data ($f(t_i)$ removed and double exponential background proper time parameterization.) 114
5.18 Fits to Background Proper Times ($f(t_i)$ removed and double exponential background proper time parameterization.) 115
5.19 Fits to the Data ($f(t_i)$ included and single exponential background proper time parameterization.) 117
5.20 Fits to Background Proper Times ($f(t_i)$ included and single exponential background proper time parameterization.) 118
5.21 Error in the Proper Time as a Function of Proper Time. 119
5.22 Fits to the Data in t' ($f(t_i)$ removed and double exponential background proper time.) 120
5.23 Fits to Background Proper Times in t' ($f(t_i)$ removed and double exp. background proper time.) 121
5.24 Distribution of The Difference between Input and Reconstructed Proper Times for Monte Carlo Data. 126
5.25 Calculated D_s^+ Lifetimes from Monte Carlo. 128
5.26 Calculated D_s^+ Lifetimes from Monte Carlo with $f(t_i)$ Correction. . . 129
5.27 $\phi^0\pi^+$ Mass Plots with Higher Values of L/σ_L 130
5.28 D_s^+ Lifetime Measurements for High L/σ_L Values (background ignored). 131
5.29 D^+ Lifetime Measurements for High L/σ_L Values (background ignored). 131
5.30 Calculated D_s^+ Lifetimes of Different Mass Ranges and Values of L/σ_L 132
5.31 Calculated D^+ Lifetimes of Different Mass Ranges and Values of L/σ_L 134

5.32 Calculated D_s^+ and D^+ Lifetimes as a Function of Z-coordinate Decay Limits. 135

5.33 D_s^+ Lifetimes as a Function of L/σ_L cut (full fit). 136

5.34 D^+ Lifetimes as a Function of L/σ_L cut (full fit). 136

6.1 Fitted Invariant Mass Plot of $\phi^0\pi^+\pi^-\pi^+$ Events as a Function of the L/σ_L Cut. 140

6.2 Fitted Invariant Mass Plot of $\phi^0\pi^+\pi^-\pi^+$ (D^+ mass and signal width constrained). 142

LIST OF TABLES

1.1 CURRENT WORLD LIFETIME AVERAGES 8

1.2 D_s^+ WORLD LIFETIME AVERAGES 10

2.1 WIDE BAND BEAM PROPERTIES 22

2.2 CHARACTERISTICS OF THE MICROSTIP DETECTOR 32

2.3 MAGNET PROPERTIES 33

2.4 ČERENKOV COUNTER PROPERTIES 35

2.5 PHOTOELECTRON YIELD FOR EACH CELL 42

3.1 BUSLINE ASSIGNMENTS 46

3.2 ČERENKOV MOMENTUM REGIONS 54

3.3 ISTATP VALUES AND DEFINITIONS 55

3.4 PARTICLE IDENTIFICATION EFFICIENCIES 55

4.1 SKIM FLAGS AND STREAMS 57

4.2 PHI FIT PARAMETERS 61

4.3 SIGNAL FIT PARAMETERS 71

4.4 CUTS USED TO EXTRACT D_s^+ AND D^+ SIGNALS 71

4.5 EVENT YIELDS AS A FUNCTION OF CUTS 72

4.6 MEAN VALUES OF EVENT CHARACTERISTICS 77

4.7 COMPARISON OF THE YIELDS OF CHARGED MODES 81

4.8 MASS FIT COMPARISON (DATA VS. MC) 85

4.9 EFFICIENCY STUDY 86

5.1 ACCEPTANCE POLYNOMIAL COEFFICIENTS 105

5.2 FIT PARAMETER RESULTS 110

5.3 FIT PARAMETER RESULTS ($f(t_i)$ =1) 115

5.4 FIT PARAMETER RESULTS (single exponential BG proper time function) 116

5.5 FIT PARAMETER RESULTS (t' distribution ($f(t') = 1$; double exp. background)). 122

5.6 COMPARISONS OF 4 FITS 123

5.7 FIT PLOTS 123

5.8 DOF FOR EACH FIT 123

5.9 χ^2/DOF COMPARISONS 124

5.10 FINAL LIKELIHOOD FUNCTION VALUES 124

5.11 LIFETIME RESULT COMPARISONS (IN PICOSECONDS) 124

6.1 $D_s^+ \to \phi^0\pi^+\pi^-\pi^+$ FIT RESULTS 141

6.2 EFFICIENCY STUDY OF $D_s^+ \to \phi^0\pi^+\pi^-\pi^+$ 144

6.3 EVENT COUNT AND EFFICIENCIES FOR D_s^+ 144

6.4 EFFICIENCY STUDY OF $D^+ \to \phi^0\pi^+\pi^-\pi^+$ 146

6.5 EVENT COUNT AND EFFICIENCIES FOR D^+ 146

7.1 LIFETIME RESULTS 147

7.2 BRANCHING RATIO RESULTS 148

7.3 D_s^+ LIFETIME MEASUREMENTS 149

7.4 D^+ LIFETIME MEASUREMENTS 150

7.5 MEASUREMENTS OF $R_1 = \frac{BR(D_s^+ \to \phi^0\pi^+\pi^-\pi^+)}{BR(D_s^+ \to \phi^0\pi^+)}$ 151

7.6 VALUES OF BR($D^+ \to \phi^0\pi^+\pi^-\pi^+$) × BR($\phi^0 \to K^+K^-$) 152

ACKNOWLEDGMENTS

It's been a long journey, but overall I managed to have some fun and meet some great people. I'd like to first thank my parents for both their emotional and financial support. I'd like to thank my sister Connie for her support too.

I want to thank my advisor, Neal Cason, for all of his assistance. He was right–I did enjoy the analysis most. I am also in gratitude to Jerome Busenitz for all he has taught me. His perseverance in completing a goal was an inspiration.

I'd also like to thank all the members of the Notre Dame High Energy group for all of the assistance I have received from them over the years.

I am also grateful to have been a member of the E687 Collaboration. It will always be an asset to have worked with such a gifted group of people.

The greatest gift from this time in graduate school had been numerous friendships. Robert Gardner will always be a close friend. Somewhere in the Florida Everglades he convinced me to return to graduate school and E687. It was valuable advice. To another close friend, Dan Shibata, whose humor and "good times" made graduate school bearable, may our friendship live on as long as N.D. football!

To my favorite Yugoslav couple in the world, Danilo and Liana Pušeljić, I'd like to thank them for all the good times and many great meals. My trip to Yugoslavia will always be a fond memory. Hey–when are we taking Saša to Disney World!?

To all my friends from the "Sorin St. ghetto," I hope our friendships continue regardless of where we end up on this planet. Zeid Ayer and Steve Schwarzbek are

great guys who never let physics get in the way of some fun (and drinking!). I'm grateful to Peter Beery for some great racketball games. His meals (especially those black beans from Brazil) were always a treat.

I do believe! Cash and Mary are a fun couple! I hope our numerous discussions/arguments on politics, economics and religion will continue forever.

My life had also been enriched by friendships with Gregg and Kathi Sturrus, C.W. Bogart, Laura Van Wormer, Charles C. Choo (C^3) and Zeyuan Wu. Thanks for everything!

CHAPTER 1

INTRODUCTION

In this dissertation, a measurement of the lifetimes of the D_s^+ and D^+ mesons is presented. Both of these mesons decay via the $\phi^0\pi^+$ channel. Another decay channel, $\phi^0\pi^+\pi^-\pi^+$, was also studied for both the D_s^+ and D^+ . The ratios of BR($D_s^+ \rightarrow \phi^0\pi^+\pi^-\pi^+$) to BR($D_s^+ \rightarrow \phi^0\pi^+$) and BR($D^+ \rightarrow \phi^0\pi^+\pi^-\pi^+$) to BR($D^+ \rightarrow \phi^0\pi^+$) are also measured.

These charmed particle states were extracted from some 60 million photon-beryllium (γBe) and photon-silicon (γSi) interactions in Fermilab experiment E687. This fixed target experiment was conducted at the terminus of the Fermilab proton line. The data were obtained with an average photon energy of 220 GeV. More details of the mechanics of the experiment are described elsewhere in this thesis.

The theoretical background and motivation for studying these charmed particle states are presented in this chapter. The photoproduction of charmed particles is first studied. The weak decay of these charmed particles is then examined. The chapter is concluded with the advantages experiment E687 has in extracting these charmed particles and measuring their lifetimes.

1.1 The Photoproduction of Charm

In this section the theoretical considerations of how a photon could interact with a nucleus in the target to produce charmed particles are examined. There are two models to explain and quantify this process: Vector Meson Dominance [VDM] and Photon-Gluon Fusion [PGF].

1.1.1 Vector Meson Dominance

The Vector Meson Dominance model [1][2] was the first theoretical model used to explain the photoproduction of hadrons. In this model, the photon has both a hadronic and electromagnetic component. This can be written as,

$$|\gamma\rangle \cong \sqrt{c_1}|\gamma_B\rangle + \sqrt{c_2}|h\rangle, \tag{1.1}$$

where $|\gamma_B\rangle$ is the "bare" photon contribution and $|h\rangle$ is the hadronic contribution. (The constants c_1 and c_2 are normalizing coefficients.) It is clear that the $|h\rangle$ states must have the same quantum numbers as the photon, namely, $J^{PC} = 1^{--}$, $Q = B = S = 0$. Vector mesons, such as the ρ^0, ω^0 and ϕ^0, have these same quantum numbers. This hypothesis seemed credible after observing the copious production of these vector mesons in photoproduction experiments. In VMD, the hadronic component of the photon undergoes normal hadronic interactions with the target. This is shown in Fig. 1.1.

Although formulated before quarks were considered the fundamental constituents of hadrons, VMD was successful in predicting the photoproduction characteristics of the ρ^0, ω^0 and ϕ^0 mesons [2]. With the advent of higher mass quark states containing the charm quark, one could then use the perturbative calculations of quantum chromodynamics (QCD) to predict the behavior of photoproduced final

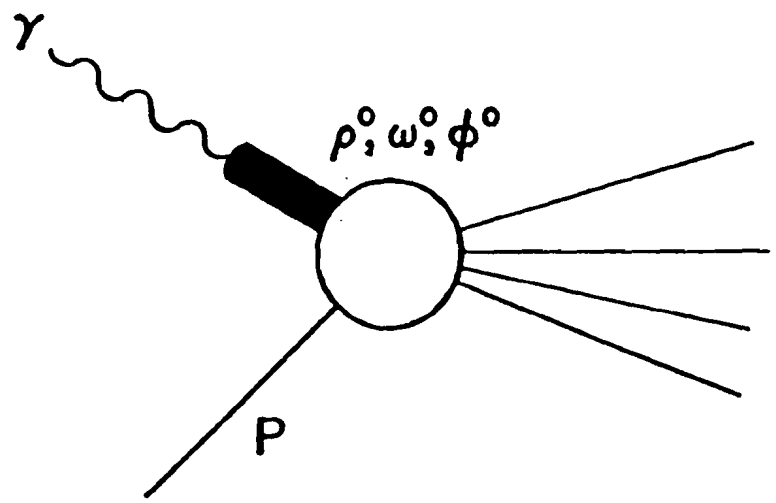

Figure 1.1: Diagram of Vector Meson Dominance.

states. (The low masses of the ρ^0, ω^0 and ϕ^0 mesons made QCD perturbative techniques inappropriate.) Photon-Gluon Fusion uses QCD to calculate the behavior of photoproduced charmed particle states.

1.1.2 Photon-Gluon Fusion

In the second model of photoproduction, Photon-Gluon Fusion [PGF] [3], the charmed particles are produced when the photon couples to a heavy quark antiquark pair and then one of the quarks is scattered by a gluon from the target. The lowest order QCD process exhibiting PGF is shown in Fig.1.2.

The calculations related to quantum electrodynamics (QED) can be calculated for Photon-Gluon Fusion. This is done by substituting the strong coupling constant (α_s) for the electromagnetic coupling constant (α_{em}) at the gluon-quark vertex. Quark charge and color factors must also be implemented [3].

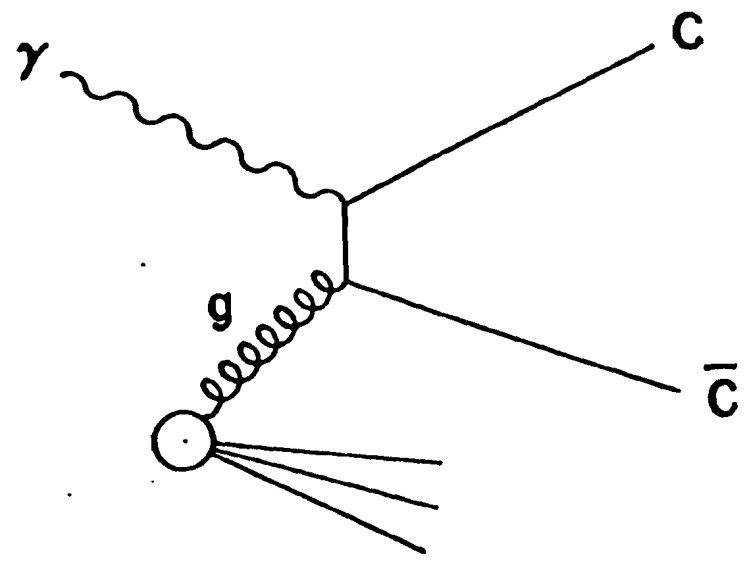

Figure 1.2: Lowest Order Diagram of Photon-Gluon Fusion.

1.2 Weak Decay of Charmed Mesons

If one examines the decay, $D_s^+ \rightarrow \phi^0\pi^+$, at the quark level, a spectator diagram (lowest order) as shown in Fig. 1.3 results. It is called a spectator diagram because the light quark or anti-quark (in this case the strange anti-quark) does not participate in the decay of the charm quark decay process. Similarly the lowest order diagram of the decay, $D^+ \rightarrow \phi^0\pi^+$ is shown in Fig. 1.4.

In both decays, the charm quark decays to a strange quark while emitting a virtual W-boson. This can be understood by studying Cabibbo theory [4]. Cabibbo theory begins by introducing a parameter, θ_c, the quark mixing angle (or Cabibbo angle). In this theory, both the down (d) quark and strange (s) quark are elements of the rotated quark states, d′ and s′, where,

$$d' = d \cdot \cos\theta_c + s \cdot \sin\theta_c \tag{1.2}$$

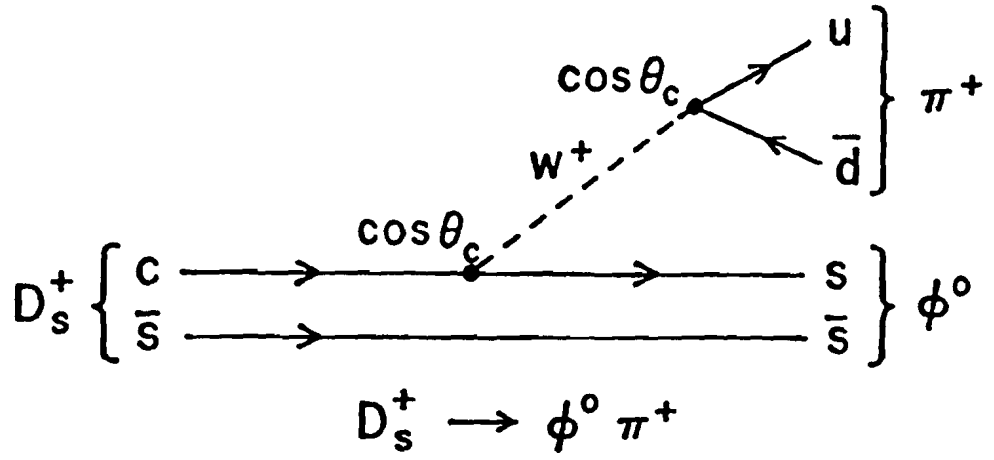

Figure 1.3: Spectator Diagram of the D_s^+ meson.

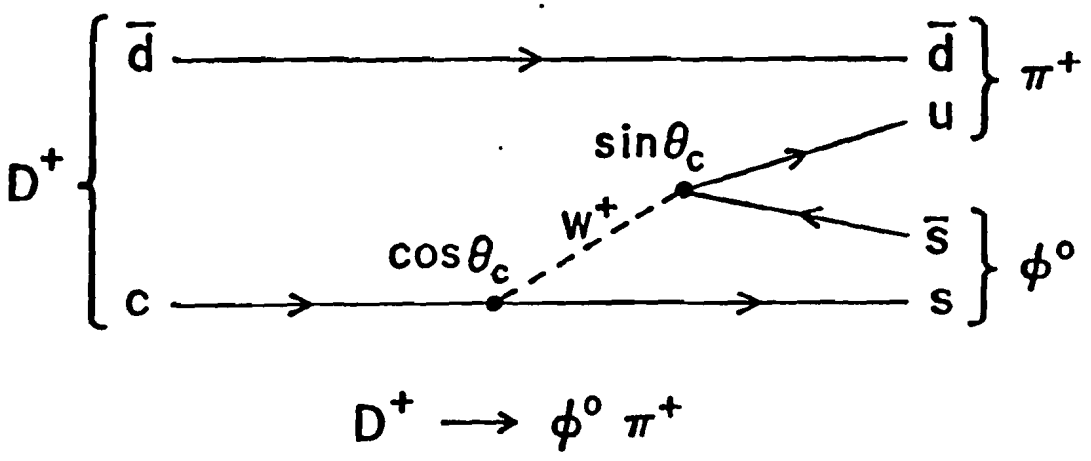

Figure 1.4: Spectator Diagram of the D^+ meson.

and

$$s' = -d \cdot \sin\theta_c + s \cdot \cos\theta_c. \tag{1.3}$$

The value of θ_c has been measured by examining the weak decays of kaons and pions giving a value, $\theta_c \approx 13°$ ($\sin\theta_c \approx 0.22$ and $\cos\theta_c \approx 0.97$). Since $\cos\theta_c$ is greater than $\sin\theta_c$, the amplitudes of those decays proportional to $\cos^2\theta_c$ dominant over those proportional to $\sin^2\theta_c$. The Feynman diagrams in Fig. 1.5(A) and Fig. 1.5(B) are proportional to $\cos\theta_c$ (Cabibbo-favored), while those in Fig. 1.5(C) and Fig. 1.5(D) are proportional to $\sin\theta_c$ (Cabibbo-suppressed). Examination of Fig. 1.3 shows that decay to be Cabibbo-favored, while the decay of Fig. 1.4 is Cabibbo-suppressed.

The theoretical analysis of charmed meson lifetimes began by using the spectator ansatz. As mentioned previously, this ansatz assumes that the charmed quark undergoes β-decay while the light quark does not affect the process. If one assumed that the charmed quark within the hadron decayed in a manner similar to the weak decay of a heavy lepton, the charmed particle lifetimes could be estimated by measuring the muon lifetime.

The decay, $\mu^- \rightarrow e^-\bar{\nu}_e\nu_\mu$, was used to determine the lifetime of the muon to be 2.2×10^{-6} seconds. The muon lifetime can be calculated as,

$$\tau_\mu = \frac{1}{\Gamma} = \left(\frac{G^2 m_\mu^5}{192\pi^3}\right)^{-1}, \tag{1.4}$$

where G is the Fermi coupling constant and m_μ is the mass of the muon.

Ignoring any strong interactions that may occur with a charmed particle decay, the decay, $c \rightarrow s$, can be scaled as a pure weak decay giving,

$$\tau_{\text{charm}} \approx \frac{1}{2+3}\left(\frac{m_\mu}{m_c}\right)^5 \approx 0.7 \times 10^{-12} \text{ seconds}. \tag{1.5}$$

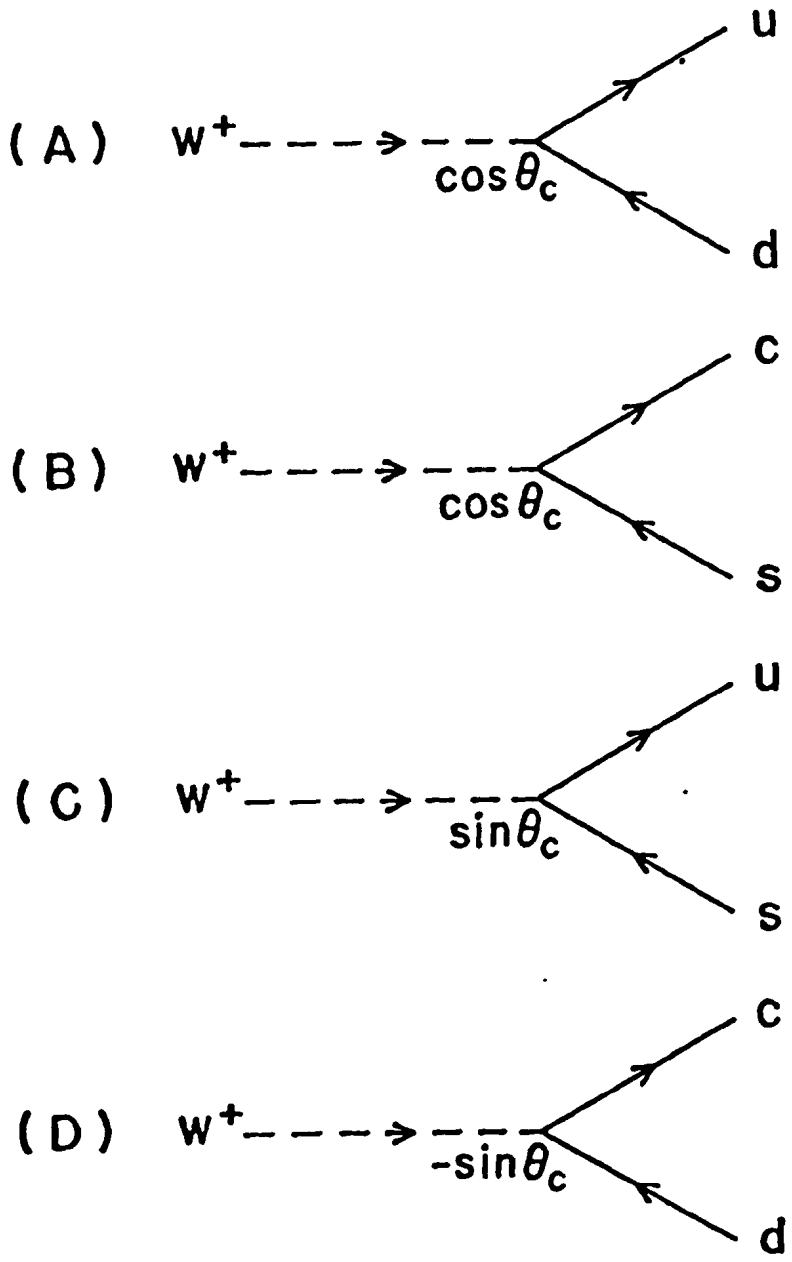

Figure 1.5: Weak Decay Mechanisms of Charmed Mesons: (A) and (B) are Cabibbo-favored; (C) and (D) are Cabibbo-suppressed.

Table 1.1: CURRENT WORLD LIFETIME AVERAGES

MESON	LIFETIME (ps)
D^+	1.062 ± 0.028
D_s^+	0.445 ± 0.032
D^0	0.421 ± 0.010

The factor, 2+3, refers to the two leptons and the three colors into which the W-boson can decay. The mass of the charmed quark used was 1.5 GeV, as suggested by $K^0 - \bar{K}^0$ mixing [5].

This spectator lifetime calculation would suggest that all charmed mesons should have the same lifetime value in the range of 10^{-13} ($\tau(D^0) \approx \tau(D_s^+) \approx \tau(D^+)$). This is shown in Fig. 1.6 where the matrix element for each of the three charmed meson decays is proportional to $\cos^2\theta$ (phase space factors ignored).

Current results do not support the assertion that all charmed mesons have the same lifetime. In fact, the lifetime values presently scale as, $\tau_{D^+} \gg \tau_{D_s^+} \geq \tau_{D^0}$. This is shown in Table 1.1 where the current world average lifetimes [6] of the charmed mesons are displayed.

Due to limited statistics, the D_s^+ lifetime is not very well established. The measured value of its lifetime has increased steadily over the years since its discovery in 1983. This is shown in Table 1.2 where the D_s^+ lifetime (world average) is listed from its discovery to the present.

Although the errors have improved, the measured lifetime value has approximately doubled. It now appears that the D_s^+ lifetime measurement is stabilizing at a value slightly longer than the D^0 lifetime although still consistent with being equal to that lifetime.

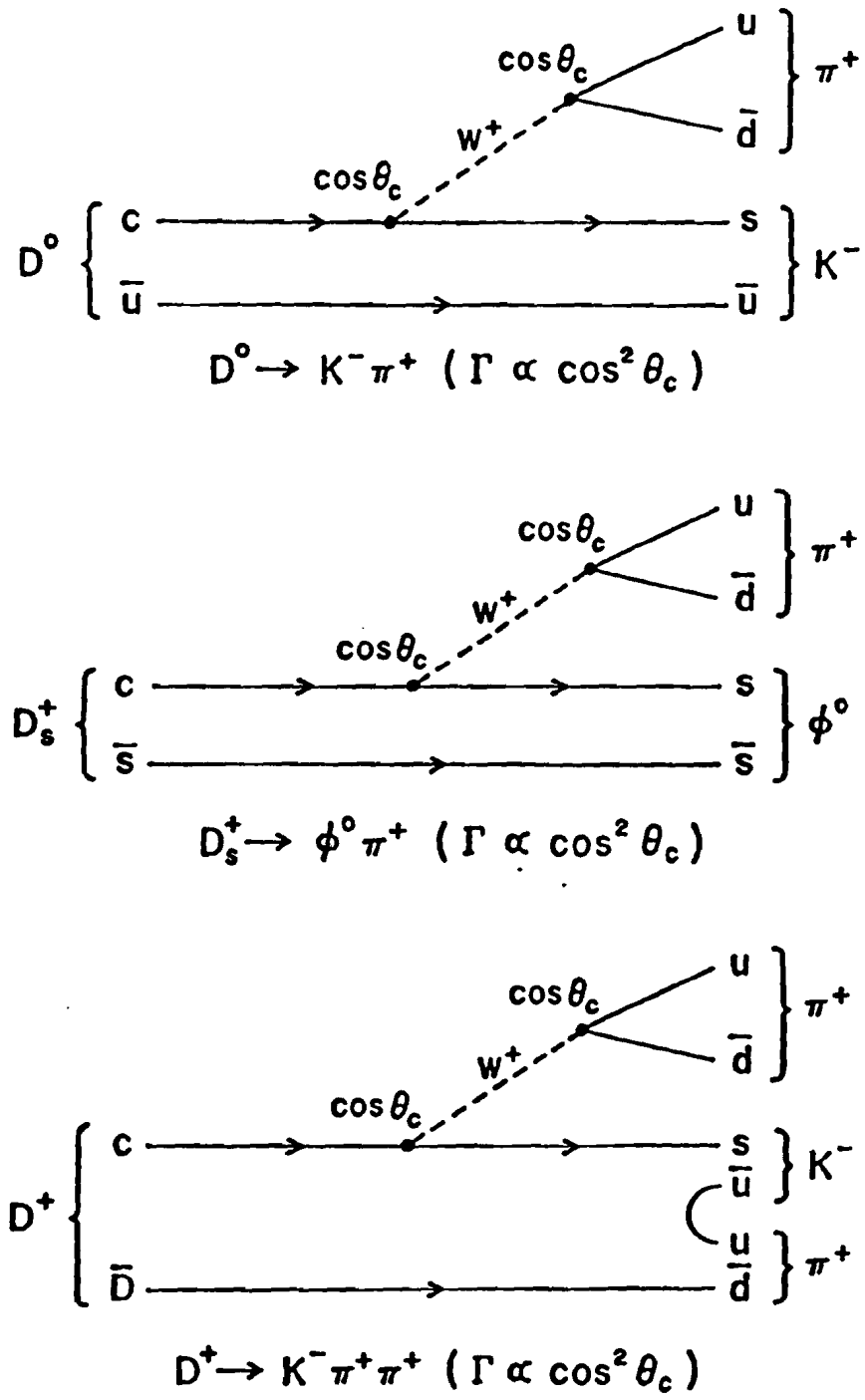

Figure 1.6: Spectator Diagrams (lowest order) for D^0, D_s^+ and D^+ Mesons.

Table 1.2: D_s^+ WORLD LIFETIME AVERAGES

YEAR	LIFETIME (D_s^+) (ps)
1984	$0.19^{+0.13}_{-0.07}$
1986	$0.28^{+0.16}_{-0.07}$
1988	$0.436^{+0.038}_{-0.032}$
1990	$0.445^{+0.035}_{-0.029}$

The value of the experimental result,

$$< \tau_{\text{charm}} > \approx \frac{1}{2}(\tau_{D^0} + \tau_{D^+}) \approx 0.7 \times 10^{-12} \text{ seconds,} \tag{1.6}$$

is indeed equal to the spectator model prediction. But the disparity between the D^0 and D^+ lifetimes cannot be ignored. The spectator model for charmed particle decays is clearly too naive in predicting lifetimes.

One major point to consider is that diagrams other than the spectator quark diagram contribute to the charmed meson decays. Diagrams to consider include spectator external W-emission, spectator internal W-emission, W-exchange and W-annihilation. The quark flow diagrams (lowest order) of each of these are shown in Fig. 1.7. Two other diagrams, penguin and sideways penguin, could also contribute to charm decays, but penguin diagrams are always Cabibbo-suppressed and are therefore ignored.

Both the D_s^+ and D^0 mesons can decay by both Cabibbo-favored spectator and Cabibbo-favored W-annihilation diagrams, while D^+ mesons can decay only by Cabibbo-favored spectator modes. This difference may explain the difference in D^+ and D^0 lifetimes and the near equality of D^0 and D_s^+ lifetimes.

The ratio of τ_{D^+}/τ_{D^0} is measured experimentally to be nearly 2.5. Considering that the D^0 meson can decay as both spectator (SPEC) and W-annihilation (WA)

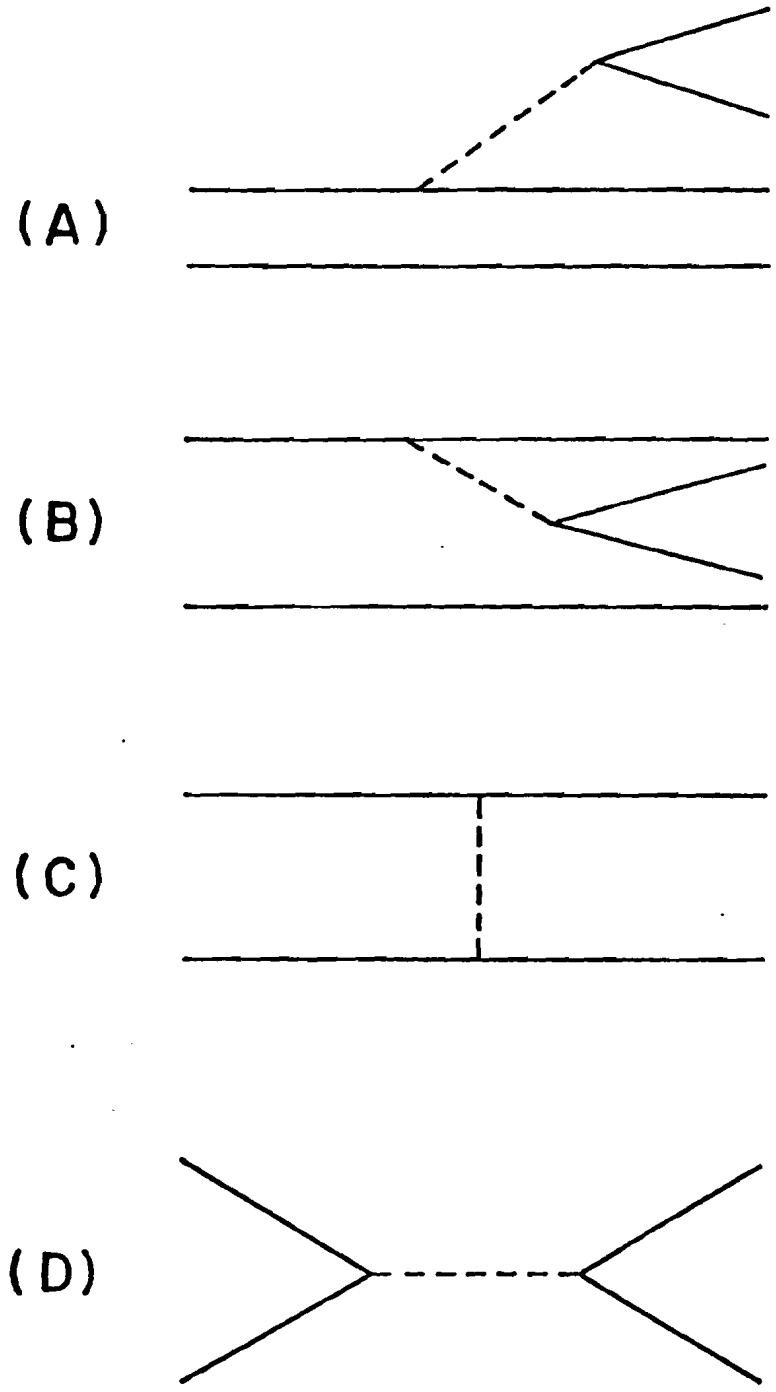

Figure 1.7: Lowest Order Diagrams for Charm Decays: (A) External W-emission (Spectator); (B) Internal W-emission (Spectator); (C) W-exchange; (D) W-annihilation.

(both are Cabibbo-favored) and that the D^+ meson can decay only as Cabibbo-favored spectator, one can argue that if only WA diagrams are to explain the disparity in lifetimes, then

$$\frac{\tau_{D^+}}{\tau_{D^0}} \approx \frac{\Gamma_{\rm SPEC}(D^0) + \Gamma_{\rm WA}(D^0)}{\Gamma_{\rm SPEC}(D^+)} \geq 2.5. \tag{1.7}$$

(All Cabibbo-suppressed modes are ignored since their contributions to the decay are small. Any interference between the decay widths has also been ignored.)

Since $\Gamma_{\rm SPEC}(D^0) \approx \Gamma_{\rm SPEC}(D^+)$, one can write,

$$\frac{\tau_{D^+}}{\tau_{D^0}} \approx 1 + \frac{\Gamma_{\rm WA}(D^0)}{\Gamma_{\rm SPEC}(D^+)} \geq 2.5. \tag{1.8}$$

This implies that $\Gamma_{\rm WA}(D^0)$ and $\Gamma_{\rm SPEC}(D^+)$ are nearly equal. This contradicts other arguments, such as the helicity suppression of WA decays, which predict that $\Gamma_{\rm WA}(D^0) \ll \Gamma_{\rm SPEC}(D^+)$ [7]. Modifications due to phase space factors and final state dynamics tend to favor W-annihilation decays somewhat. But the argument of W-annihilation being totally responsible for the lifetime differences does not appear to be correct [8]. One theoretical approach uses an expansion of $1/N_c$, where N_c is the number of colors, to argue for a small contribution by WA diagrams [9].

Another contribution to the D^+ and D^0 lifetime disparity is that color coherence contributes to the D^+ decays but not to the D_s^+ or D^0 decays [10][11]. By examining the Cabibbo-favored of the D^+ in Fig. 1.6, one sees that two $\bar{d}$-quarks are in the final state. The final decays states of the D^0 and D_s^+ do not contain two identical quarks. Since the $\bar{d}$-quarks are fermions, a negative interference will occur since these two quarks cannot occupy the same state. The width of the D^+ decays will therefore be smaller resulting in a longer lifetime.

Aside from the theoretical approaches listed above, other arguments exist to explain the differences in meson lifetimes. Many are variations of the same basic approach and can be found elsewhere [12][13].

Although current experimental results seem to support that

$$\tau_{D^+} > \tau_{D_s^+} \approx \tau_{D^0}, \tag{1.9}$$

the result,

$$\tau_{D^+} > \tau_{D_s^+} > \tau_{D^0}, \tag{1.10}$$

may also be probable. This can be explained by studying the semi-leptonic branching ratios of the charmed mesons. By isospin arguments (relating the up and down quarks) [8], one can write,

$$\Gamma(D^+ \to l\nu X) \approx \Gamma(D^0 \to l\nu X) + O(\sin^2\theta_c), \tag{1.11}$$

implying that,

$$\frac{\tau(D^+)}{\tau(D^0)} \approx \frac{\mathrm{BR_{SL}}(D^+)}{\mathrm{BR_{SL}}(D^0)} \tag{1.12}$$

(up to corrections of the order of θ_c^2).

Similarly, arguments of V-spin (relating the up and strange quarks) rather than isospin relate $\Gamma(D_s^+ \to l\nu X)$ and $\Gamma(D^0 \to l\nu X)$. Since W-annihilation is very likely to break V-spin and not I-spin, one can argue,

$$\frac{\mathrm{BR_{SL}}(D_s^+)}{\mathrm{BR_{SL}}(D^0)} > \frac{\tau(D_s^+)}{\tau(D^0)}. \tag{1.13}$$

The best way to test this hypothesis is to measure the semi-leptonic branching ratios of the D_s^+ and D^0.

In summary, both W-annihilation and d-quark interference contribute to the differences in the lifetimes of the D^+ and D^0 mesons with d-quark interference probably being the larger effect. Other models exist to explain this difference. Given the current statistics, it's not clear whether the D_s^+ lifetime is somewhat longer or equal to the D^0 lifetime. The lifetime measurement of the D_s^+ presented in this dissertation will assist in determining this ambiguity by increasing the world lifetime

measurement sample by nearly 25%. It will also reconfirm the D_s^+ lifetime measurement of another high statistics photoproduction experiment whose D_s^+ lifetime measurement nearly doubled the world average of this quantity [14].

1.3 Charmed Meson Lifetime Measurements in E687

This section addresses the advantages experiment E687 has over other charm production experiments in determining charmed particle lifetimes. The first advantage of E687 in measuring charmed lifetimes is the photon beam. Although the fraction of charmed particles in photoproduction is 1/40 that of e^+e^- collision, a photon beam allows for higher luminosities and cross sections [15]. (The fraction of charmed particles in photoproduction is 10 times greater than in hadroproduction.) Recent measurements of the lifetimes of charmed particles produced in photon interactions have played a major role in the determination of D^+ , D^0 and D_s^+ lifetimes [6]. The higher photon energies create a greater forward Lorentz boost for the charmed particles resulting in longer laboratory decay lengths. This consequence facilitates lifetime measurements.

A second advantage of experiment E687 is the performance of the spectrometer. In order to identify charmed particle states, one must first identify the final decays states. The E687 spectrometer has excellent particle identification for a broad range of particle momenta. (This is discussed in detail in the Chapter 3.) To measure the lifetime of a charmed meson, one must measure the separation distance between the primary and secondary decay vertices. (This is studied in Chapter 4.) The microstrip system allowed precise determination of this quantity. (This is discussed in Chapter 3 along with all the other components that contribute to extraction of charmed particle states from the plentiful background.)

CHAPTER 2

BEAM LINE AND SPECTROMETER

The data analyzed for this thesis were obtained in the 1987-1988 data run of experiment E687 at Fermi National Accelerator Laboratory (FNAL) in Batavia, Illinois, USA. One of the most distinguishing features of Fermilab experiment E687 was that it obtained nearly 60 million photon-beryllium and photon-silicon interactions with the highest photon beam energy in the world. The steps that produced a beam of photons with an average energy of 220 GeV from 800 GeV incident protons accelerated by the Fermilab Tevatron are described first in this chapter. (The photon energy spectrum is discussed later in the chapter.) It concludes with a discussion of the E687 spectrometer emphasizing those components contributing to the $\phi^0\pi^+$ analysis.

2.1 The Photon Beam

The photon beam was obtained by using 800 GeV protons to produce electrons and then having the electrons radiate photons by bremsstrahlung. The production of the 800 GeV protons is first described and then their transport to produce photons is presented.

2.1.1 The Accelerator

The protons that eventually are accelerated to 800 GeV begin as hydrogen gas in an ion source. An intense electric field within the ion source strips electrons from the hydrogen molecules leaving protons. The protons are then sent into a pre-accelerator to begin five steps in the process of full acceleration.

The pre-accelerator is actually a Cockcroft-Walton power supply of 750 kilovolts. The protons are accelerated in this electric field to an energy of 0.75 MeV after travelling about 30 centimeters through the accelerator [16].

After emerging from the pre-accelerator, the protons then travel to a linear accelerator (LINAC). Consisting of a series of accelerating cavities extending a distance of 175 meters, the LINAC accelerates the protons to 200 MeV. This is accomplished by the intense electric fields within each cavity which build and then provide a stream of protons extending for about 10 microseconds. From here the protons enter the Booster.

The third accelerator element in the chain, the Booster, consists of 96 ten foot long magnets arranged in a circle of radius 75 meters. Here the protons are accelerated from 0.2 GeV to 8 GeV. It takes nearly 16,000 trips through the magnet cavities to reach this final energy. On the average, the protons gain 0.5 MeV per turn and achieve 8 GeV in 33 microseconds. Now the protons enter the Main Ring (MR) and Tevatron Accelerators.

Both the Main Ring and Tevatron Accelerators are located six meters below the ground in a ring tunnel of one kilometer radius. The protons are first injected in the Main Ring Accelerator where they are accelerated to 150 GeV. The Main Ring Accelerator was once the original Fermilab accelerator capable of accelerating protons to 400 GeV. It was later modified to be used as an injector for the Tevatron.

The 150 GeV protons then enter the final accelerator, the Tevatron [17]. Made of superconducting magnets, the Tevatron accelerates the protons to 800 GeV. Although designed to accelerate protons to 1 TeV (1000 GeV), the Tevatron's ability to accelerate protons was more typically restricted to 800 GeV due to problems with magnet performance and reliability. The Tevatron produced an intensity of 2×10^{13} protons per pulse.

Once the proton beam is extracted from the Tevatron, it is directed to the switchyard. Here the proton beam is manipulated and shaped in preparation for being sent down to the three experimental beam lines of FNAL. These three areas are the meson, neutrino and proton lines. Experiment E687 was located at the terminus of the proton line in the Wide Band (WB) lab.

A schematic of the fixed target beamlines at Fermilab as well as the location of experiment E687 is shown in Fig. 2.1. This figure refers to the E687 experimental area as the Broad Band beam, but this area is officially called the Wide Band beam.

2.1.2 Beam Transport

After the protons have been accelerated to 800 GeV, they are used to begin production of the photon beam. Although clean photon beams are easiest to produce in electron accelerators where contamination of the beam by neutral hadrons is negligible, proton beams allow greater photon energies. Additional steps must also be taken to reduce the contamination of the photon beam by neutral hadrons [18]. An electron beam is first produced from the 800 GeV proton beam. Then photons are produced by the bremsstrahlung of the electron beam as detailed below.

The photons produced at experiment E687 have been produced through three steps involving two interactions and one decay process [19]. First the protons inter-

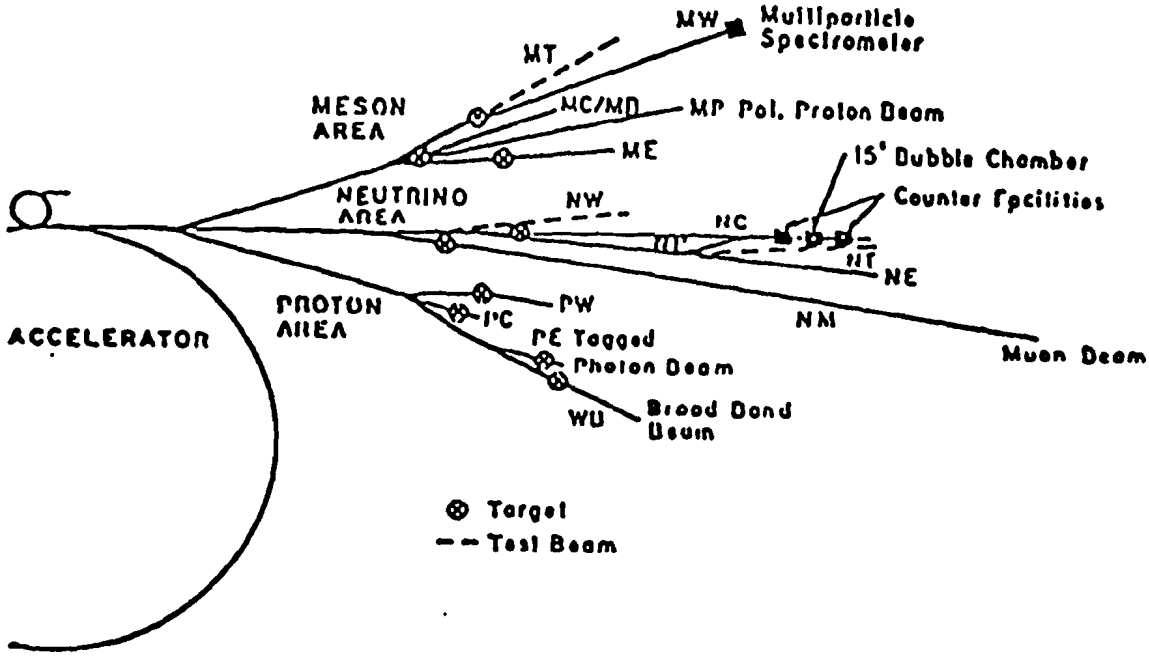

Figure 2.1: Beamlines at Fermilab.

act in the primary production target. Composed of an eighteen inch thick piece of beryllium, this target is struck by the proton beam to produce numerous particles. Immediately downstream of the primary production target are sweeping magnets that remove all charged particles leaving only neutral hadrons, K_L^0's, photons (almost all from $\pi^0 \rightarrow \gamma\gamma$ decays) and neutrons.

In the next step of the photoproduction process, the photons interact in a lead foil converter made of 50% of a radiation length of lead and produce electron-positron pairs. Being bent away from zero degrees, the electrons are then transported by dipole and quadrupole magnets. The remaining neutrals (neutrons, K_L^0's and unconverted photons) continue forward being absorbed in a particle dump.

Having been bent away from the original beam direction, the electrons then impinge on a thin lead foil radiator of 20% radiation length in which the electron beam produces photons by bremsstrahlung. The electrons are then swept away from the beam by dipole magnets and are eventually sent to a dump while the photons continue onward to the experimental hall.

In order to produce the most energetic and intense photon beam free of contaminants, a few parameters in the photoproduction process were varied. To attain a high flux of high energy photons, two requirements were made. First it was important to collect as many electrons emerging from the converter as possible. These emerging electrons had a wide range of angles and momenta. The optics of the beamline for E687 are arranged to collect electrons within a range of momentum of $\pm$ 15% around a particular momentum setting. This is the reason the E687 beam line is referred to as the Wide Band beam.

Second, the final flux is affected by the choice of thicknesses of the production target, the converter and the radiator. The values listed above were determined by Monte Carlo techniques for maximum photon energy and flux. For example

if the production target is too long, photons can convert as they travel from the production point to the end of the target. Also the converter cannot be too thick because the electrons will radiate energy via bremsstrahlung as they travel through the radiator. Finally increasing the converter thickness produces more electrons but lowers the average energy of those electrons. Too many electrons can similarly create too high a rate for the detectors of the experiment to accommodate adequately.

The Wide Band beam line was able to reduce the hadronic background of the photon beam by the following technique. The contamination by neutrals begins at the production target where, as previously mentioned, neutrons, K_L^0's and photons are produced. When the contaminating neutrals strike the converter, a small fraction of them interact and produce highly energetic charged hadrons (mostly charged pions and protons) which will be swept along by the electron beam transport. The charged hadrons produced by contamination are typically more positive than negative. For this reason, negatively charged particles are chosen to be sent down the secondary beam. The contaminating π^- will eventually interact hadronically with the radiator. These hadronic interactions are of concern only if they produce neutral particles that are transported along with the photons to the experimental target. But in order for this to occur, these particles must be produced within a milliradian of the incident charged hadron. The resultant background from neutral hadrons in the photon beam has been determined from Monte Carlo calculation and direct measurement giving a neutral contamination of nearly 10^{-5} neutrons per photon.

In Fig. 2.2 are recapitulated the steps that produce photons from an incident proton beam. The properties of the Wide Band beam are shown in Table 2.1.

The following are some performance results of the Wide Band Beam line. The yield of electrons observed was typically 10^{-5} per incident proton varying from

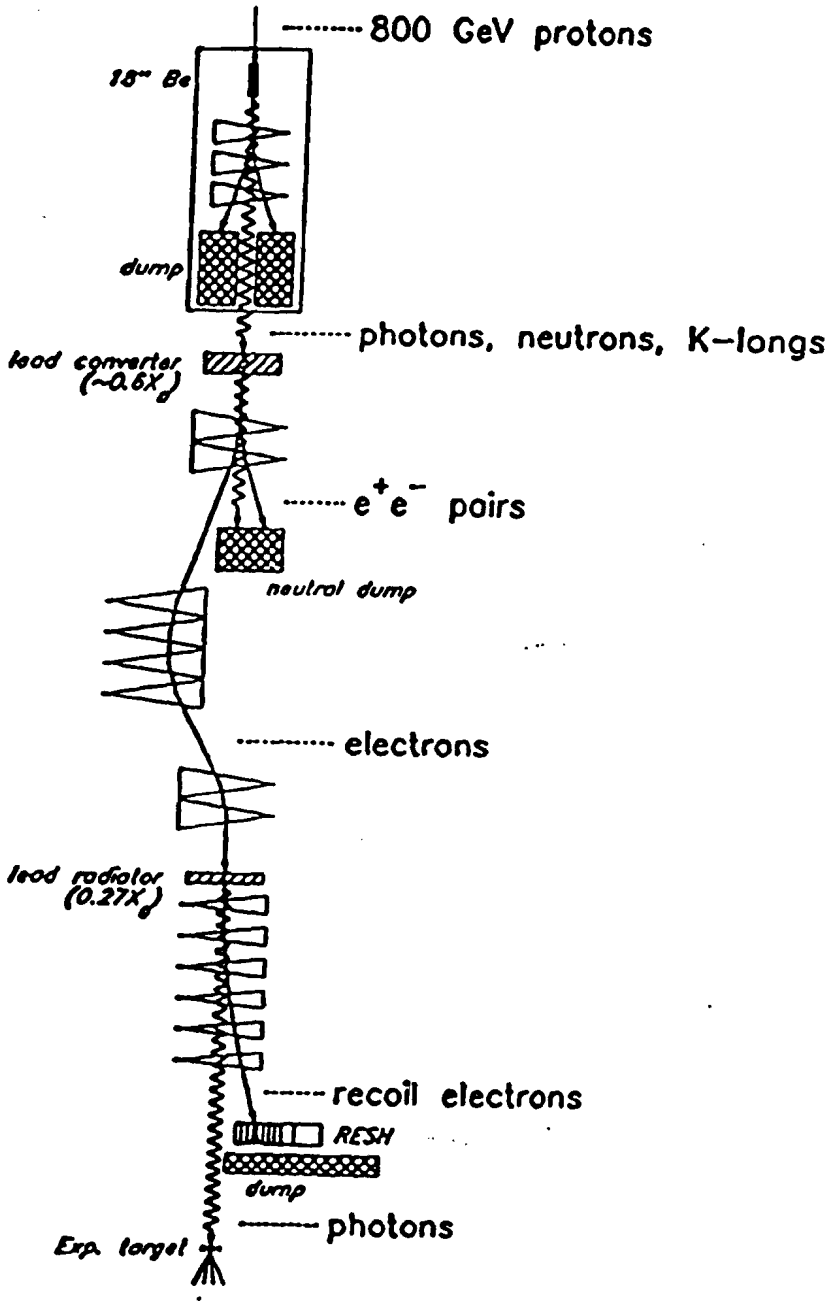

Figure 2.2: The Steps to Produce Photons from Protons (courtesy of Seongwan Park).

Table 2.1: WIDE BAND BEAM PROPERTIES

QUANTITY	VALUE
horizontal spot size at production target	$\delta x = \pm 1$mm
vertical spot size at production target	$\delta y = \pm 1$mm
geometric horizontal angle accepted	$\theta_x = \pm$ 1.0 milliradians
geometric vertical angle accepted	$\theta_y = \pm$ 1.0 milliradians
geometric solid angle accepted	$\Omega = \pm 3.0$ μsteradians
momentum bite accepted	$\frac{\Delta P}{P} \approx \pm$ 15%
total acceptance	$\delta\Omega \times \frac{\Delta P}{P} \approx 96$ μster·%
horizontal spot at experimental target	δ x = $\pm$1.25 cm
vertical spot at experimental target	δ y = $\pm$0.75 cm
horizontal divergence at experimental target	$\theta_x = \pm$ 0.6 milliradians
vertical divergence at experimental target	$\theta_y = \pm$ 0.5 milliradians

1.0×10^{-5} to 3.5×10^{-5}. The data analyzed in this thesis were obtained with an electron momentum setting (central value) of 350 GeV/c . The distribution of electron beam energy for the 350 GeV/c central beam setting is displayed in Fig. 2.3

The resulting photon energy distribution for the 350 GeV/c ($\pm$ 50 GeV/c) electrons is shown in Fig. 2.4. This spectrum of photon energy is not the photon spectrum of the recorded data. The energy of the photons in the beam is actually tagged by a Radiated Electron Shower Hodoscope (RESH) detector (discussed in the next chapter.) The tagged photon spectrum using RESH information is displayed in Fig. 2.5.

The data in this analysis were obtained with the photon energy spectrum of Fig. 2.5. The mean energy of photons interacting with the experimental target material was nearly 220 GeV. Other characteristics of the data set will be discussed in greater detail in the next chapter.

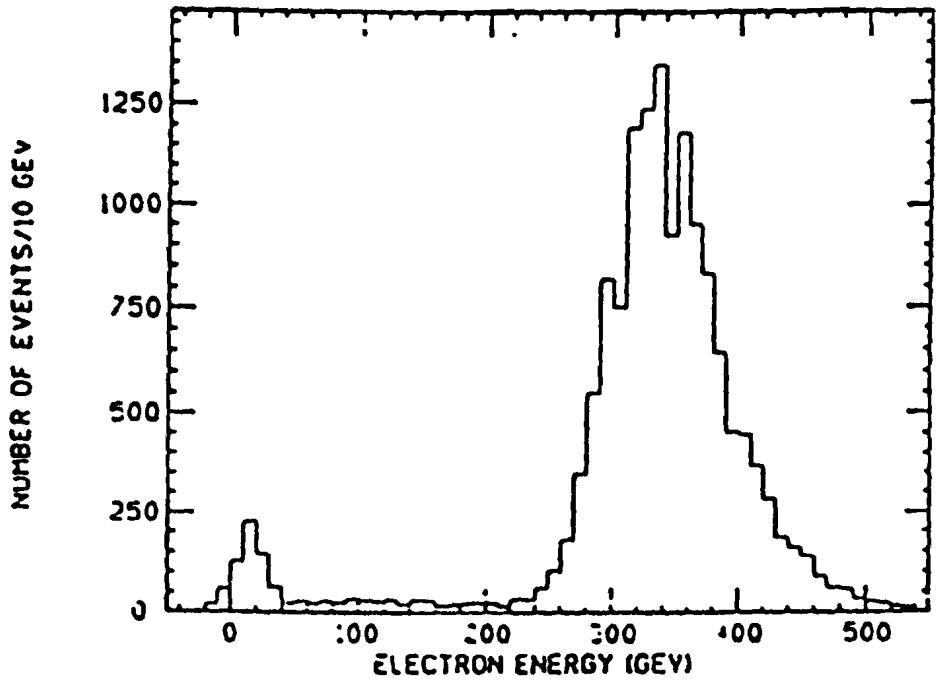

Figure 2.3: Electron Beam Energy Distribution for 350 GeV/c Central Beam Setting.

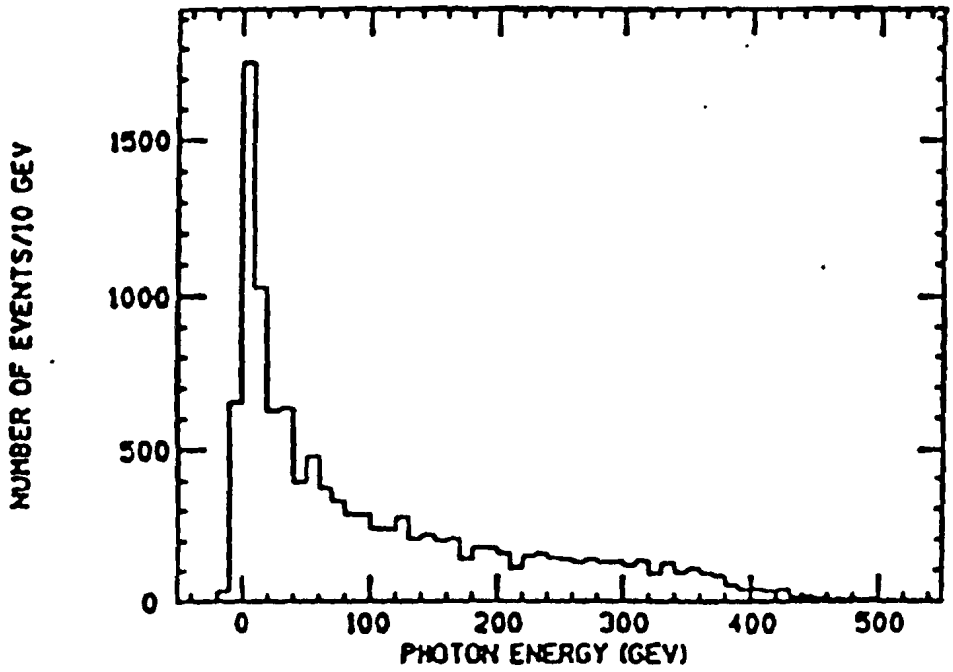

Figure 2.4: Photon Spectrum from 350 GeV/c Electrons.

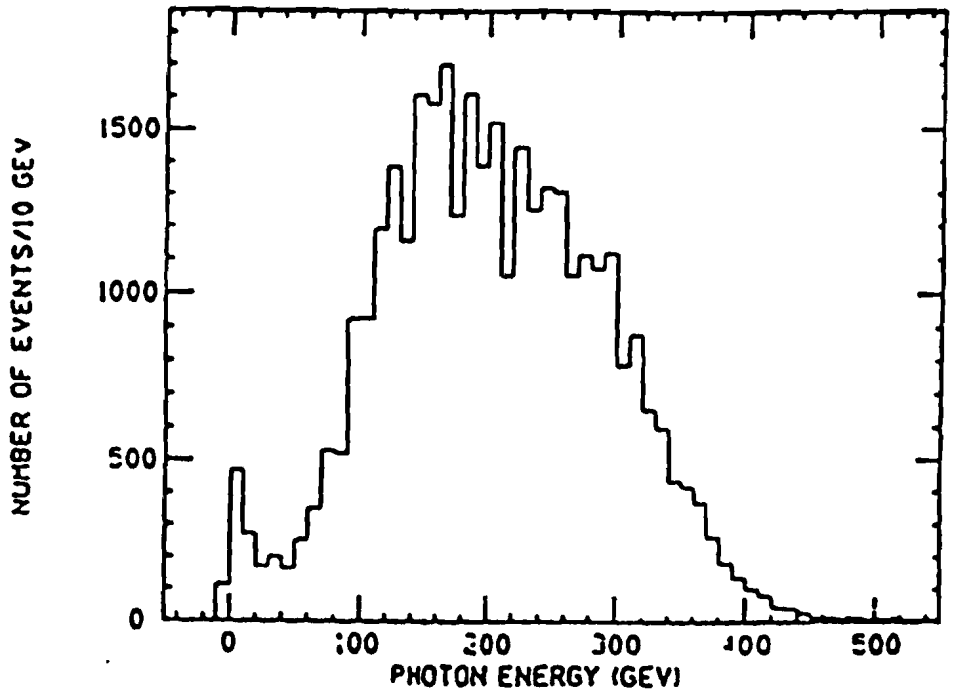

Figure 2.5: Tagged Photon Spectrum.

2.2 E687 Spectrometer

In this section, the detector systems used to extract the D_s^+ , $D^+ \rightarrow \phi^0\pi^+, \phi^0\pi^+\pi^-\pi^+$ events from all of the photon-Be and photon-Si interactions are studied. The E687 spectrometer from the target region and continuing downstream is shown in Fig. 2.6. There is also a magnified section of the target area shown Fig. 2.7. From Fig. 2.6 and Fig. 2.7, one can see that the E687 spectrometer comprises a silicon microstrip detector with four planes, five proportional wire chambers (PWC's), inner and outer electromagnetic calorimeters, two analyzing magnets, a hadron calorimeter, various trigger counters and a muon detection system.

This study of the E687 spectrometer begins with an examination of beam tagging and then turns to experimental targets, trigger counters, the microstrip detector system, the analyzing magnets and PWC's and finally the Čerenkov system. Several components of the E687 spectrometer such as calorimeters and the muon detection

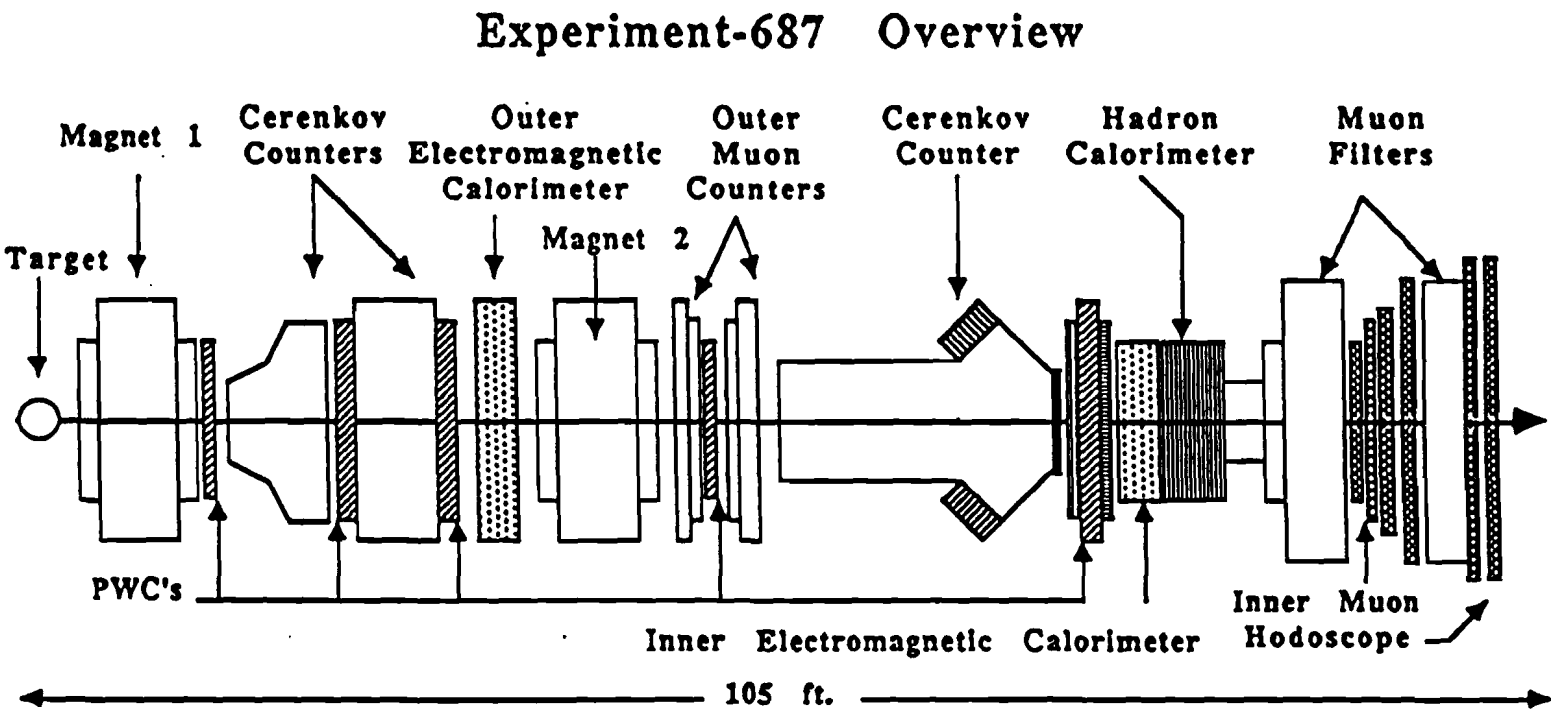

Figure 2.6: The E687 Spectrometer (view from above).

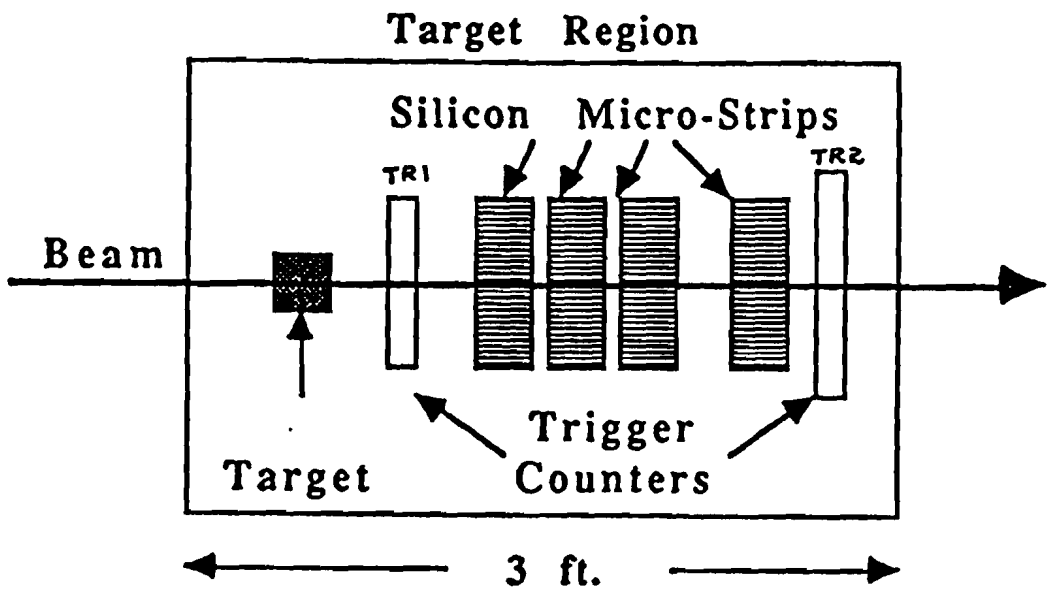

Figure 2.7: The E687 Target and Microstrip Region (view from above).

system are not discussed here but their characteristics can be found in other sources [20][21][22]. This section is written with an emphasis on the detectors used in the $\phi^0\pi^+$ analysis with particular attention paid to their construction and performance. Details of electronic read out and design considerations can be obtained elsewhere [20].

2.2.1 Beam Tagging System

As discussed in the previous section, the final step of the photon beam production occurs when the electrons pass through the lead radiator producing photons by bremsstrahlung. The photons continue to the experimental target while the electrons are swept away. The beam tagging system is designed to measure the energy of the interacting photon. It is also used in triggering to select electrons with minimal energy loss in the radiator (to "harden" the bremsstrahlung spectrum.) After

the electron loses energy by bremsstrahlung, its momentum is analyzed by a magnet spectrometer and the RESH (Radiated Electron Shower Hodoscope) detector. The RESH detector also measures the energy of the electron by calorimetric means. The combined RESH detector and magnetic spectrometer information can be used to measure E/p, thereby identifying the charged particle depositing energy in the RESH as an electron.

The RESH hodoscope counters were either lead-lucite or lead-acrylic scintillator shower counters each of about 24 radiation lengths in depth. There were 10 RESH counters consisting of 23 alternating absorber planes and detector planes. The absorber planes were made of quarter inch thick lead doped with 6% antimony.

One other component of the beam tagging was the Beam Gamma Monitor (BGM) counter positioned at the far downstream end of the E687 Spectrometer. This detector was used to measure the energies of the additional photons produced in the radiator but which did not interact in the experimental target. It also measures the energy of photons that interacted in the target and would later strike the BGM.

With the results of both detectors, the photon energy can be calculated on an event by event basis using the expression,

$$E_{e^-}^{\text{before}} = E_{e^-}^{\text{after}} + E_\gamma + E_\gamma^{\text{BGM}}, \tag{2.1}$$

where,

- $E_{e^-}^{\text{before}}$ is the energy of the electron before radiating;
- $E_{e^-}^{\text{after}}$ is the energy of the electron after radiating;
- E_γ is the energy of the radiated photon;
- E_γ^{BGM} is the sum of the additional energy deposited in the BGM detector.

Therefore the photon energy can be calculated as,

$$E_\gamma = E_{e^-}^{\text{before}} - E_{e^-}^{\text{after}} - E_\gamma^{\text{BGM}}. \tag{2.2}$$

The errors in the quantity E_γ result from errors or limited resolution of each of the remaining quantities. The quantity $E_{e^-}^{\text{before}}$ has large errors due to the large spread ($\pm$ 50 GeV/c for 350 GeV/c electrons) of the momentum of the incident electron. Similarly $E_{e^-}^{\text{after}}$ is imprecise due to the granularity of the RESH hodoscope. Typical photon energy distributions determined by this system are displayed in Fig. 4.18 of Chapter 4. The quantized appearance of the distribution is a direct result of the limited number of scintillator pieces in the RESH hodoscope.

2.2.2 Targets

Fermilab Experiment E687 used four experimental target configurations in the 1987-1988 data run. Two were made of beryllium and two were active targets, one made of silicon and the other of scintillating glass fibers. Two major considerations in the choice of target material are how the charmed particle cross section is affected by the material and whether the material suppresses the production of e^+e^- pairs typical of photoproduction. Since charm cross sections increase with the atomic weight, A, of the target material and the cross section for e^+e^- is proportional to Z^2, the quantity, Z^2/A, should be as small as possible. Beryllium is an easily utilized material with a low Z^2/A ratio.

Both beryllium targets were similar in construction. One was made of four pieces of beryllium (4BE); the other had five pieces (5BE). The 5BE target had 5 blocks of 4 millimeter thick beryllium separated by thin air gaps as shown in Fig 2.8. The diamond shape of the last three blocks was designed to match the high resolution region of the first station of the microstrip detector. The total length of the 5BE

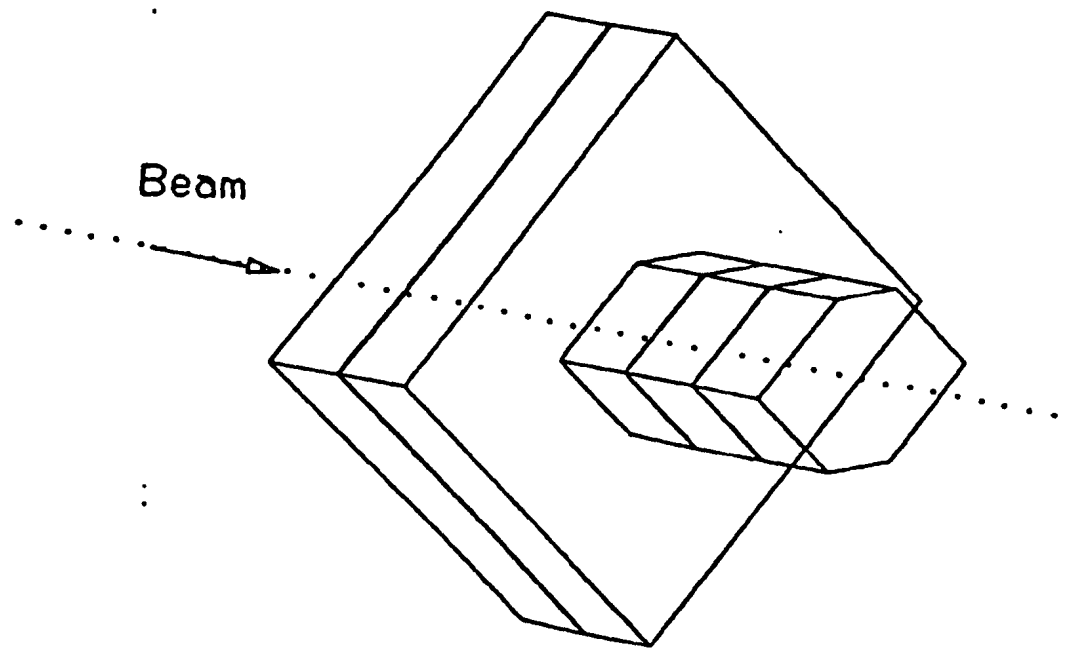

Figure 2.8: A Schematic of the 5 Stack Beryllium Target.

target was about 4.5 centimeters. Somewhat shorter in length than the 5BE target, the 4BE target had only one large piece of beryllium at the upstream end instead of two.

The first of two active targets, the silicon target (SILI), consisted of 48 pieces of silicon of thicknesses varying from 200 micron to 250 micron and had an active area of 2×2 cm^2. The second active target (SFT) was composed of a one inch cube of scintillating glass fibers. The characteristics and performance of this device are detailed elsewhere [23].

The data events analyzed to produce the D_s^+ , $D^+ \rightarrow \phi^0\pi^+, \phi^0\pi^+\pi^-\pi^+$ events were obtained with only the beryllium and silicon targets (roughly 90% beryllium and 10% silicon). The scintillating glass fiber target (SFT) was not included since those data runs were obtained using a pion beam instead of a photon beam. The

Z-coordinate vertex positions of primary vertices reconstructed in the data for each of the three targets (4BE, 5BE, SILI) showing their relative sizes and positions is plotted in Fig. 2.9 for comparison.

2.2.3 Trigger Counters

As will be discussed in the next chapter, various scintillation counters placed along the beam line played an important role in the trigger logic of the experiment. The first level trigger (also discussed in the next chapter) used the scintillation counters: A0, AM, TM, TR1, TR2, OH and H×V. The A0, AM and TM counters were placed upstream of the experimental target and were implemented to detect and reject any charged particles (typically muons) travelling within and near the photon beam.

The next two trigger counters, TR1 and TR2 (as seen in Fig. 2.7), were placed just upstream and downstream, respectively, of the microstrip detector . They were designed to detect charged particles coming from the target and were used in concidence. TR1 was 3.5 × 2.5 cm^2 and placed about three centimeters downstream of the target. This trigger counter becomes the downstream limit for the Z-coordinate position of the D_s^+ and D^+ decay vertices as discussed in Chapter 5. The transverse area of TR2 was 22 × 22 cm^2. The discriminator thresholds of TR1 and TR2 were set to trigger on single ionizing particles making them sensitive to e^+e^- pairs, dimuons, dihadrons and multihadronic final states.

The last two trigger counters, OH and H×V, served two purposes. They were used to reject the electromagnetic interactions of the photons and to identify final hadronic states. Consisting of one plane of 24 scintillator counters covering the upstream face of the outer electromagnetic counter, the trigger counter, OH, was designed to detect wide angle charged particles. Farther downstream of the OH

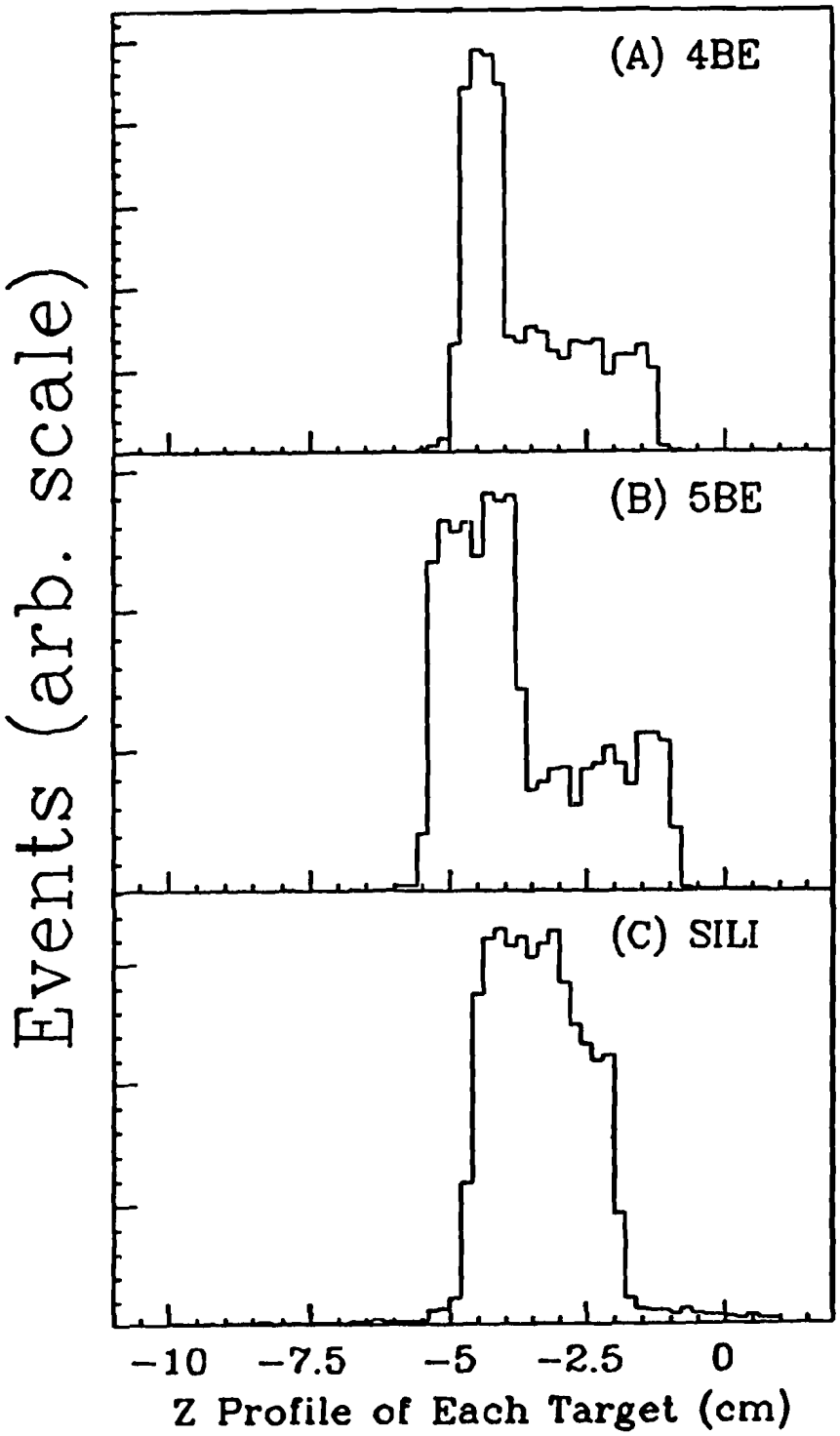

Figure 2.9: Z-coordinate Vertex Positions for each of the Three Target Configurations: (A) 4 Piece Beryllium (4BE); (B) 5 Piece Beryllium; (5BE)(C) Silicon Wafer(SILI).

Table 2.2: CHARACTERISTICS OF THE MICROSTIP DETECTOR

CHARACTERISTIC	STATION I	STATION II	STATION III	STATION IV
Active Area	2.5×3.5 cm^2	5×5 cm^2	5×5 cm^2	5×5 cm^2
High Res. Area	1.0×3.5 cm^2	2×5 cm^2	2×5 cm^2	2×5 cm^2
Strip Pitch	25μm, 50μm	50μm, 100μm	50μm, 100μm	50μm, 100μm
No. of Channels	688×3	688×3	688×3	688×3

counter was the H×V detector located just downstream of P4 (farthest downstream PWC). Consisting of two adjacent planes of scintillators with 24 and 12 counters placed horizontally (H) and vertically (V) respectively, the H×V detector along with the OH signals were used together with electronic logic to identify particles from a possible hadronic interaction. The use of these counters for triggering on possible charm events is discussed in detail in the next chapter.

2.2.4 The Microstrip Detector

Most important for the vertexing analysis, the silicon microstrip detector contained twelve planes grouped in four stations. The three detectors of each station were rotated at -135, -45 and -90 degrees with respect to the horizontal X-coordinate axis of the spectrometer. The most inner central region of the microstrip detector had a resolution two times more precise than the outer region. This is displayed in Table 2.2 along with other properties of the microstrip detector.

All of the detectors of the microstrip system were mounted on a high precision support allowing an alignment of ± 3 microns over 5 centimeters. The detection efficiency of every plane was greater than 99% including broken strips and broken electronics channels. The resolution of the system measured for infinite momentum

Table 2.3: MAGNET PROPERTIES

MAGNET	MAXIMUM P_T (GeV/c)	CURRENT (amps)
M1	0.400	1020
M2	0.850	2000

tracks crossing the high resolution regions of the twelve detectors was 9 microns.

2.2.5 Analyzing Magnets and PWC's

The E687 spectrometer contained two analyzing magnets, M1 and M2. These two large aperture dipole magnets deflected charged particles allowing for later momentum analysis. Both magnets bent the particles in the vertical (Y-coordinate) direction and in directions opposite to each other. The ratio of the momentum kicks was arranged so that charged tracks would return to their original undeflected positions by the time they had reached the inner electromagnetic calorimeter. The maximum transverse momentum kick and current setting for each magnet are listed in Table 2.3.

The spectrometer had five (P0, P1, P2, P3, P4) proportional wire chambers (PWC's) positioned throughout its length. These were essential for tracking charged particles. The chambers P0, P1 and P2 were located between the two magnets with P0 immediately downstream of M1. Chamber P3 was immediately downstream of the second magnet, M2, while P4 was downstream of the last Čerenkov counter, C3. Each PWC had four planes of wires (YVUX). The X view wires ran vertically measuring position horizontally; the U and V wires were ± 11.3 degrees from the Y view.

The five chambers could be divided into two groups, type A (P0 and P3) and

type B (P1, P2 and P4). The type A chambers each had an aperture of 30 × 50 inches. The anode wires were 0.8 mil in diameter and made of gold-plated tungsten under 65 grams of equivalent tension. The cathode wires were 2.5 mil in diameter and made of Cu-Be. They ran vertically with a pitch of approximately 0.4 times that of the anodes.

Similar in design to the type A PWC's, the type B chambers each had an aperture of 60 × 90 inches. The anode wires were also made of gold-plated tungsten but of 1.0 mil thickness and under 90 grams of equivalent tension. The cathode wires were also made of Cu-Be and were somewhat thicker than the type A's at 3.5 mil.

The gas mixture used in the PWC system was 65/35 argon-ethane bubbled through ethyl alcohol at zero degrees centigrade. With this gas mixture, the type A planes were operated at voltages between 3.3 and 3.5 kilovolts. Type B planes were operated at voltages between 3.0 and 3.3 kilovolts.

2.2.6 Čerenkov Counters

Three threshold Čerenkov counters were contained in the E687 spectrometer. Used for particle identification, Čerenkov counters are essential in identifying kaon and proton tracks. Since these tracks are common decay daughters of many charmed particles, their identification can assist charmed signal extraction by reducing the huge hadronic background typically composed of pions.

Each counter ran at atmospheric pressure and was filled with a particular gas or gas mixture. In Table 2.4 are listed the cell count, gas and particle thresholds for each Čerenkov detector. From this table, one can see that the pions are separable from protons or kaons at the C2 pion threshold of 4.4 GeV/c to the C3 pion threshold of 61 GeV/c while kaons can be separated from protons between 16 GeV/c and 116 GeV/c .

Table 2.4: ČERENKOV COUNTER PROPERTIES

COUNTER	NO. OF CELLS	GAS	TH(π)(GeV)	TH(K) (GeV)	TH(P) (GeV)
C1	90	HeN_2	6.7	23.3	44.3
C2	110	N_2O	4.4	16.2	30.9
C3	100	He	17.0	61.0	116.2

The first of the Čerenkov counters, C1, had a total length of gas volume of 71 inches when measured along the beam direction. The active transverse area of the counter measured 50 × 80 inches. Both planar and focusing mirrors were used for light reflection. Light collection cones were located in front of each of the two or three inch photomultiplier tubes that instrumented the counter. Typical photoelectron yields for each cell varied from 2.5 to 3.6.

The second Čerenkov counter, C2, was built by the University of Notre Dame. It was located downstream of C1 between the P1 and P2 chambers. The detector had an aperture of 90.5 × 100 inches and a length in the beam of 74 inches. An overview schematic of C2 is shown in Fig. 2.10.

C2 contained 110 cells with 54 inner cells and 56 larger outer cells. The 54 inner cells were instrumented with Thorn EMI 9939A 2 inch photomultiplier tubes while the outer cells used RCA 8854 PMT's (5 inch). The phototube faces of both the 2 inch and 5 inch PMT's were coated with p-terphenyl to improve light detection in the near ultraviolet. A transistorized base was attached to each 2 and 5 inch phototube. The electronics schematic for the 2 inch tube base design is shown in Fig. 2.11, while in Fig. 2.12 is displayed the schematic for the 5 inch bases. In both schematics, all resistors, except the 5.1K and 51Ω resistors, were power rated at one watt.

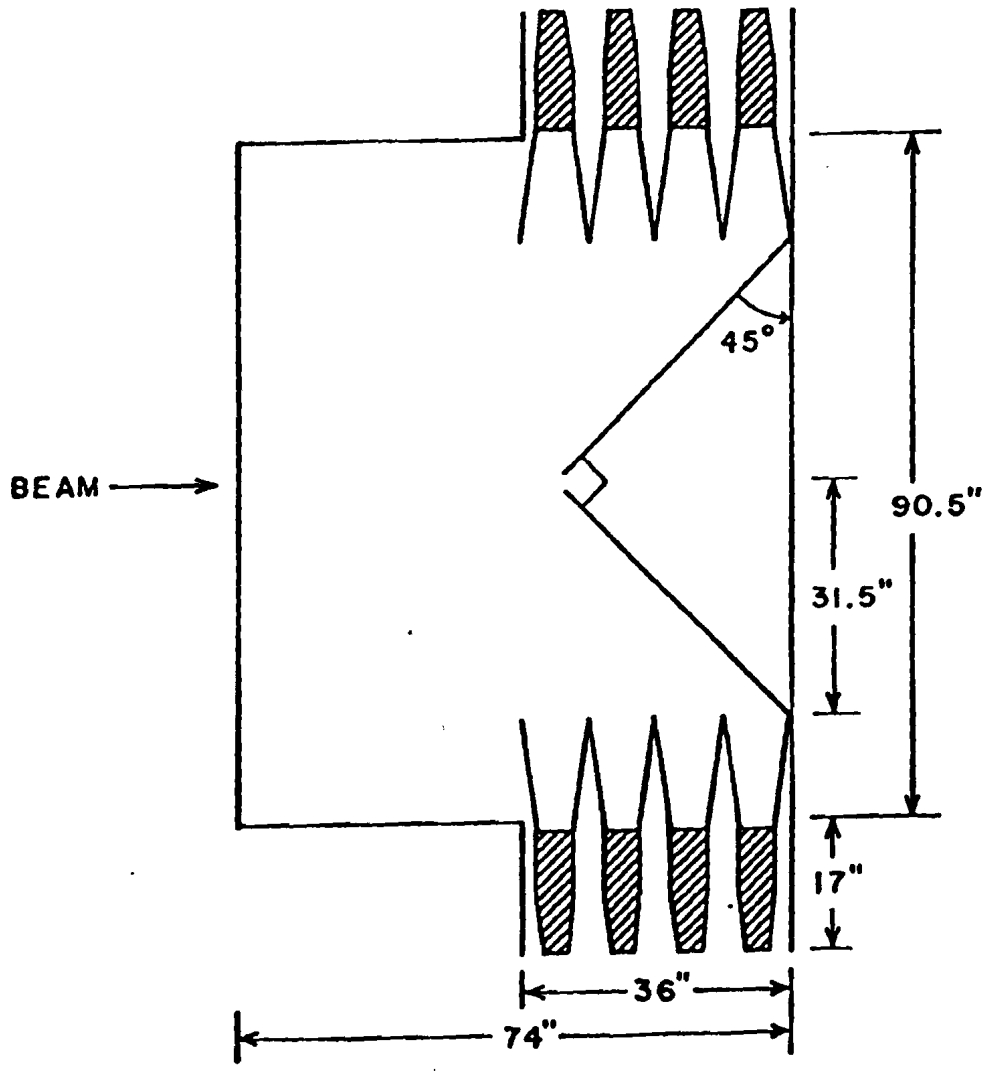

Figure 2.10: A Schematic of C2 (view from above).

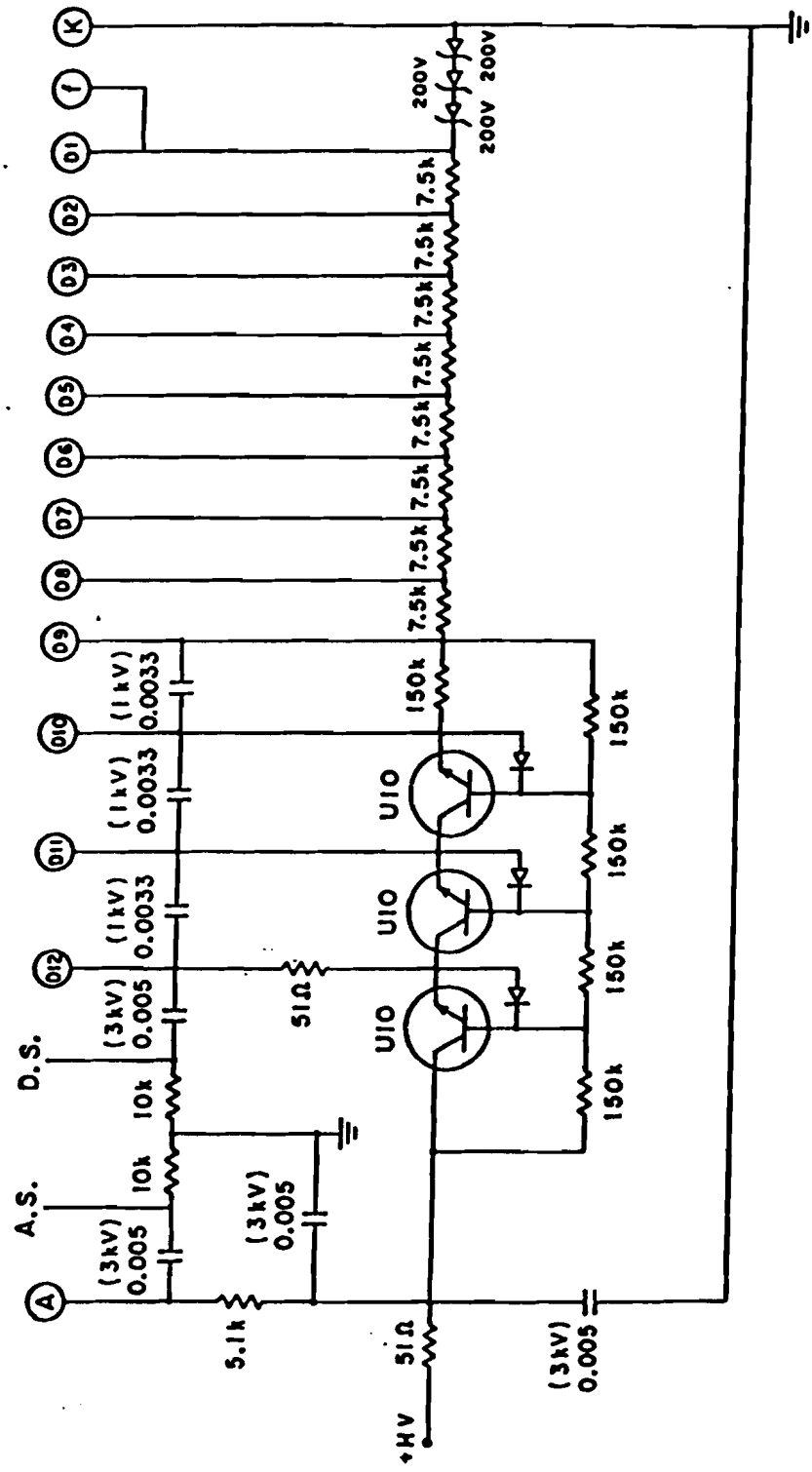

Figure 2.11: Schematic of 2 Inch Tube Base Design Used on Thorn EMI 9939A PMTs.

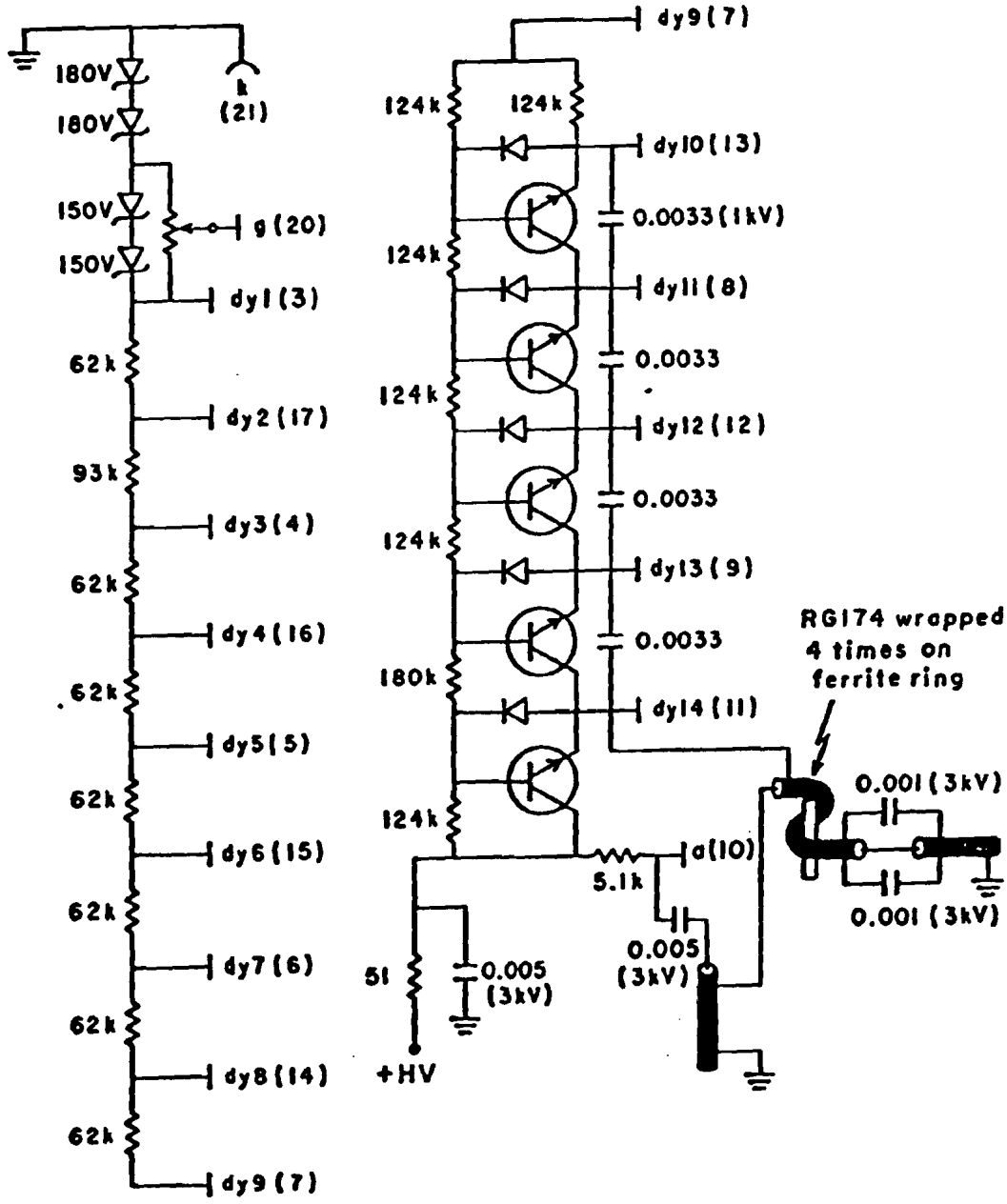

Figure 2.12: Schematic of 5 inch Tube Base Design Used on RCA 8854 PMTs.

As with the C1 counter, C2 had each phototube face equipped with a light collection cone. These cones were made of specular quality Coilzak which had been realuminized and overcoated with a 25 micron layer of magnesium fluoride (MgF_2). The realuminizing process consisted of electrolytically applying a barrier film of Al_2O_3 of approximately 30 nanometers thickness on the Coilzak. A photographic survey of the 110 cells to determine cell positions and boundaries was made. This survey was accomplished by opening the Čerenkov counter and photographing the image of the light collection cone array on the mirror. The photograph was then digitized to quantize the cell boundaries as seen in Fig. 2.13. The gaps between cells resulted in mismatches between adjoining light collecton cones.

The counter contained two planar mirror sections. The mirrors reflected the Čerenkov light toward the phototubes which were mounted on both sides of the counter. As shown in Fig. 2.10, the mirror sections were each mounted at a 45 degree angle relative to the beam direction forming a 90 degree angle between them. The mirror sections were each 63 × 92 inches and contained 32 separate mirrors of thickness 0.0394 inches. Coated with a 50 nanometer thick layer of MgF_2, the mirrors measured 11.0 × 11.5 inches and had a reflectivity of 88% at a wavelength of 400 nanometers. A small vertical gap between the two mirror sections in the center of the counter was designed to reduce the material in the region of high incident photon and electon flux (as seen in Fig. 2.13).

As listed in Table 2.4, the gas used was nitrous oxide at atmospheric pressure. This gas produced the necessary thresholds while being relatively safe to utilize (compared to the alternative of CH_4 which has a similar momentum threshold but greater safety risks). Since no data on the scintillating properties of N_2O was available during the design of the counter, beam tests were performed at Brookhaven National Laboratory with a test cell. No evidence of scintillation was observed and

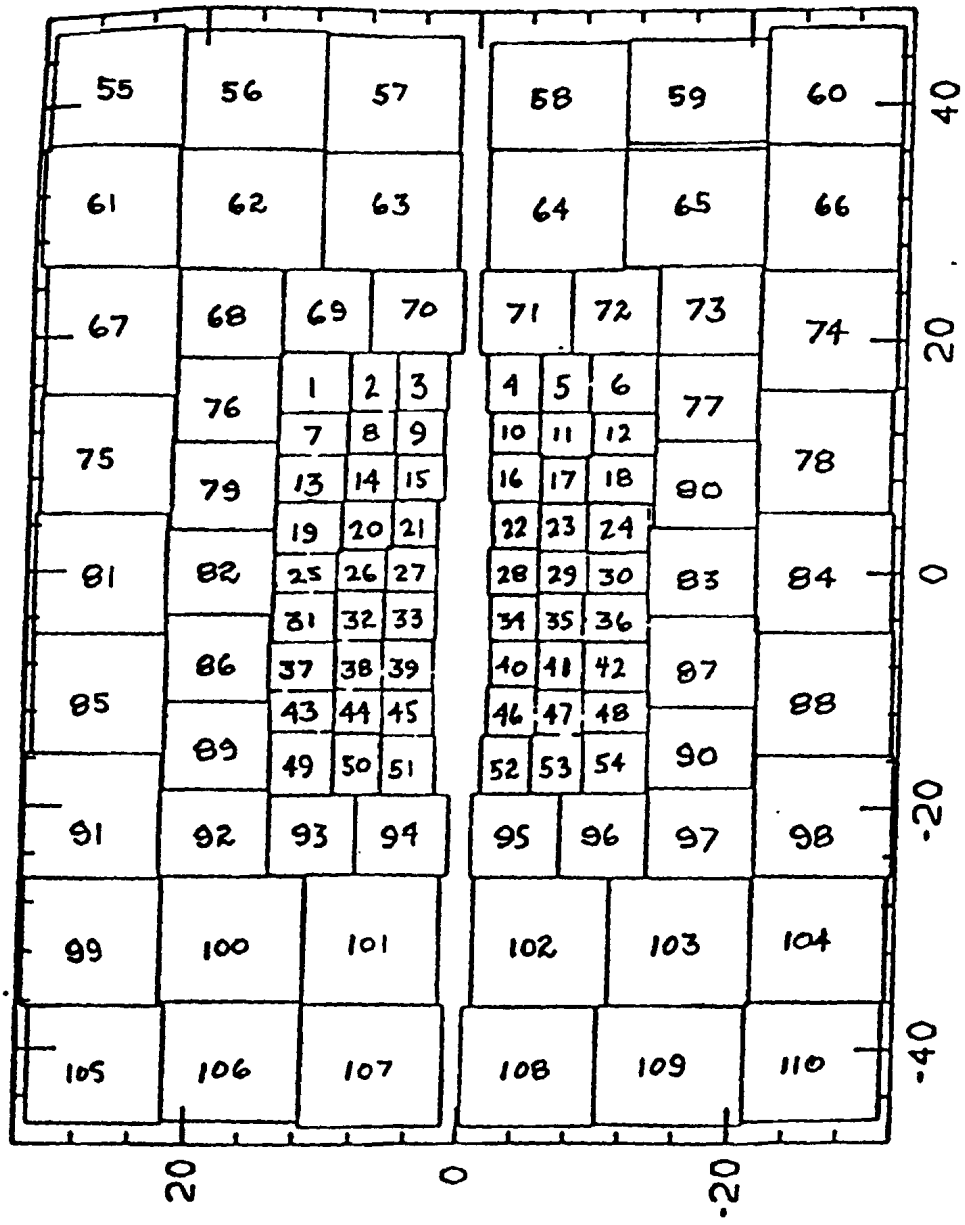

Figure 2.13: Photographic Survey Results Showing the Cell/Cone Structure of C2.

the nitrous oxide proved to work well in the experiment.

The photoelectron yields for C2 were substantially higher than those of C1. The yield for the 2 inch cells ranged from 8 to 16. For the 5 inch cells, the yield varied from 5 to 13 photoelectrons with an average of 8. These results are shown on a cell by cell basis in Table 2.5. The cell labels assigned are those defined in Fig. 2.13.

Downstream of C2 was the third Čerenkov counter, C3. This counter was the longest Čerenkov counter having a length of 277 inches and was segmented with 100 phototubes. Its aperture measured 60 × 93.25 inches. The counter had 100 spherical glass focusing mirrors with each mirror matched to a particular cell. Both 2 inch and 5 inch photomultipliers instrumented the counter. The photoelectron yields for all cells varied from 3 to 17 with an average of 9.

Table 2.5: PHOTOELECTRON YIELD FOR EACH CELL

Cell	Yld	Cell	Yld	Cell	Yld	Cell	Yld
1	14.8	29	11.9	57	8.0	85	5.6
2	13.4	30	10.4	58	7.5	86	10.9
3	7.9	31	10.9	59	7.5	87	13.0
4	9.3	32	14.0	60	9.8	88	8.1
5	10.1	33	12.1	61	7.8	89	6.9
6	8.1	34	12.3	62	8.0	90	7.6
7	9.7	35	12.8	63	8.3	91	8.2
8	12.0	36	14.0	64	7.7	92	8.8
9	8.7	37	16.4	65	5.2	93	10.1
10	11.5	38	9.9	66	8.8	94	10.2
11	7.5	39	12.0	67	5.8	95	13.0
12	9.3	40	13.6	68	8.1	96	10.6
13	9.2	41	10.9	69	8.5	97	5.5
14	15.7	42	12.1	70	8.8	98	8.5
15	11.2	43	12.7	71	7.8	99	9.4
16	14.9	44	10.8	72	11.3	100	6.2
17	10.6	45	11.7	73	6.5	101	6.6
18	14.3	46	10.3	74	8.7	102	8.6
19	15.4	47	13.6	75	6.1	103	5.9
20	9.8	48	12.6	76	9.6	104	7.2
21	11.3	49	14.0	77	8.6	105	7.2
22	10.1	50	14.1	78	8.2	106	10.0
23	13.4	51	10.2	79	8.2	107	9.8
24	14.7	52	9.8	80	8.9	108	5.3
25	10.6	53	11.3	81	8.4	109	11.7
26	14.5	54	8.7	82	10.6	110	7.1
27	8.6	55	8.8	83	8.1		
28	10.4	56	6.5	84	7.0		

CHAPTER 3

THE DATA SET

The technique of manipulating electronics signals from the E687 spectrometer to reconstruct charged particle tracks and then determine their momenta and probable particle identification is described in this chapter. The data run conditions are first examined. Next, the method of recording spectrometer electronic signals onto computer tape is briefly explored. The chapter is concluded with a study of PASS1, the experiment E687 data reconstruction program, with an emphasis on the data reconstruction components of PASS1 influencing the $\phi^0\pi^+$, $\phi^0\pi^+\pi^-\pi^+$ analyses.

3.1 Data Run

The operation of the spectrometer and the characteristics of the beam when the data were obtained are examined in this section. The triggers used to select charmed particle events are also studied.

3.1.1 Spectrometer and Beam Conditions

Fermilab experiment E687 began taking data in August 1987. This continued until October 1987. On the night of October 3, 1987, a fire occurred in the Wide Band pit (spectrometer) area. It was later determined that a short circuit in a power supply near the electromagnetic calorimeter (IE) had caused the IE plastic scintillator to

burn. This fire rapidly spread to other detectors in the spectrometer. The fire was subsequently stopped but only after completely destroying the IE and P4 detectors and severely damaging several others.

After a two month shutdown for repairs and cleaning, experiment E687 was commissioned for the second time to take data in December 1987. The inner electromagnetic calorimeter was not replaced. The P4 chamber was replaced with a smaller chamber having an aperture of 40 × 60 inches and only three views X, V and U (same angles). The X-plane had 3 millimeter spacings while the U- and V-planes had 2 millimeter spacings. All other damaged detectors were repaired and calibrated once again.

Because of the P4 chamber replacement and changes in the geometry of all detectors after the fire, only the data obtained after the fire were eventually reconstructed and analyzed. This data run, often referred to as the "post-fire" data run, began in December 1987 and continued until February 15, 1988. The data were obtained with an electron momentum setting of 350 GeV/c . The photon beam had an average energy of 220 GeV and had the energy distributon seen in Fig. 2.5. The data set consisted of some 60 million triggers at the end of the run. These 60 million raw events were recorded on 1200 nine-track tapes.

3.1.2 Triggering

Appropriate triggers required of the data events were essential to extract charm candidates and to reject background events. These triggers were divided into two levels in E687, the first level trigger or master gate and the second level trigger.

The master gate used the information from the trigger counters discussed in Chapter 2 (A0, AM, TR1, TR2, OH and H×V). As a reminder, the counters A0, AM and TM were scintillator counters placed directly upstream of the target and

were used for the rejection of charged particles within the beam. Counters TR1 and TR2 were scintillator counters placed both directly upstream and downstream, respectively, of the microstrip detector. These were used to detect charged particle tracks within the microstrip detector. The OH and H×V detectors were used to identify final hadronic states downstream of the target and microstrip regions and outside of the beam region.

The master gate was "on" when no charged tracks were detected upstream of the target (A0, AM and TM were "off"); when charged tracks were present within the microstrips (TR1 and TR2 were "on"); and when two body charged particles were present in the H×V and/or OH detectors. The master gate logic was then assigned symbolically as,

$$\mathrm{MG} = \mathrm{TR1} \cdot \mathrm{TR2} \cdot ((\mathrm{H} \times \mathrm{V})_{2\mathrm{body}} + \mathrm{OH} \cdot (\mathrm{H} \times \mathrm{V})_{1\mathrm{body}}) \cdot \overline{(\mathrm{A0} + \mathrm{AM} + \mathrm{TM})}. \quad (3.1)$$

This was the master gate for most of the run although a few other master gate combinations were occasionally used.

The second level trigger supplemented the master gate triggering by incorporating additional information from other detectors in the spectrometer such as RESH and calorimetry information. Numerous second level triggers were used in the post-fire data run but were organized according to the following scheme.

Each component of the second level trigger was assigned a hardware bus line. These bus lines were inputs to PIN logic modules and would be "on" if that component of the second level trigger was satisfied. The combined logic of the various bus lines coming from the PIN logic modules was used to form the second level trigger. The buslines and their descriptions are shown in Table 3.1.

The hadron energy triggers required that at least 40 GeV be deposited in the hadron calorimeter and the central hadron calorimeter. Beam tagging was accom-

Table 3.1: BUSLINE ASSIGNMENTS

BUSLINE	DEFINITION
1	muon anti-coincidence
2	particle present in the A0 counter
3	RESH energy > 116 GeV
4	RESH energy > 193 GeV
5	RESH energy > 212 GeV
6	RESH veto
7	silicon wafer trigger
8	2 muons in the inner muon system
9	2 muons in the outer muon system
10	1 inner and 1 outer muon
11	hadron energy > ELOW
12	hadron energy > EMED
13	hadron energy > EHIGH
14	E_{perp} > EPLOW
15	E_{perp} > EPHI
16	one charged track
17	two charged track
18-20	cuts on event multiplicity
> 20	reserved for calibration runs

plished with a RESH energy requirement. Most of the data was taken with the electron energy loss greater than 116 GeV (busline 3 required "on"), as determined by RESH information. The specific definitions of buslines 11 through 15 are related to calorimetry and can be found elsewhere [20].

Numerous trigger mixes of the second level trigger buslines were used throughout the data run. At times no second level trigger was implemented leaving only the master gate. This was labelled the minimum bias trigger.

3.2 Data Acquistion

When a master gate trigger was present, the data acquisition was alerted to begin the process of recording the event to tape. Then the electronics associated with the second level trigger were examined. If the second level trigger requirements were satisfied, all further master gates were inhibited for one microsecond. The data were now ready to be written to tape.

The process of writing an event to nine-track tape began by having all the electronics signals, including such quantities as ADC and TDC data, stored in one of five Fastbus memory modules. These memories were read into a PDP11/45 by means of a UPI interface module. The PDP then wrote the event to tape through a STC1921 controller connected to two tape drives. Two drives were used, so while one tape drive was being used the other could be rewound. A VAX11/780 was used both to supply events to the online monitoring and display programs and to pass information from the user to the PDP. A schematic of the E687 triggering and readout is shown in Fig. 3.1. More details on this topic can be found elsewhere [20][22].

The rate for recording events was roughly 3,000 two-kilobyte events in a one minute spill cycle. The above steps in recording the data were indeed the limiting

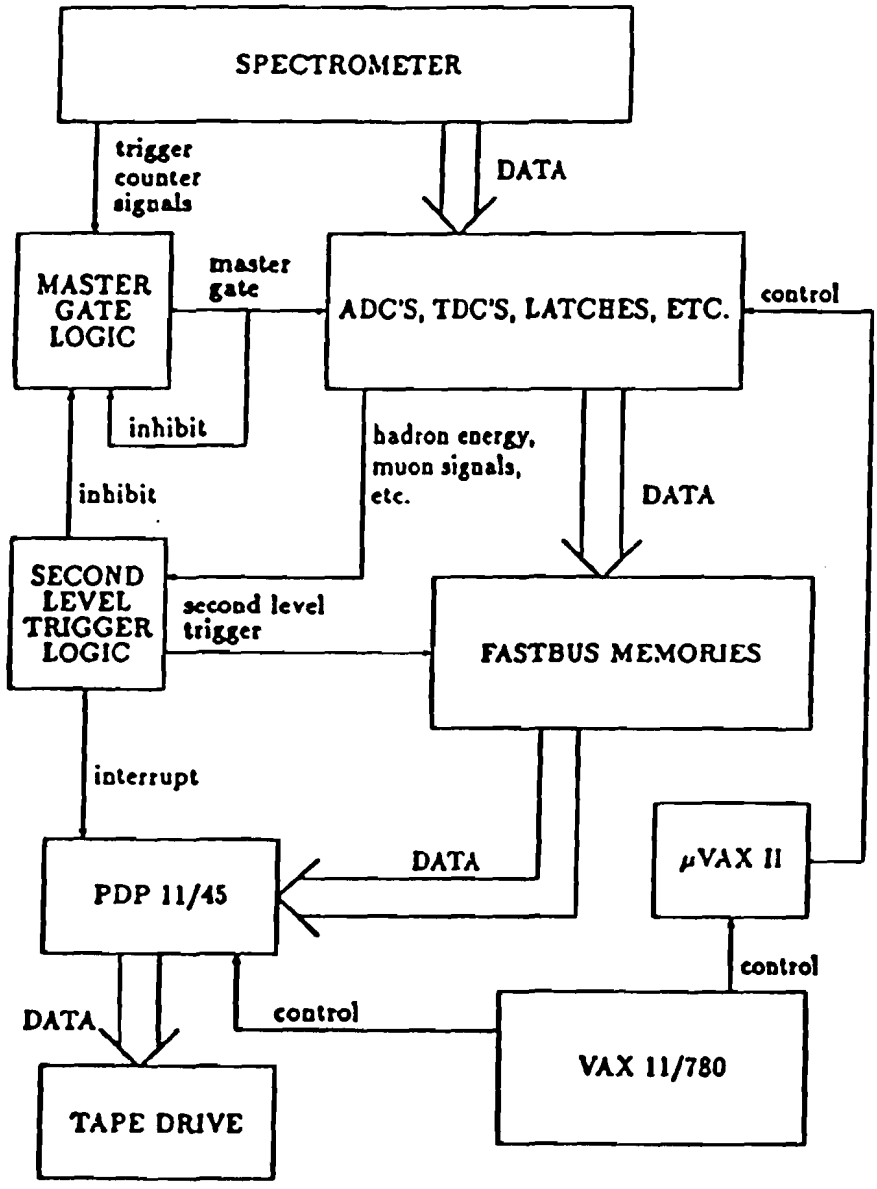

Figure 3.1: Trigger and Readout Schematic (Courtesy of Rikutaro Yoshida).

factor. But this rate was fairly close to the logging capacity of a nine-track tape and the maximum capacity of the UPI link. The total deadtime during the spill was about 30%. And as mentioned previously, the post-fire run ended with 60 million events being recorded on 1200 nine-track tapes.

3.3 Data Reconstruction

The raw data of experiment E687 consisted, among other quantities, of ADC integrated pulse heights from the Čerenkov counters, strip hits of the microstrip detector and PWC wire hits. The data reconstruction took this basic electronic information and used it to trace charged particle tracks, find vertices from these tracks and determine probable particle identification from the Čerenkov counters. In this way, physics analysis could begin by reconstructing the decays of charmed particles produced in the E687 spectrometer.

3.3.1 PASS1

The E687 reconstruction program, called PASS1, was basically divided into a series of reconstruction routines assigned to major detector systems such as the microstrip track reconstruction or Čerenkov reconstruction. Some components of the routine would also manipulate the newly reconstructed data. For example, the linking algorithm would attempt to match tracks found in the PWC system to those in the microstrip detector. PASS1 was performed on each raw data tape by the Fermilab ACP (Advanced Computer Project) system. The amount of information produced by PASS1 was nearly double that of the raw tape. Therefore, PASS1 produced nearly 2400 reconstructed data tapes.

Those elements of the PASS1 reconstruction program important to the D_s^+, $D^+ \to \phi^0\pi^+$ analysis will be discussed. The algorithms and performance of these

reconstruction programs are examined for the microstrip system, the PWC system, the magnet system, the linking algorithm and the Čerenkov algorithm. Since neutral vee (K_s^0's and Λ's) reconstruction is not used in this analysis, it is not discussed but can found elsewhere [20][21].

3.3.2 Microstrip Tracking

The basic idea in microstrip tracking is to determine the charged particle tracks from specific strip hits in the detector. This begins by examining the charge deposited in the detector and understanding clusters of hits. The idea was to separate the clusters that result from multiple tracks as opposed to those clusters left by one track alone. Projection finding of the three views is then begun by requiring at least three hits per view. If strip hits were used in a 4-station projection, they could not also be used in 3-station projections. The projections were subject to a least squares fit and cuts on their χ^2 were made ($\chi^2 < 8$ required). Tracks sharing one or two projections were arbitrated by means of their χ^2 values.

The unused hits were then used to search for wide angle tracks and tracks scattered by multiple coulomb scattering (MCS). These tracks were obtained by requiring at least six hits matching in space.

The efficiency of the microstrip tracking algorithm was measured on a Monte Carlo data set. These data, containing photoproduced $D\overline{D}$ events, showed an overall efficiency of 96%, including MCS effects. Nearly 2.7% of the tracks were spurious tracks. The reconstruction efficiency was a function of the momentum of the track having a value of 90% at 2.5 GeV/c and approached a value greater than 99% at 10 GeV/c .

As mentioned previously, the microstrip detectors are important for vertexing. One important quantity related to this is resolution. This was measured in the

microstrip system giving the following momentum dependent results:

$$\sigma_x = 11\mu\text{m}\sqrt{1 + \left(\frac{17.5\ \text{GeV}}{P}\right)^2} \tag{3.2}$$

and

$$\sigma_y = 7.7\mu\text{m}\sqrt{1 + \left(\frac{25\ \text{GeV}}{P}\right)^2}. \tag{3.3}$$

These expressions for the resolution were measured on tracks by extrapolating them to the center (high resolution) region of the microstrips and determining their error in the X-Y plane. These formulae include multiple coulomb scattering contributions due to both the target and the TR1 trigger counter.

3.3.3 PWC Tracking

Similar in design to the microstrip tracking algorithm, the PWC tracking algorithm searched for charged tracks among the wire hits of the PWC system. Two types of tracks were extracted depending on the number of chambers included in the fit. There were 5-chamber tracks and also 3-chamber tracks (often referred to as "stubs") where both sets of tracks were required to be contained in the P0 chamber. The 3-chamber tracks were presumably lower momentum tracks kicked out of the spectrometer at magnet M2 which would not leave hits in the remaining two wire chambers.

The PWC tracking began by determining projections in the U-, V- and Y-(bend) views of the PWC wire hits. In the X-view, hits were first examined from the extensions of microstrip tracks into the PWC system. A least squares fit was performed on all the track candidates. A χ^2 per degree of freedom cut was required of each track ($\chi^2/\text{DOF} < 0.45$).

In addition to the 3- and 5-chamber track topologies found in the PWC system, the PWC tracking algorithm searched for two other track topologies. One of these

routines extended microstrip tracks to the first two wire chambers (P0 and P1) and searched for unused hits. Another considered 3-chamber extensions in P3 and P4.

The efficiency of the PWC algorithm was measured on Monte Carlo generated tracks. These studies produced an efficiency of 98% for tracks with a momentum greater than 5 GeV/c . Spurious tracks were less than 0.5% of the total reconstructed tracks.

3.3.4 Momentum Analysis

By knowing the trajectory of a particle and the nearby magnetic field, the particle's momentum could be determined. This is exactly how the momentum was calculated in PASS1. Using precise knowledge of the magnetic fields of M1 and M2, as well as the bend parameters of the tracks, the momentum was calculated. The errors in the momentum were determined analytically as:

$$\frac{\sigma_P}{P} = 3.4\% \left(\frac{P}{100\ \mathrm{GeV}}\right) \sqrt{1 + \left(\frac{17\ \mathrm{GeV}}{P}\right)^2}, \tag{3.4}$$

for M1 and,

$$\frac{\sigma_P}{P} = 1.4\% \left(\frac{P}{100\ \mathrm{GeV}}\right) \sqrt{1 + \left(\frac{23\ \mathrm{GeV}}{P}\right)^2}, \tag{3.5}$$

for M2. These terms contain multiple scattering terms that dominate at lower momentum values.

3.3.5 Linking Algorithm

The linking of the microstrip tracks and PWC tracks was essential for the $\phi^0\pi^+$ analysis. Since precise vertexing information occurs in the microstrip detector and Čerenkov information was determined with PWC tracks, a routine to match PWC and microstrip detector tracks was required. This was done by extending both

PWC and microstrip tracks to the center of M1. A global least squares fit was performed on both tracks using all hits to determine matches. The efficiency of linking microstrips and PWC tracks was 92% for 3-chamber PWC tracks and 97% for 5-chamber tracks. This efficiency was somewhat lower at lower track momentum values where the microstrip tracks may have suffered from substantial multiple scattering and were not found by the microstrip algorithm.

3.3.6 Čerenkov Algorithm

Analysis of the Čerenkov counter signals is necessary to determine the particle identification. The information on the raw data tape is simply the integrated pulse heights from the ADC's (with pedestals suppressed). This information is recorded for each cell.

The Čerenkov algorithm begins by examining the ADC counts for each cell of the counters. Cells with corresponding ADC counts greater than 10 counts above the pedestal values are considered "on." Using tracking information, the cells associated with a particular track are examined. Assuming the track to be a pion, its predicted photoelectron yield for the cell is determined. If the predicted photoelectron yield was greater than some assigned requirement, the cell was labelled "on." If the expected photoelectron counter also greater than another required value but no ADC counts were observed for that cell, the track was flagged as "off." If neither of these conditions could be satisfied, the track was flagged "confused."

The track's "on-off" status as determined by the Čerenkov algorithm is then compared with the track's momentum and the counter's particle threshold values. The momentum of each particle is assigned to one of seven momentum regions. The momentum assignments contain momentum regions from a particle threshold to its "effective" threshold. These effective thresholds differ from the true thresholds by

Table 3.2: ČERENKOV MOMENTUM REGIONS

REGION	MOMENTUM RANGE
1	0 GeV/c → pion threshold
2	pion threshold → 1.08 × pion threshold
3	1.08 × pion threshold → kaon threshold
4	kaon threshold → 1.08 × kaon threshold
5	1.08 × kaon threshold → proton threshold
6	proton threshold → 1.08 × proton threshold
7	1.08 × proton threshold → infinity

a Monte Carlo factor of 1.08. This factor results from the fact that no Čerenkov light is expected for a track which is exactly at the Čerenkov threshold. The seven Čerenkov momentum regions are shown in Table 3.2.

This momentum information as well as the track's "on-off" status are used to set a 4-bit status word hinting of the particle's identificaton:

- No bits "on" - The track is indeterminate;
- Bit 1 is "on" - The track is consistent with being an electron;
- Bit 2 is "on" - The track is consistent with being a pion;
- Bit 3 is "on" - The track is consistent with being a kaon;
- Bit 4 is "on" - The track is consistent with being a proton.

The 4-bit status works for each of the three Čerenkov counters are then logically AND-ed to form the Čerenkov identification variable, ISTATP. The possible values of ISTATP and their definitions are listed in Table 3.3.

The performance of the Čerenkov algorithm was tested on both data and Monte Carlo. In this analysis, the efficiency in the identification of kaons and pions is

Table 3.3: ISTATP VALUES AND DEFINITIONS

ISTATP	DEFINITION
0	inconsistent information
1	e^- definite
2	$\pi^\pm$ definite
3	$e^-/\pi^\pm$ ambiguous
4	$K^\pm$
7	$e^-/\pi^\pm/K^\pm$ ambiguous
8	proton definite
12	proton/$K^\pm$ ambiguous
14	$\pi^\pm/K^\pm$/proton ambiguous
15	confused information

Table 3.4: PARTICLE IDENTIFICATION EFFICIENCIES

PARTICLE	DATA SET	ϵ	MONTE CARLO	ϵ
$K^\pm$	$\phi^0 \to K^+K^-$	80%	$D_s^+ \to \phi^0\pi^+, \phi \to K^+K^-$	77%
$\pi^\pm$	$K_s^0 \to \pi^+\pi^-$	88%	$D_s^+ \to \phi^0\pi^+$	85%

most important since $D_s^+ \to \phi^0\pi^+ \to (K^+K^-)\pi^+$. This efficiency was measured both on data and Monte Carlo. Using a large sample of ϕ^0's and studying the decay $\phi^0 \to K^+K^-$ on data, the efficiency for identifying kaons was measured to be nearly 80% [24]. Similarly, a Monte Carlo sample of D_s^+ decaying to $\phi^0\pi^+$ with the ϕ^0's decaying to K^+K^- had a kaon identification efficiency of 77% (per kaon) [25]. The Čerenkov efficiency measured both on data and Monte Carlo for identifying kaon and pion tracks is displayed in Table 3.4.

CHAPTER 4

DATA ANALYSIS

All of the post-fire E687 data were analyzed to determine the lifetime of the charmed-strange meson, $D_s^{\pm}$, via the decay mode $D_s^{\pm} \rightarrow \phi^0\pi^{\pm}$, where $\phi^0 \rightarrow K^+K^-$. The Cabibbo-suppressed decay of the charmed meson, $D^{\pm}$, where $D^{\pm}$ decays to $\phi^0\pi^{\pm}$ was also studied to determine the $D^{\pm}$ lifetime. In this chapter, the cuts on the data used to extract the $D_s^{\pm}$ and $D^{\pm}$ signals are presented. The resulting signals are then studied in preparation for the lifetime measurements and to elucidate the nature of the D_s^+ and D^+ events. Unless otherwise specified, charge conjugate states are included when decay modes of a specific charge are discussed.

4.1 Data Reduction

Considering that PASS1 produced nearly 2400 nine-track tapes, the data set had to be reduced to a more manageable size. This was accomplished in two steps. First all of the data were analyzed by various skim routines to produce smaller samples for further analysis. Then one of these smaller samples was selected to extract events containing ϕ^0's.

Table 4.1: SKIM FLAGS AND STREAMS

SKIM FLAG	STREAM	EVENT CHARACTERISTIC
1	1	> 1 heavy present in the event
2	1	at least one oppositely charged heavy pair
3	1	K_s^0 and a heavy present
4	1	a pair of K_s^0's present
5	1	K^+K^- pair with ϕ^0 mass cut
6	2	global vertex χ^2
7	2	global vertex χ^2 and transverse mass cut
8	4	clean K_s^0
9	2	D meson skim
10	4	Λ present in the event
11	4	kink in the event
12-15	none	unassigned
16	3	VERTIC vertex
17	3	VERTIC vertex and mass cuts

4.1.1 E687 Skim Routines

As mentioned above, the 2400 reconstructed PASS1 tapes were reduced by applying various criteria to reduce the data set. This was accomplished by doing some rudimentary analysis on each event and writing a subset of the events to one or more skim streams. The goal was to create a series of data sets with total event samples not to exceed 20% of the total event sample. Within each skim stream, skim flags were assigned to events with specific characteristics. There were four skim streams containing thirteen skim flags. These are listed and described in Table 4.1, where the term "heavy" refers to a heavy particle such as a proton or kaon.

The skim stream used for this analysis was stream 1. The decay mode $\phi^0 \rightarrow K^+K^-$ was the motivation for selecting all events with pairs of oppositely charged "kaon consistent" tracks, as specified by Čerenkov identification, having invariant

masses within the ϕ^0 meson mass range (1020 $\pm$ 20 MeV/c^2). Skim stream 1 was composed of events that contained at least one pair of heavy particles (p, K^+, K^0_s). Those events of skim stream 1 that contained two oppositely charged kaon tracks were also assigned to the skim bit 4 substream. Skim stream 1 fell short of the reduction goals of 20% by reducing the total data set by a factor of 3.

All of the output tapes were to be processed over this subskim routine, but the skimming was stopped prematurely when a geometry problem in PASS1 was detected. It appeared that the geometry of the spectrometer, particularly that of the silicon microstrip detector, was not constant throughout the duration of the run. Some of the PASS1 tapes were fine but others had to be reconstructed once again (those data runs which occurred after this geometry shift but were processed with the old geometry).

Due to inefficiencies or known problems with the performance of some streams of the skim, a somewhat modified version of the skim was implemented. This new skimming routine was then used on both the remaining unskimmed PASS1 tapes and those that had to be reconstructed a second time. The same skimming algorithm was used for the ϕ^0 skim in both versions of the skim routines.

4.1.2 ϕ^0 Skim

By simply determining each PWC track's charge and Čerenkov identification, a fairly clean ϕ^0 signal was obtained by selecting all possible K^+K^- pairs, while also substantially further reducing the data sample. A charged track was labelled a kaon if the Čerenkov algorithm had identified it as "kaon definite" (ISTATP = 4) or "kaon-proton ambiguous" (ISTATP = 12). One other qualification was made for those tracks that had a momentum greater that 60 GeV/c. If the track was identified as "$e/\pi/K$ ambiguous" (ISTATP = 7) and had a momentum greater than

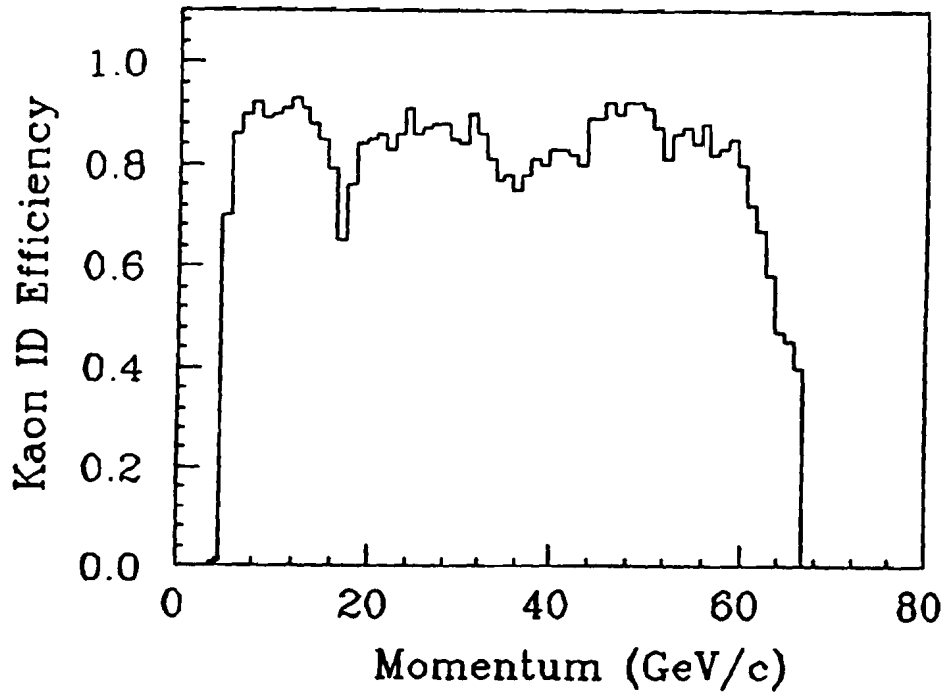

Figure 4.1: Kaon Identification as a Function of Momentum (as determined by Monte Carlo studies).

60 GeV/c (the C3 kaon threshold), it was considered to be a kaon candidate. This additional kaon definition picked up only a tiny fraction of kaon candidate tracks (a few percent).

In Fig. 4.1 is shown the range of momenta for charged tracks identified as "kaon consistent" in the E687 Čerenkov system. Determined by Monte Carlo studies (the characteristics of this sample are explained at the end of this chapter) and produced with 5 chamber tracks only, this plot shows that kaons can be identified in the momentum range between roughly 4 GeV/c and 65 GeV/c. The dips in the identification efficiency are threshold mismatches between the three Čerenkov counters.

Both kaon PWC tracks were required to link with microstrip detector tracks.

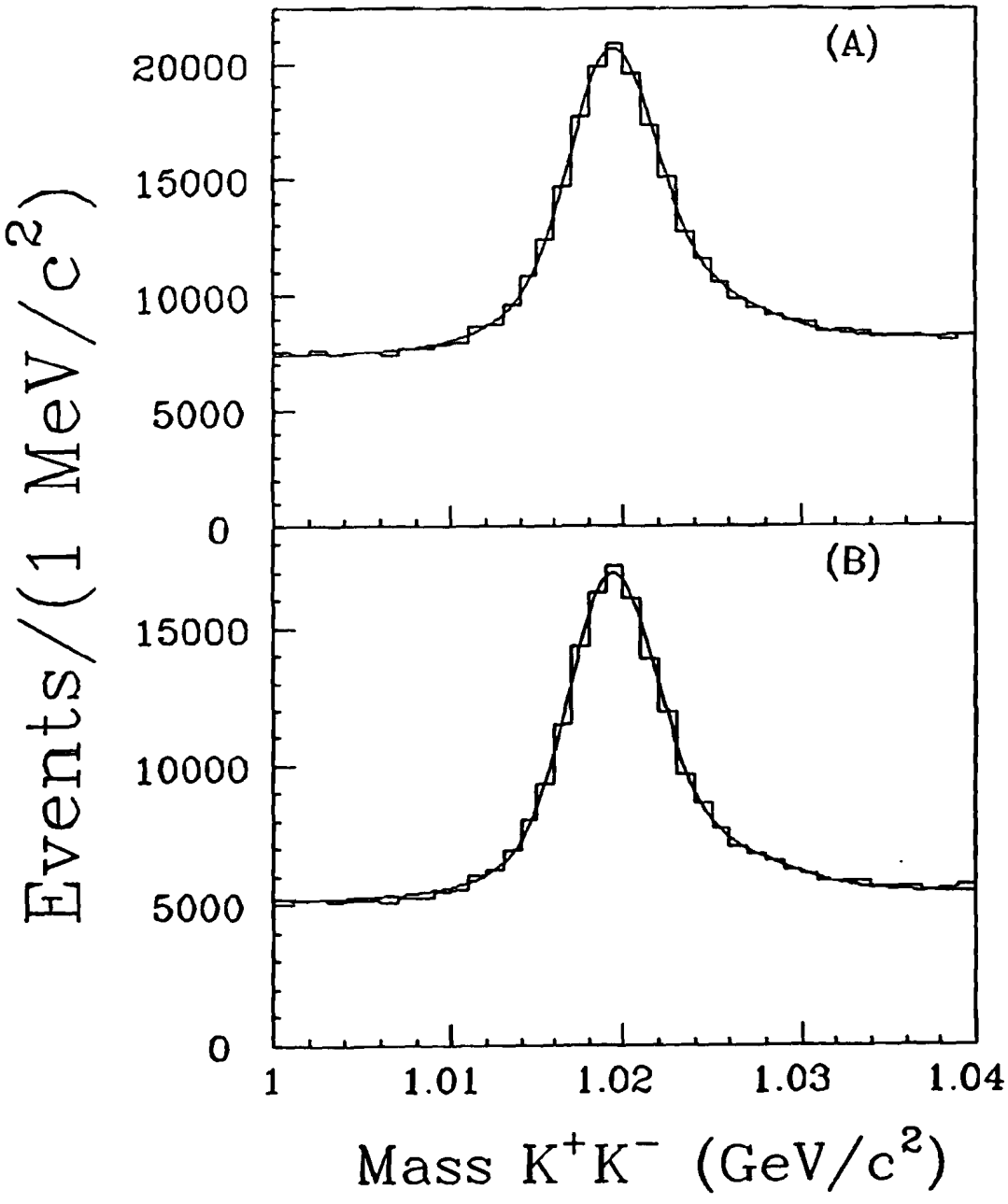

Figure 4.2: Phi Meson Study: (A) No linking requirement; (B) Both kaons required to link.

The invariant mass plots that resulted for all oppositely charged pairs of kaon tracks with and without a PWC-microstrip track link requirement are plotted in Fig. 4.2. These figures clearly show a ϕ^0 peak at 1020 GeV/c^2 for both the linked and unlinked K^+K^-. The fit parameters for these plots when the peaks were fitted with a P-wave Breit-Wigner function are listed in Table 4.2. Accepting all K^+K^- unlinked pairs of PWC tracks with invariant masses in the range 1.00 GeV/c^2 < $M_{K^+K^-}$ < 1.04 GeV/c^2 reduced the data set from 44 million events to 398 thousand events. Requiring both kaon tracks to link reduced the data set further to 300 thousand events. After an examination of Fig. 4.2, one can see that not all events are ϕ^0's. Even within the ϕ^0 mass range, there may be a non-resonant K^+K^- contribution as well as K^+K^- events resulting from the decays of other mesons.

One reason the Čerenkov cuts were successful in isolating ϕ^0 candidates was the good efficiency of the Čerenkov system for identifying kaons and thereby allowing excellent pion rejection. These Čerenkov efficiencies were discussed in Chapter 3.

Table 4.2: PHI FIT PARAMETERS

DATA SET	NUMBER OF ϕ^0's	MASS (MeV/c^2)	Γ (MeV/c^2)	S/B
NO LINK	98980	1019.54 ± .02	6.1 ± 0.1	0.63
LINK	89840	1019.52 ± .02	5.8 ± 0.1	0.84

4.2 Signal Extraction

After the 300 thousand events containing one or more K^+K^- pairs of linked tracks were obtained, a tighter mass cut on the K^+K^- pair of 1020 ± 10 MeV/c^2 was applied. The kaon pairs of this new data set were then combined with each available pion track in the event. These pions were required to be linked tracks and to be

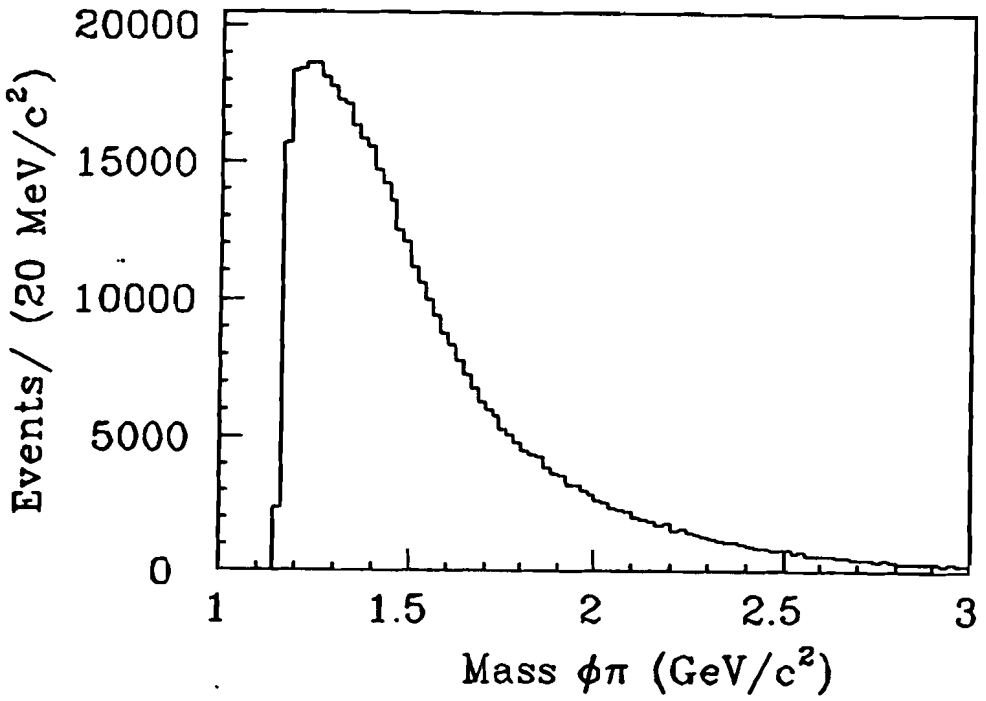

Figure 4.3: The $\phi\pi^+$ Invariant Mass.

identified as "pion consistent" by the Čerenkov system. This basically required the pion candidate track not to be identified an as electron, kaon or proton (ISTATP $\neq$ 1, 4, 8, 12). The invariant mass plot of all possible $\phi^0\pi^+$ combinations is exhibited in Fig. 4.3. As can be clearly seen from this figure, more cuts were necessary to suppress the background and extract the signals. These analysis cuts were separated into two major categories: vertex cuts and kinematic cuts.

4.2.1 Vertex Considerations

Keeping events that pass minimum separation cuts between primary and secondary vertices is one effective means to extract charmed particle signals. At the primary vertex, the charmed particle is created and then it subsequently decays at a secondary vertex. For the decays under study, $D_s^+ \rightarrow \phi^0\pi^+$ and $D^+ \rightarrow \phi^0\pi^+$, the

secondary vertex will contain the charged track trio, $K^+K^-\pi^+$, due to the strong decay of the ϕ^0 resonance.

One technique to determine these vertices and measure their separation is to first identify the tracks that form the secondary vertex. Known as a "candidate driven" vertex algorithm because the particular decay tracks are first selected, this vertexing technique (utilizing a routine called DVERT [26]) uses the charm candidate as a seed to find the primary vertex. Using the full covariance matrices of each decay track to generate the charm candidate track, DVERT then loops over all of the linked microstrip tracks. Those tracks that form a vertex with the seed track and have a fit confidence level greater than 0.02 are retained in a list. The pair with the best fit confidence level is selected as forming the primary vertex. The remaining tracks in the list are checked for their consistency with coming from the primary vertex. For each consistent track, the primary vertex is recalculated. After the primary and secondary vertices have been fitted, DVERT performs a global fit to the decay tracks to find the 3-dimensional decay length, L, as well as the error in this quantity, σ_L. This procedure can fail if there are not enough good tracks or no tracks are consistent with forming a primary.

The efficiency of DVERT as determined by Monte Carlo studies will be discussed in the last section of this chapter. Its performance in data has been studied on the decay $D^{*+} \rightarrow D^0\pi^+ \rightarrow (K^-\pi^+)\pi^+$ yielding a 90% efficiency [20]. The precision in the calculation L/σ_L has also been studied [20].

For charmed particle extraction, the variable examined is not the separation of the vertices but the quantity, L/σ_L, the separation divided by the error in this separation. The distribution of L/σ_L for the subset of 300 thousand K^+K^- events where DVERT succeeds in determining a primary and secondary (roughy 270 thousand events) is shown in Fig. 4.4. This plot shows a peak and then a tail. Background

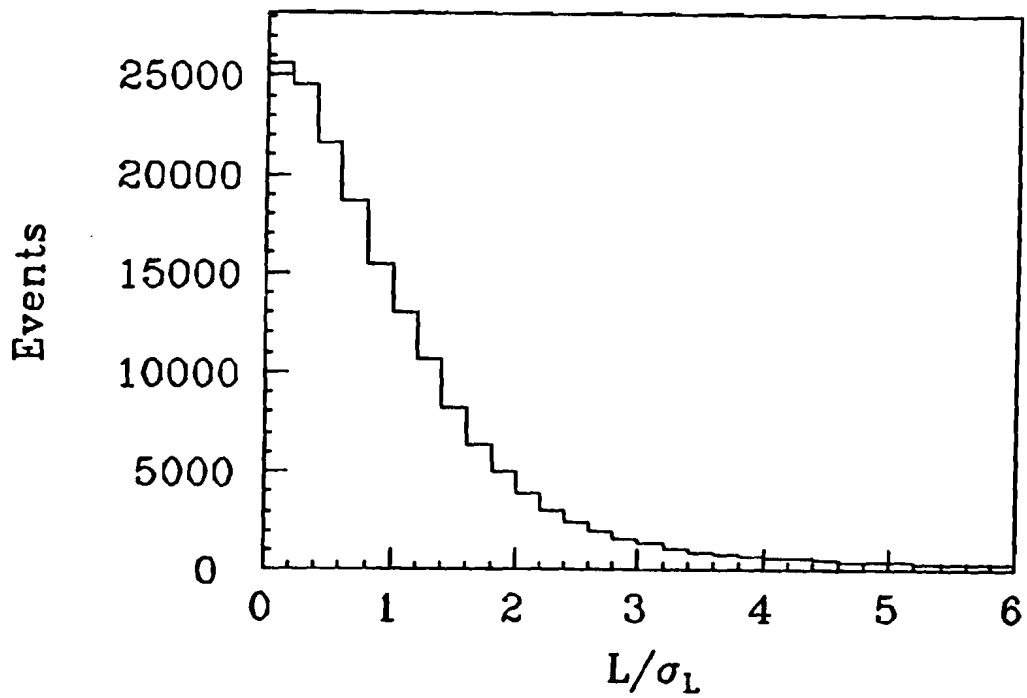

Figure 4.4: Distribution of L/σ_L .

can be suppressed and charmed particles thereby extracted by retaining events with high values of L/σ_L .

In Fig. 4.5 is shown the distribution in separation, L, between the primary and secondary vertices for all $K^+K^-\pi^+$ events (where DVERT succeeded in determining a primary and secondary vertex), as well as those where the secondary vertex is required to be downstream of the primary. It should be noted that DVERT can and does produce secondary vertices upstream of the primary. This is a consequence of the "candidate driven" algorithm where the user may have selected a group of presumed secondary vertex tracks that were actually the tracks of some upstream, possibly primary, vertex. If this occurs, DVERT assigns a negative value to the quantity, L [1]. A cut will be made that requires that the secondary be downstream

[1] It also assigns a negative value to L/σ_L.

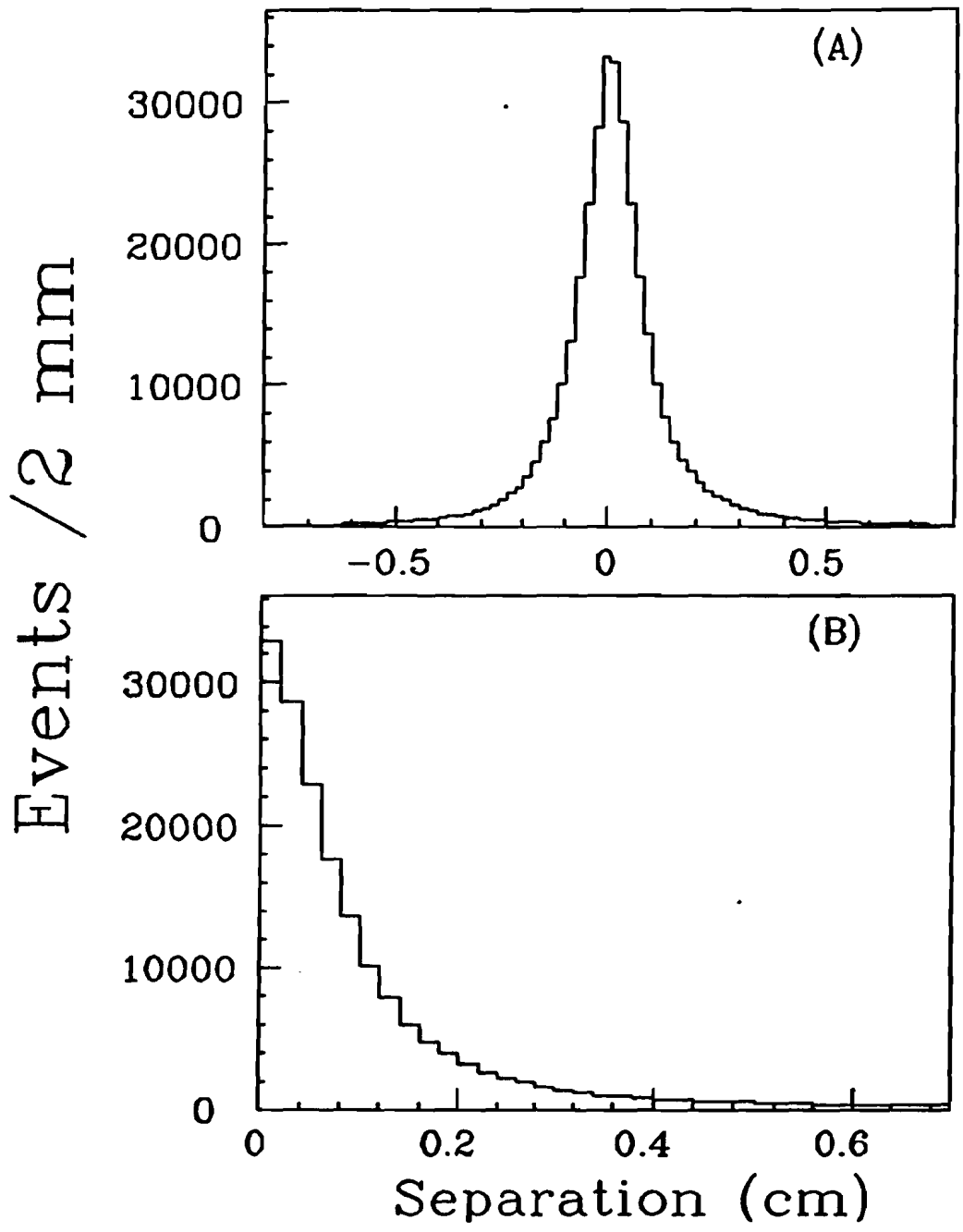

Figure 4.5: Separation, L, between Primary and Secondary Vertices: (A) All values (B) Values > 0 only.

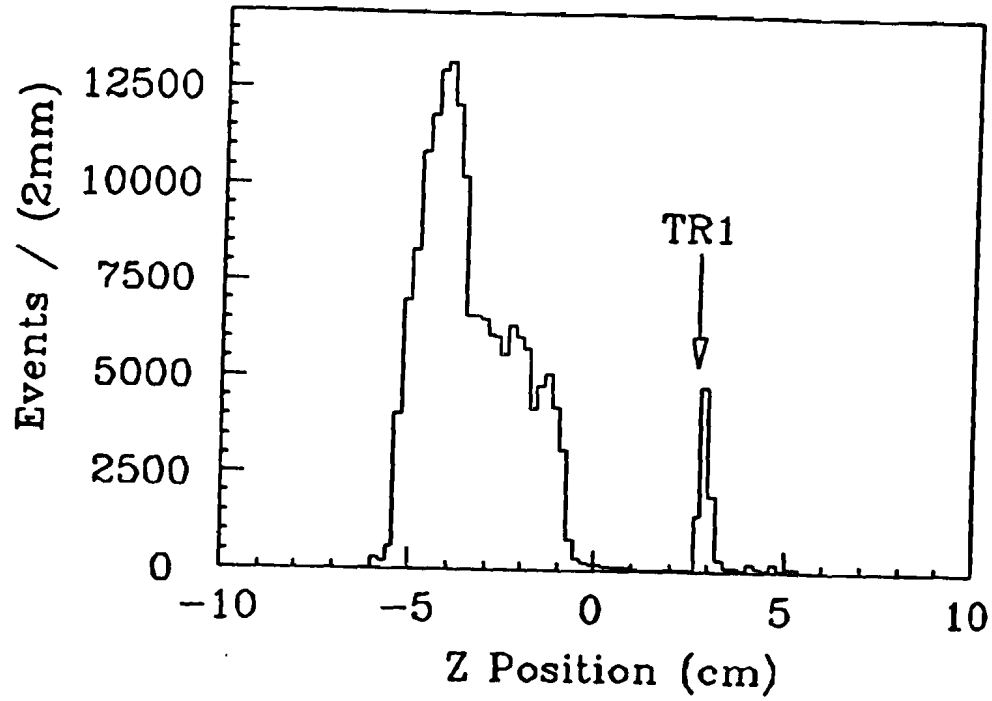

Figure 4.6: Secondary Vertex Z-coordinate Position ($L/\sigma_L > 0$).

of the primary.

For photon-hadron interactions, the primary vertex should occur within the target region. No secondary vertices in materials downstream will be accepted, so as to avoid "false" secondaries that are actually daughter particles interacting hadronically with material in the beam. The Z-coordinate positions of the secondary vertices where the secondary was required to be downstream of the primary are shown in Fig. 4.6. From this figure, it is seen that a substantial number of candidate charm events appeared to decay in TR1, a scintillation counter located upstream of the microstrip detector at Z = +2.7 centimeters (discussed in Chapter 2). These were removed from the data set.

In Fig. 4.7 is displayed the distribution of χ^2/DOF of the secondary vertex fit for the $\phi^0\pi^+$ events. After some Monte Carlo studies, a χ^2/DOF less than 3 was

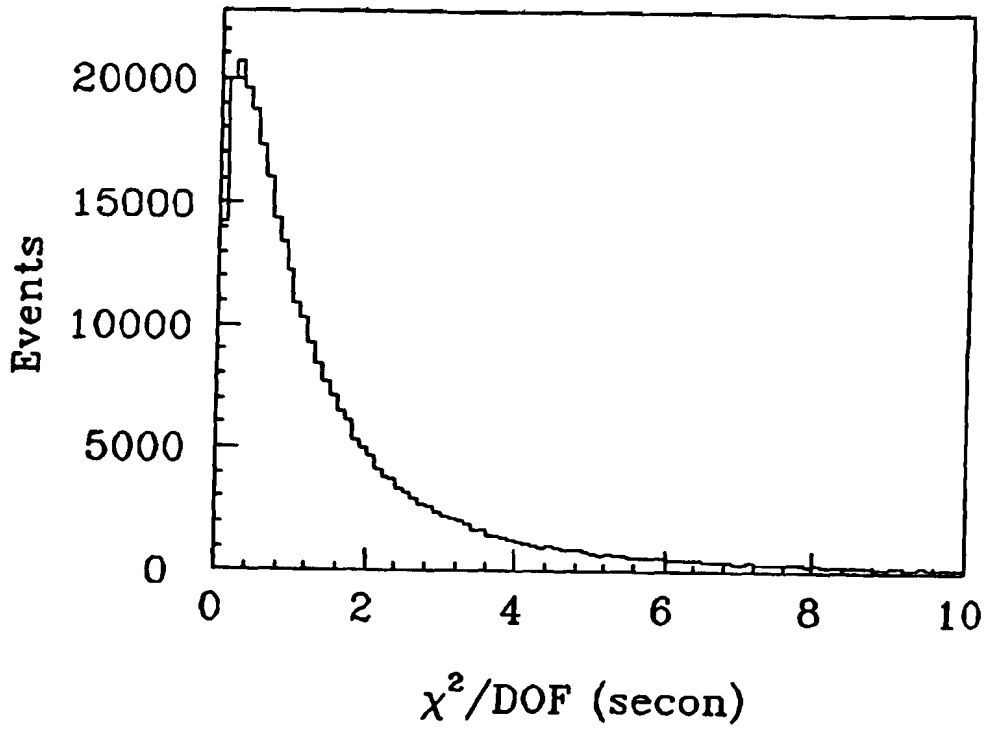

Figure 4.7: Distribution of χ^2/DOF for the Secondary Vertices.

chosen as a criterion for the secondary vertex. Thus the final vertex cuts were:

- The primary vertex was required to be located in target region (-5.5 cm < Z_{prim} < -1.0 cm);
- No secondary vertices were permitted in the downstream scintillation counter TR1 (+2.6 cm < Z_{secon} < +3.2 cm, not permitted);
- The value of χ^2/DOF for the secondary vertex was required to be less than 3;
- The secondary vertex Z-coordinate position was required to be downstream of the Z-coordinate position of the primary;
- Cuts were made on the separation divided by the error in this separation between primary and secondary, L/σ_L , such that this quantity was greater than 2, 3, 4 or 5.

4.2.2 Kinematic Requirement

The second category of cuts was kinematic in nature. In the decay, $D_s^+ \rightarrow \phi^0\pi^+$, a pseudoscalar meson decays to a vector meson and a pseudoscalar meson. By conservation of angular momentum, the angle θ measured between one of the daughter kaons of the ϕ^0 and the pion in the rest frame of the vector meson (ϕ^0) will have a distribution proportional to $\cos^2\theta$. Since the E687 spectrometer has a flat acceptance in θ, the forward/backward peaking of the $\cos\theta$ distribution was expected. This was observed in the data as shown in Fig. 4.8. This distribution was also incorporated into the Monte Carlo. The $\cos\theta$ distribution for Monte Carlo events is plotted in Fig. 4.8(A), while this variable is plotted for a sample of D_s^+ data events (mass cut of 1.94 GeV/c^2 to 1.99 GeV/c^2 ; $L/\sigma_L > 3$) in Fig. 4.8(B). In Fig 4.8(C)is displayed the $\cos\theta$ distribution for mass regions outside both the D_s^+ and D^+ signals indicating no $\cos\theta$ distribution. After examining Fig. 4.8(A), a cut of $\cos\theta > 0.3$ was made on the events. This cut retained nearly 97% of the signal and removed about 30% of the background events in the D_s^+ mass region. A comparison of the $\phi^0\pi^+$ events ($L/\sigma_L > 3$ and all other analysis cuts) with and without a $\cos\theta$ (> 0.3) cut is shown in Fig. 4.9.

When all of the above cuts were applied to the data set and the L/σ_L cut was varied, the plots of Fig. 4.10 resulted. Both the D_s^+ (1.970 GeV/c^2) and the Cabibbo-suppressed decays of the D^+ (1.870 GeV/c^2) events can be seen in the mass plots. The signal regions were fit with Gaussians, while the background was fit with a linear polynomial. In Table 4.3 are displayed the fit results for the $L/\sigma_L > 3$ sample showing mean masses consistent with world averages [6]. The analysis cuts made on the data for the skims and final analysis are recapitulated in Table 4.4. The event yields after each cut are listed in Table 4.5.

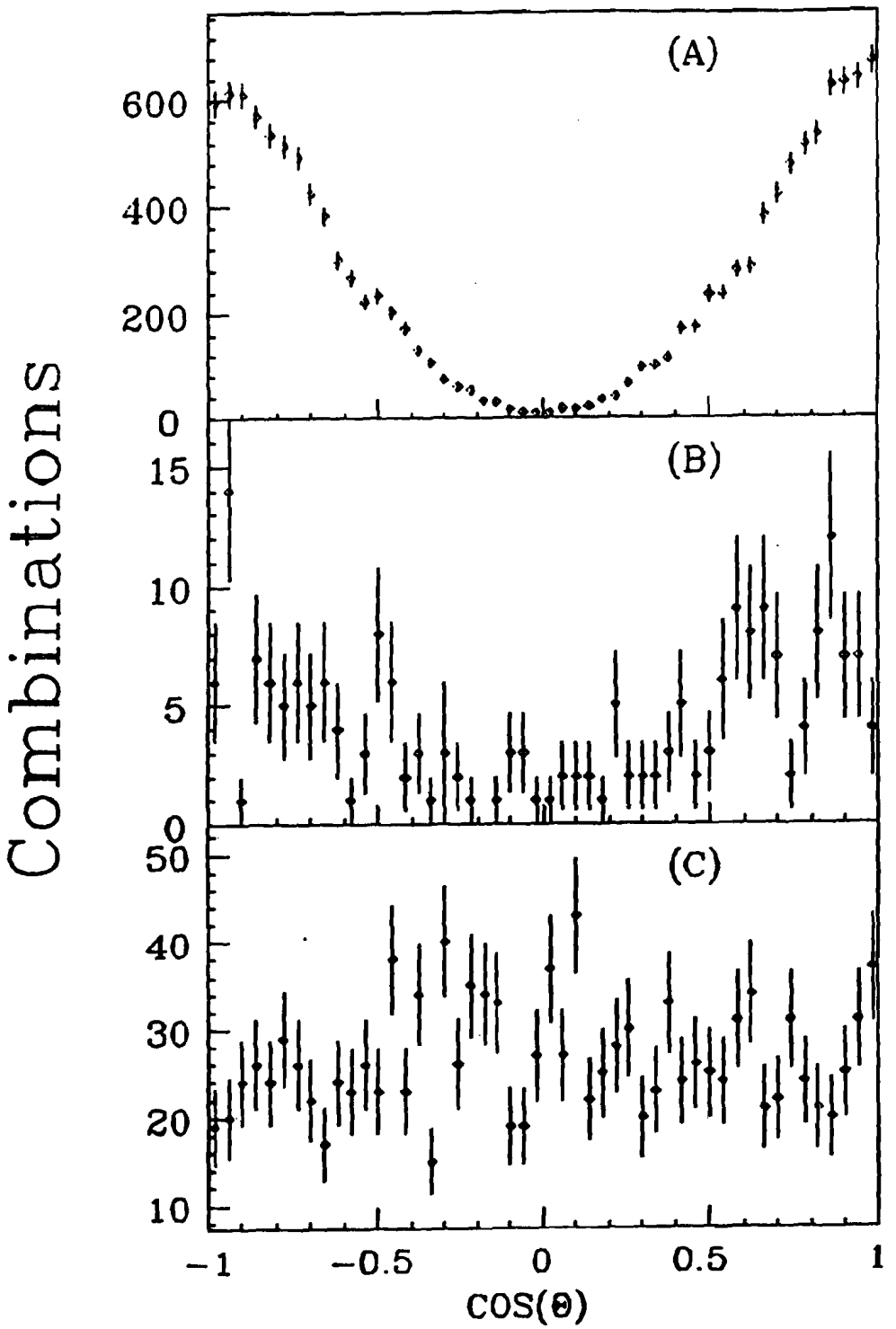

Figure 4.8: The $\cos\theta$ Distributions: (A) Monte Carlo; (B) D_s^+ signal region; (C) Mass regions outside the signals.

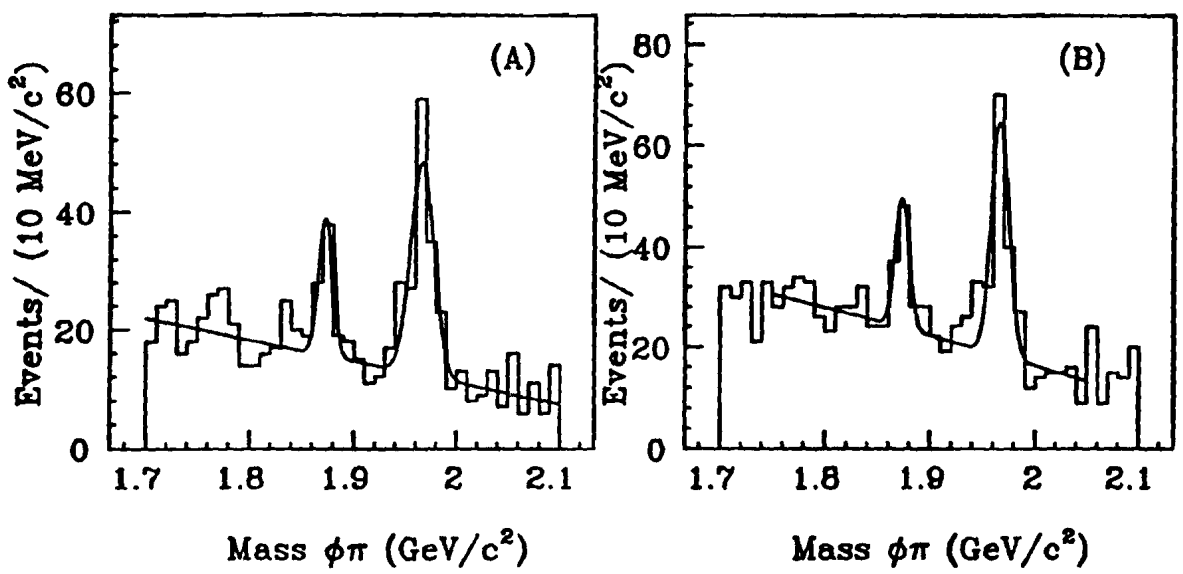

Figure 4.9: $\phi^0\pi^+$ Mass Distributions: (A) With a $\cos\theta > 0.3$ cut; (B) Without a $\cos\theta$ cut.

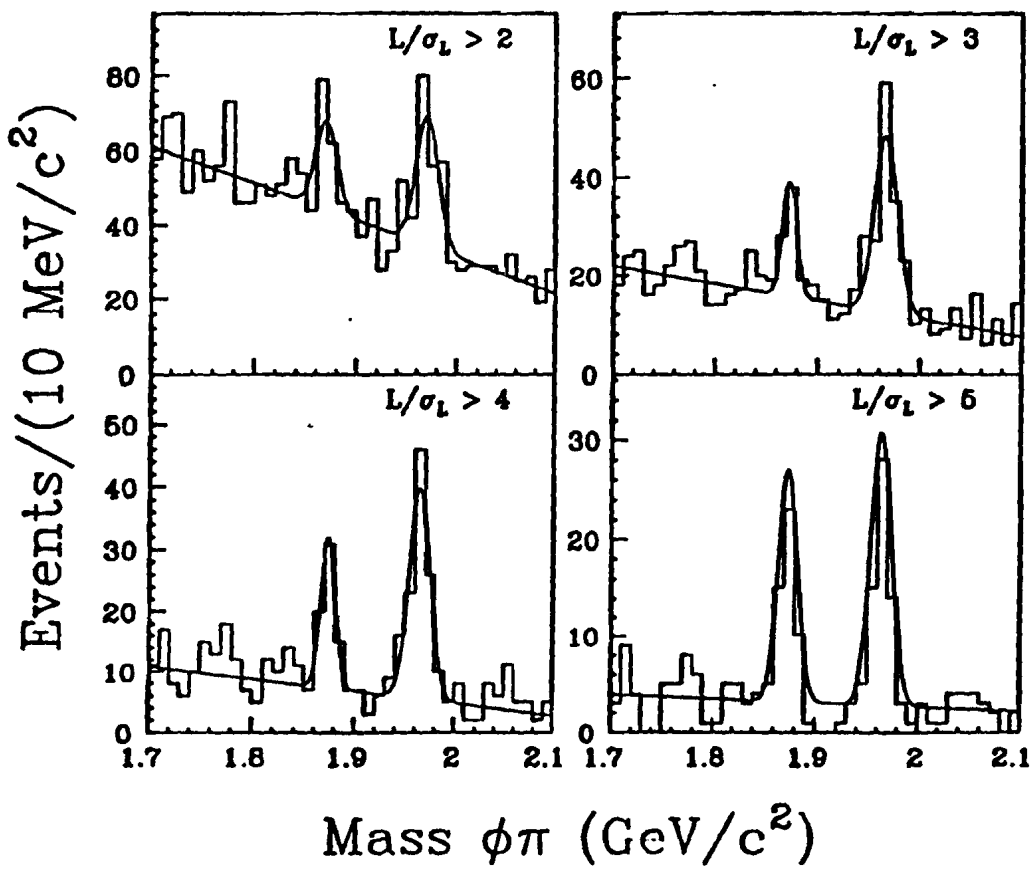

Figure 4.10: Fitted $\phi\pi^+$ Invariant Mass Distributions for Various L/σ_L Cuts.

Table 4.3: SIGNAL FIT PARAMETERS

QUANTITY	D_s^+	D^+
CUT	$L/\sigma_L > 3.$	$L/\sigma_L > 3.$
MASS (MeV/c^2)	1967 ± 2	1871 ± 2
σ (MeV/c^2)	11.1 ± 2.6	7.4 ± 3.7
NUMBER OF EVENTS	104 ± 15	50 ± 10
SIGNAL/BACKGROUND	2.5	1.6

Table 4.4: CUTS USED TO EXTRACT D_s^+ AND D^+ SIGNALS

CUT	SKIM	ϕ SKIM	ANALYSIS
ČERENKOV REQUIREMENTS	$\geq 2K^{\pm}$	K^+K^-	$K^+K^-\pi^+$
ϕ INVARIANT MASS(GeV/c^2)	—	$[1.0, 1.04]$	$[1.01, 1.03]$
LINKING (PWC-MICROSTRIP)	—	—	$K^+K^-\pi^+$
PRIMARY VERTEX LOCATION	—	—	*within target*
χ^2/DOF (SECONDARY VERTEX)	—	—	$< 3.$
$\lvert \cos\theta_{K\pi} \rvert$	—	—	> 0.3
$L/\sigma_L > N$ (D_s^+)	—	—	$N = 3$
$L/\sigma_L > N$ (D^+)	—	—	$N = 3$

Table 4.5: EVENT YIELDS AS A FUNCTION OF CUTS

CUT	EVENT YIELDS
TOTAL TRIGGERS	60,000,000
RECONSTRUCTED DATA ($\geq$2 *tracks in PWC*)	44,000,000
$\geq$2 (p, K or K^0_s) IN THE EVENT	15,000,000
1.00 GeV/c^2 < $M_{K^+K^-}$ < 1.04 GeV/c^2	400,000
1.01 GeV/c^2 < $M_{K^+K^-}$ < 1.03 GeV/c^2 (*linking of* K^+K^- *required*)	300,000
DVERT SUCCEEDS	167,000
PRIMARY VERTEX IN TARGET	127,000
χ^2/DOF < 3. (*secondary vertex*)	89,000
$\lvert \cos\theta_{K\pi} \rvert > 0.3$	82,000
$L/\sigma_L > 0.$	31,000
$L/\sigma_L > 1.$	8,700
$L/\sigma_L > 2.$	3,000
$L/\sigma_L > 3.$	1,600
$L/\sigma_L > 4.$	1,000

4.3 Signal Study

The $\phi^0\pi^+$ events surviving a cut of $L/\sigma_L > 3$ (and all of the other analysis cuts) were chosen for the lifetime measurements of the $D_s^+$and D^+ mesons. From Table 4.3 it is seen that a fairly high signal to background and event yield resulted for this cut on both particle states.

In order to measure the lifetime of a particle, the distribution of proper time is needed. The proper time is measured for a length L, the distance between the primary vertex and the secondary, as

$$\tau = L/\gamma v \tag{4.1}$$

where γv for the particle is,

$$\gamma v = p/m \tag{4.2}$$

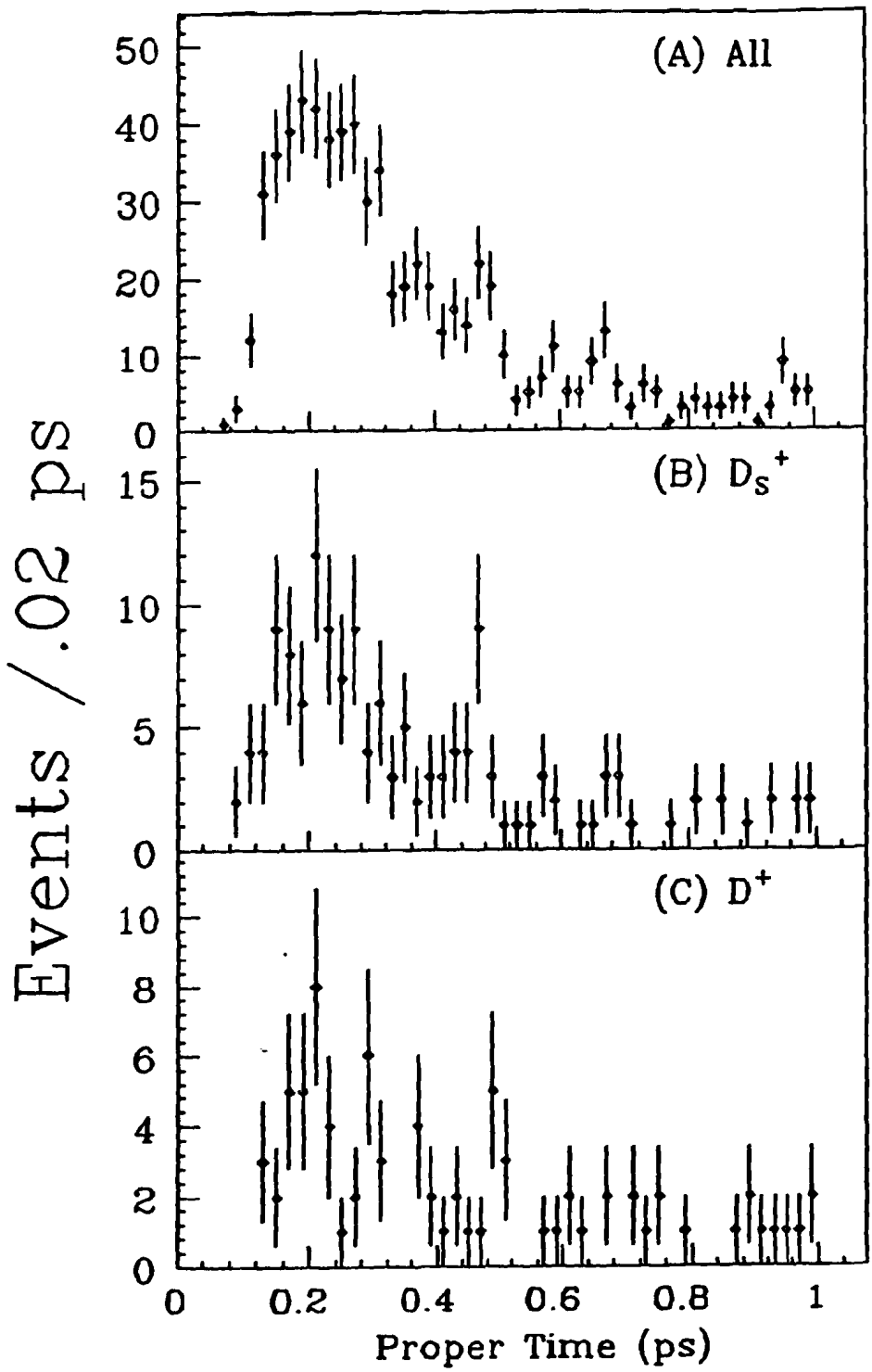

Figure 4.11: Proper Time Distributions: (A) All events; (B) D_s^+ events; (C) D^+ events.

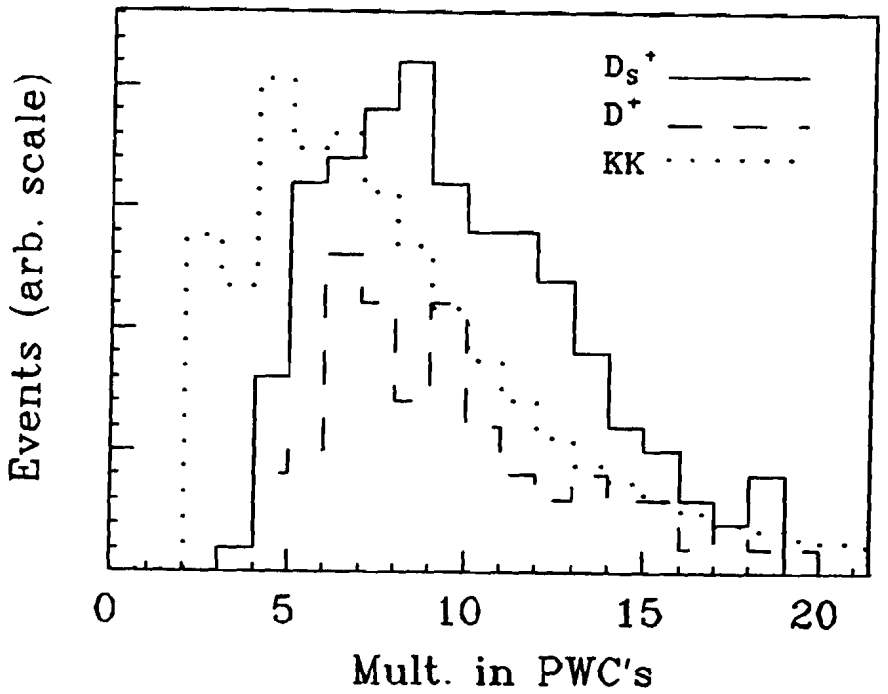

Figure 4.12: Multiplicity of Charged Tracks in the PWC's.

(where p is the particle's momentum and m its mass.) In Fig. 4.11(A) is exhibited the proper time distribution for the $\phi^0\pi^+$ invariant mass range from 1.7 GeV/c^2 to 2.1 GeV/c^2 with the $L/\sigma_L > 3$ cut. The proper time distribution for the D_s^+ sample (mass cut 1.94 GeV/c^2 to 1.99 GeV/c^2 and $L/\sigma_L > 3$) is shown in Fig. 4.11(B) and the proper time distribution for the D^+ sample (mass cut 1.85 GeV/c^2 to 1.90 GeV/c^2 and $L/\sigma_L > 3$) is shown in Fig.4.11(C). These distributions will be analyzed in the next chapter to extract the D_s^+ and D^+ lifetimes.

Several characteristics of the D_s^+ ($L/\sigma_L > 3$) and D^+ samples ($L/\sigma_L > 3$) are shown in the following series of plots:

1. The multiplicity distributions of charged tracks in the PWC's compared to the 400,000 event K^+K^- sample are shown in Fig. 4.12. Both the D_s^+ and D^+ samples had multiplicity distributions peaked at values greater than the overall K^+K^- sample.

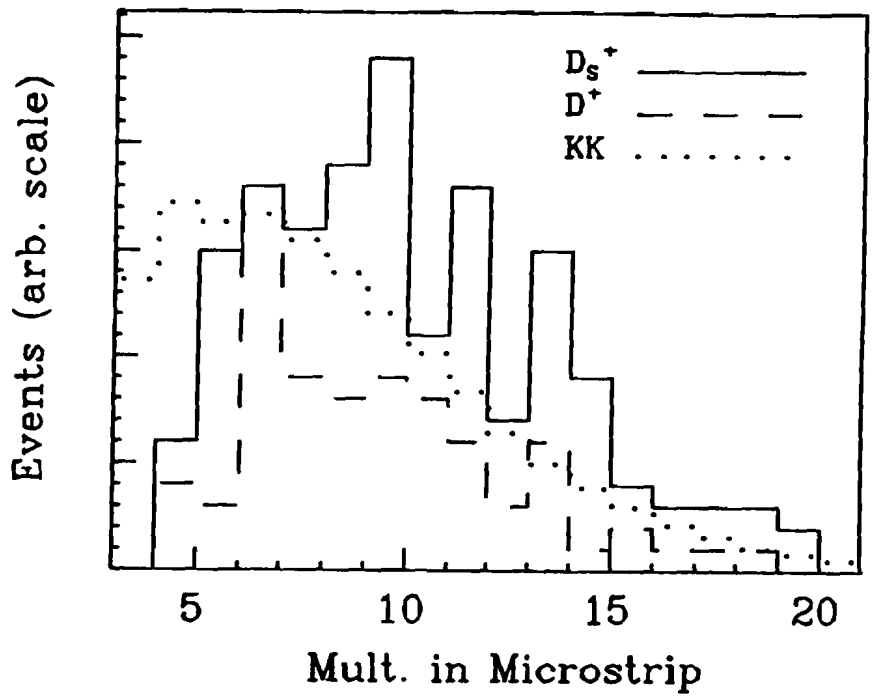

Figure 4.13: Multiplicity of Charged Tracks in the Microstrip Detector.

2. The multiplicity distributions of charged tracks in the microstrip detector compared to the 400,000 K^+K^- sample are shown in Fig. 4.13. Here too the charmed particle samples had multiplicity distributions peaked at values greater than the overall K^+K^- sample.

3. The multiplicity distributions of charged tracks at the primary vertex are displayed in Fig. 4.14. One notes that a fairly high percentage of events resulted from just one track, as well as the projected charmed particle track, forming the primary vertex. This was one advantage of the "candidate driven" vertex algorithm, where the charmed particle vector could be used along with a solitary track to form the primary vertex.

4. The distribution in the separation between primary and secondary vertices,

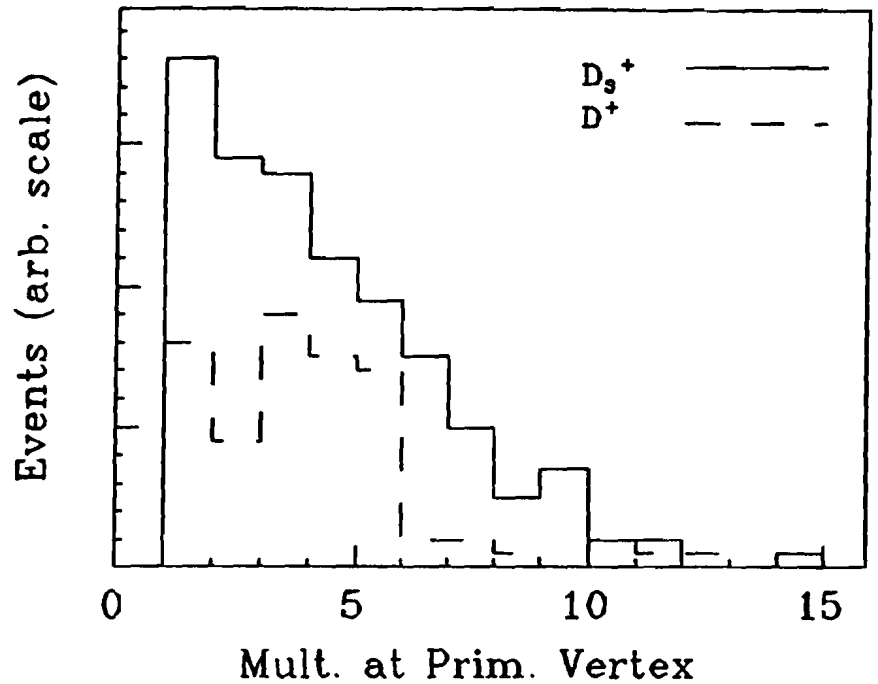

Figure 4.14: Multiplicity of Charged Tracks at the Primary Vertex.

L, as well as the error in this separation, σ_L, are shown in Fig. 4.15.

5. The momentum distributions for the D_s^+ and D^+ are shown in Fig. 4.16.

6. The resulting ϕ^0 mass distributions are shown in Fig. 4.17.

7. The photon energy distributions of the samples compared to the photon energy distribution for the total 400,000 ϕ^0 data set are shown in Fig. 4.18.

The mean values of these quantities are given in Table 4.6.

It is interesting to compare the yield of D_s^+ events to that of D_s^- events (or D^+ versus D^-). The $\phi^0\pi^+$ mass plots for positive particles versus negative particles for both $L/\sigma_L > 3$ and $L/\sigma_L > 4$ are shown in Fig. 4.19. The fitted yields for these plots, as well at for higher values of L/σ_L , are listed in Table 4.7. The background was fit with a second order polynomial, since a linear background did not fit the background mass distribution adequately. Within the errors of the fits, there seemed

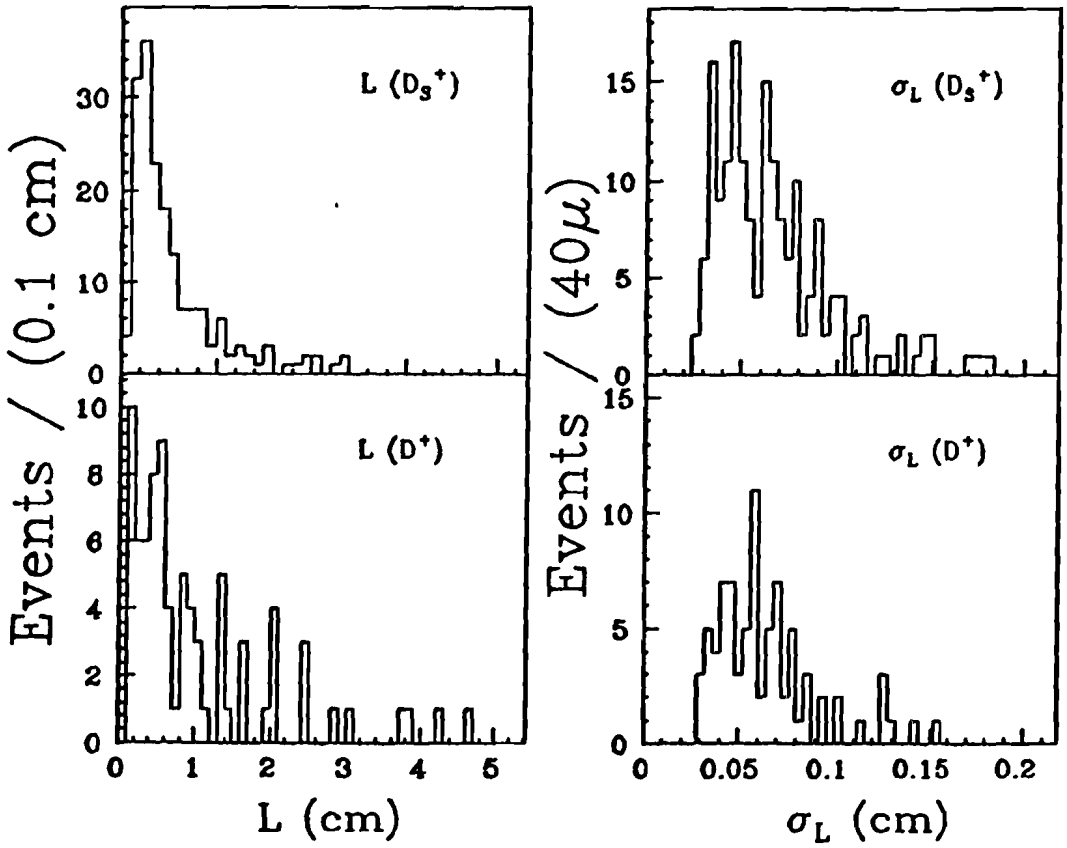

Figure 4.15: L and σ_L for D_s^+ and D^+ Samples.

Table 4.6: MEAN VALUES OF EVENT CHARACTERISTICS

Characteristic	D_s^+	D^+	ALL K^+K^- (400K)
MULT. IN PWC'S	9.99	9.50	5.41
MULT. IN MICROSTRIP	10.04	9.28	7.48
MULT. AT PRIM. VERTEX	4.36	4.14	—
MOMENTUM OF PARTICLE (GeV/c)	68.71	69.70	—
RESH PHOTON ENERGY (GeV/c^2)	224.4	226.1	221.9

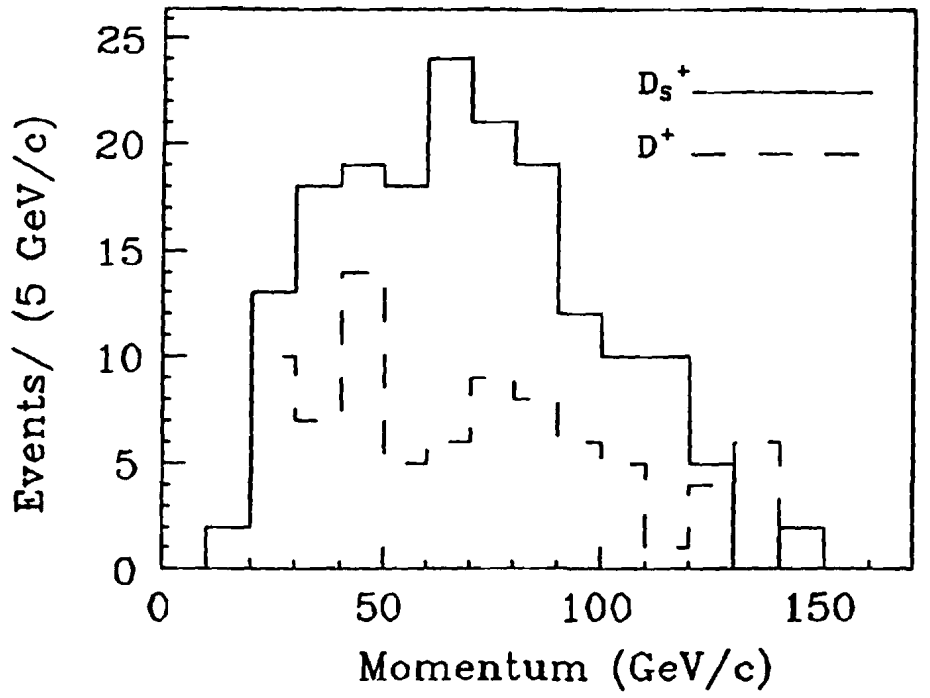

Figure 4.16: Momentum Distributions of D_s^+ and D^+ Events.

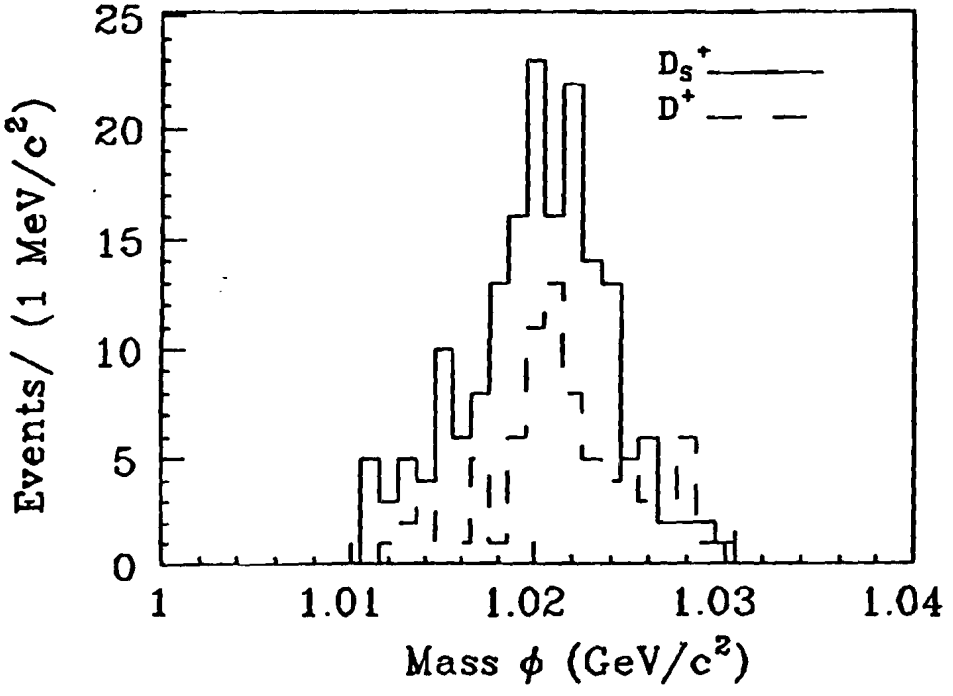

Figure 4.17: Resulting ϕ^0 Mass after Cuts.

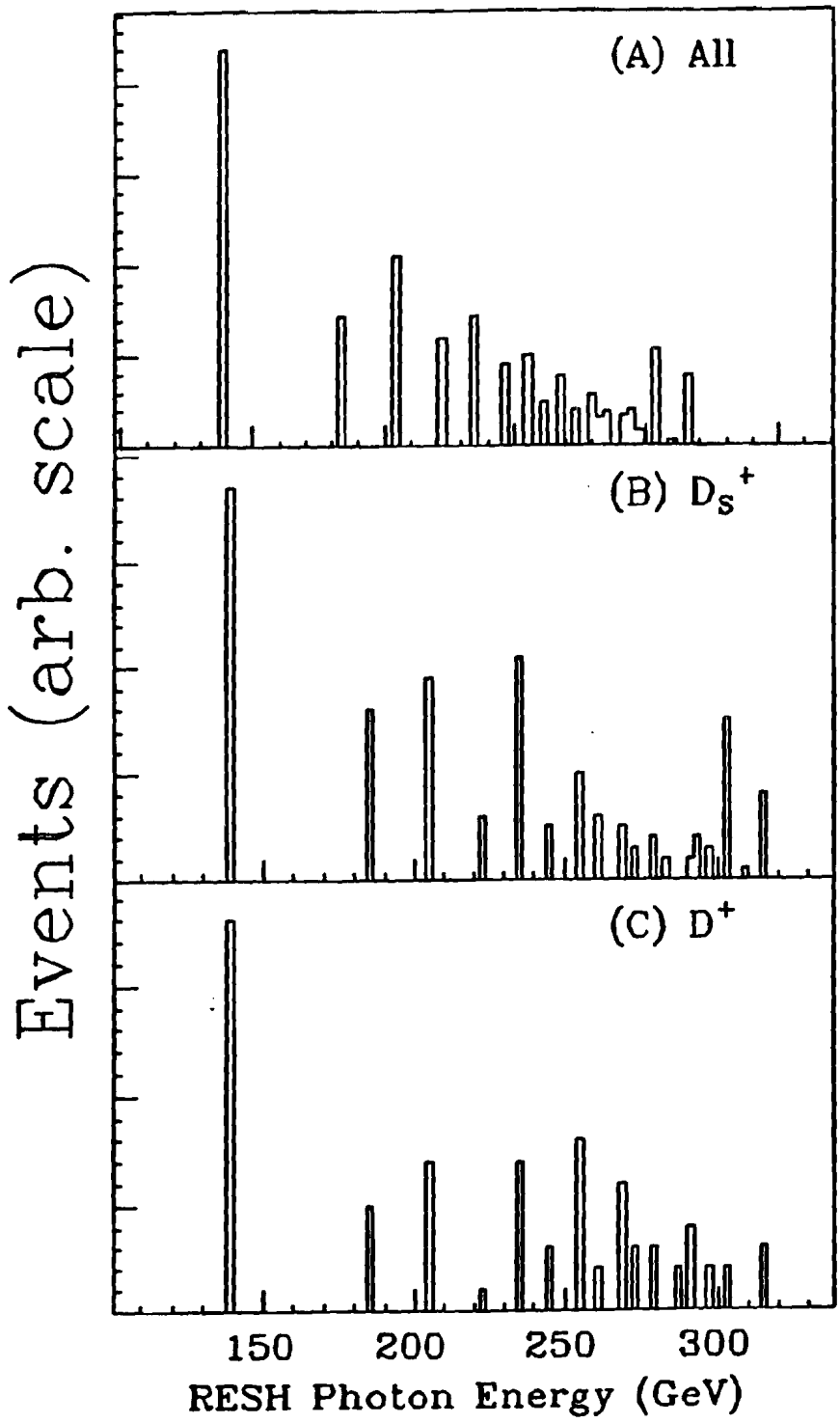

Figure 4.18: RESH Photon Energy Distributions: (A) All events; (B) D_s^+ events; (C) D^+ events.

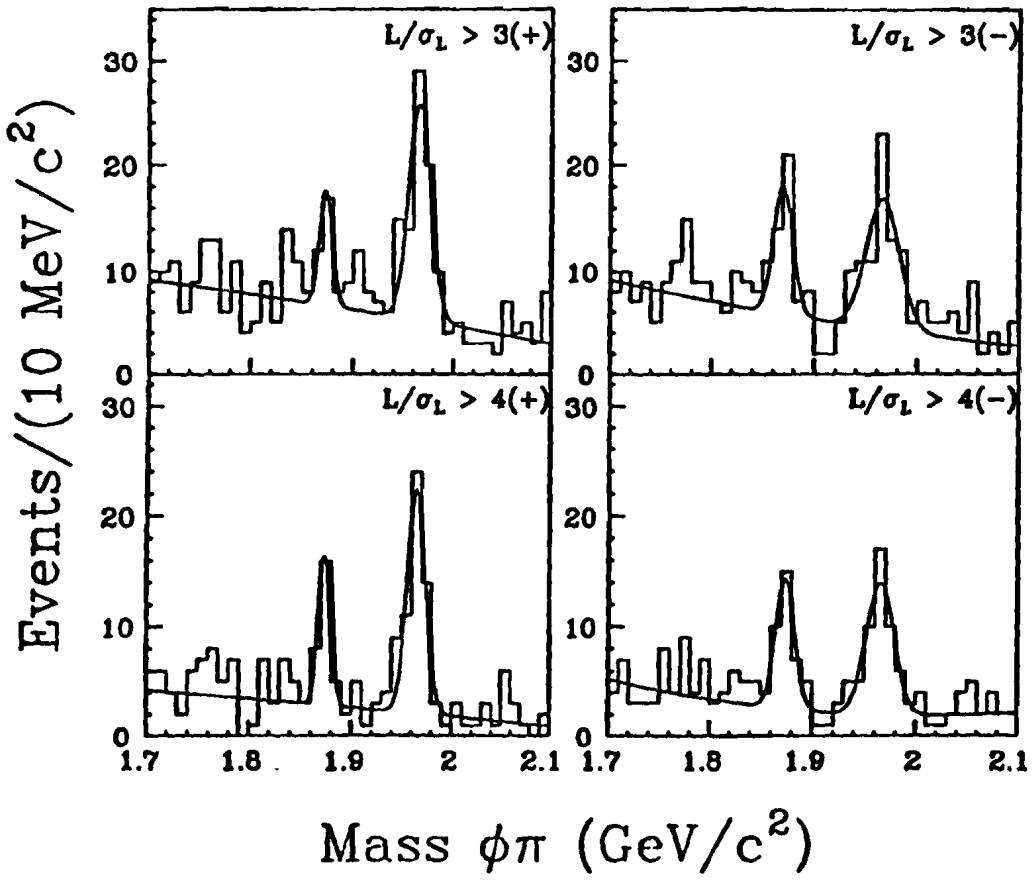

Figure 4.19: A Comparison of Charged Modes of the D_s^+ and D^+ for $L/\sigma_L > 3$ and $L/\sigma_L > 4$.

Table 4.7: COMPARISON OF THE YIELDS OF CHARGED MODES

L/σ_L CUT	D_s^+	D_s^-	D^+	D^-
>3	57±10	57±10	16±6	27±7
>4	47±7	36±7	21±6	24±7
>5	38±7	20±5	17±5	28±7
>6	28±6	18±5	14±5	24±6

to be no charge asymmetry in the D_s^+ or the D^+ samples.

4.4 Efficiency Study

In order to study the efficiency of the various cuts on the data set, one must have a large Monte Carlo data set that resembles the data set as much as possible. The following event topology was generated in the creation of the Monte Carlo (MC) sample: $\gamma g \rightarrow D_s^+ \bar{C} \rightarrow (\phi^0 \pi^+)\bar{C} \rightarrow (K^+K^-\pi^+)\bar{C}$, where '$\bar{C}$' represents "charmbar" or any charmed particle that balanced all quantum numbers and followed all conservation rules. The "charmbar" particle can be either a charmed meson or baryon and decays according to the world averages [6] of branching ratios to any established decay mode.

The Monte Carlo (MC) program, ROGUE, was developed at the University of Illinois [27] and uses Photon-Gluon Fusion [3] as the framework to generate charmed particles from the interations of the photon beam and the hadronic material of the target. The geometry of the E687 spectrometer as well as its performance were simulated in the Monte Carlo.

A comparison was made of several characteristics of the MC data set to the D_s^+ event sample in the data. The D_s^+ sample consisted of events from the $L/\sigma_L >$ 5 sample requiring the $\phi^0\pi^+$ mass to be between 1.94 GeV/c^2 and 1.99 GeV/c^2 .

The $L/\sigma_L > 5$ sample was chosen because of its low background levels compared to the $L/\sigma_L > 3$ sample, although it also contained a smaller number of events.

In Fig. 4.20 are shown the comparisons between the data and Monte Carlo samples in the distribution of charged track multiplicities in both the microstrip and PWC system, the number of vertices found in the microstrip by the SSD reconstruction routine and the number of charged tracks at the primary vertex. The PWC and microstrip multiplicities for the Monte Carlo set are on average nearly one track short of the average PWC and microstrip multiplicities found in the data. This may be due to inadequate simulation of the hadronic background in the Monte Carlo data set.

The comparison between data and Monte Carlo is continued in Fig. 4.21 with plots of the D_s^+ momentum distributions. The mass resolutions of the D_s^+ signal for the $L/\sigma_L > 5$ events in both data sets are compared in Fig. 4.22 with the fit results displayed in Table 4.8. Although statistically inferior in comparison to the Monte Carlo set, the $L/\sigma_L > 5$ data set showed reasonable similarities to its MC counterpart.

The efficiency of each of the analysis cuts was then studied on a large sample of Monte Carlo events. The cuts applied to the data to produce the charm signals were studied in the following order:

1. The Master Gate was satisfied in the event;

2. The second level trigger was satisfied in the event;

3. All three particles ($K^+K^-\pi^+$) were identified by the Čerenkov system;

4. The ϕ^0 mass cut was satisfied (1.01 GeV/c^2 $< M_{K^+K^-} <$ 1.03 GeV/c^2 and both kaon tracks were required to link);

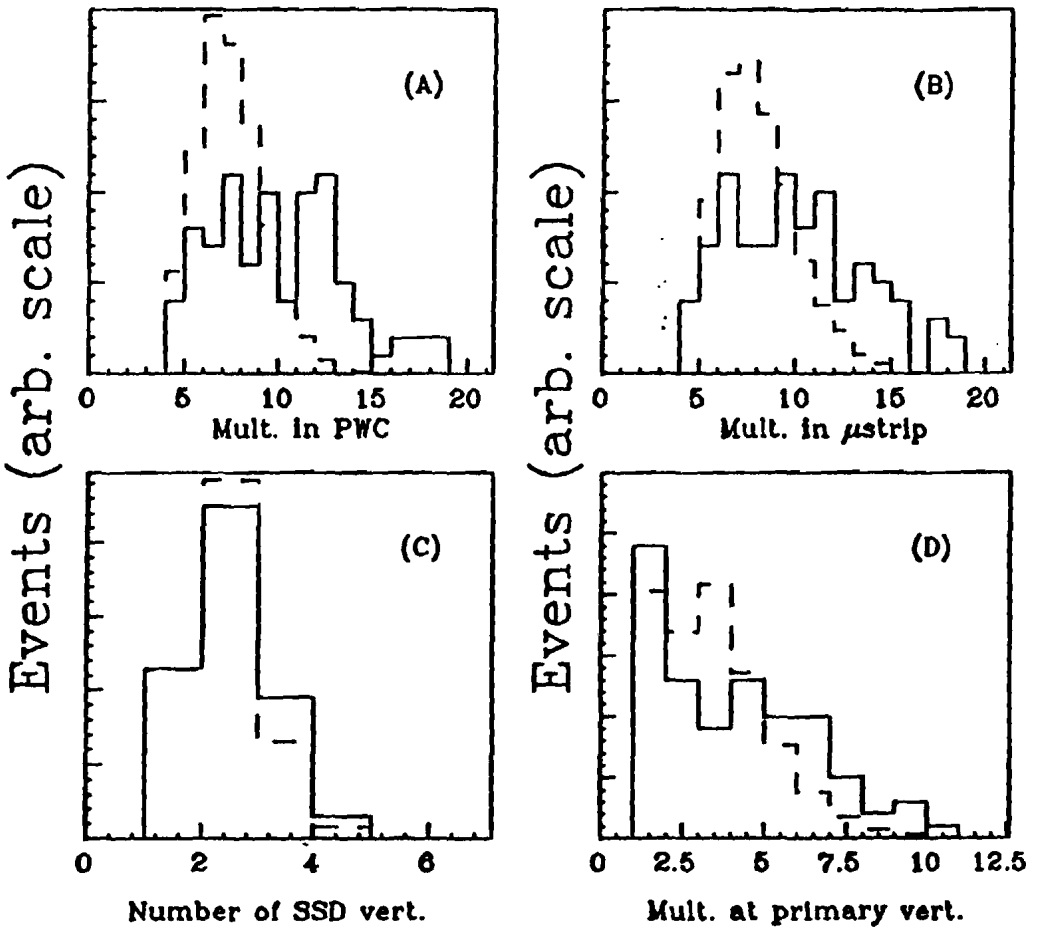

Figure 4.20: Comparisons between Data and Monte Carlo Event Samples: (A) Charged track multiplicity in the PWC's; (B) Charged track multiplicities in the microstrip; (C) Number of SSD vertices; (D) Multiplity at the primary vertex. The data is the solid, while MC is dashed.

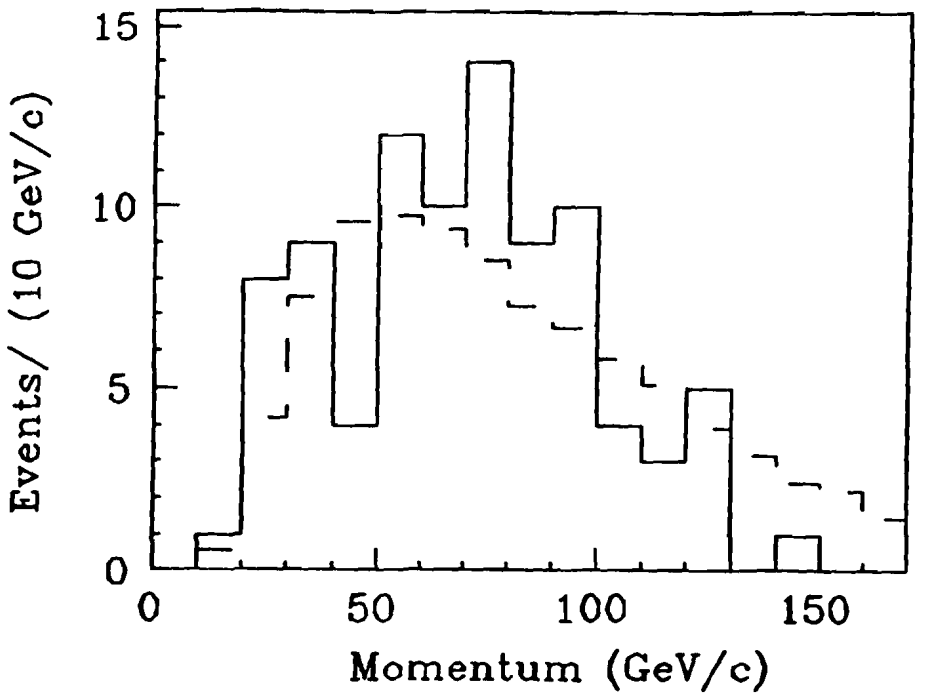

Figure 4.21: Momentum Distribution of D_s^+ Comparing Data to Monte Carlo. The solid line is data; the dashed line is Monte Carlo.

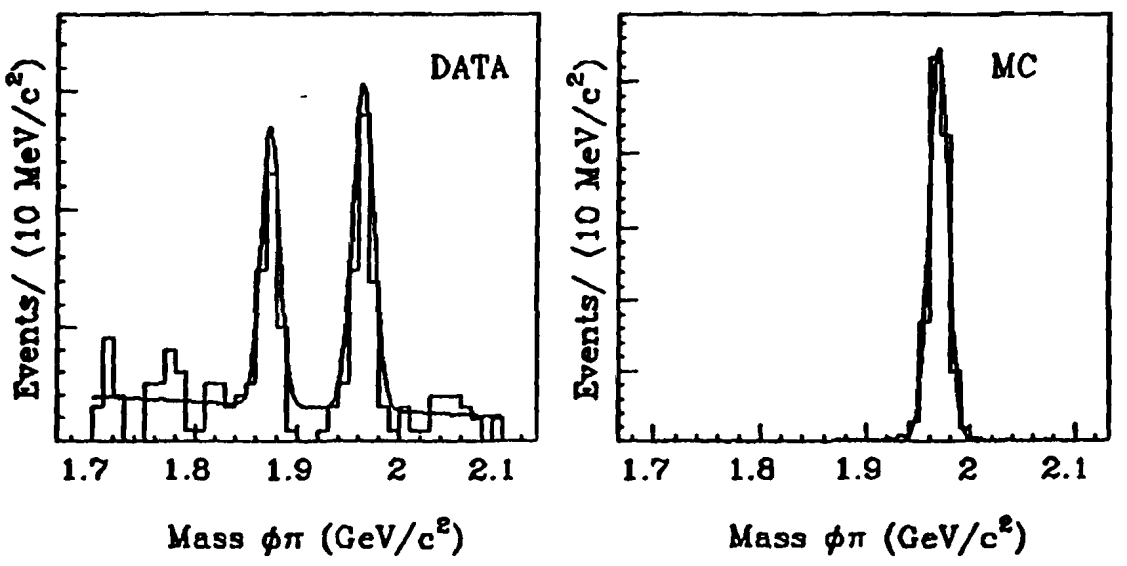

Figure 4.22: Comparisons in D_s^+ Mass Resolution in Data and MC.

Table 4.8: MASS FIT COMPARISON (DATA VS. MC)

	DATA	MONTE CARLO
D_s^+ MASS (MeV/c^2)	1967 ± 2	1968 ± 1
$\sigma(D_s^+)$ (MeV/c^2)	10.2 ± 0.2	9.5 ± 0.1

5. DVERT succeeded in determining primary and secondary vertices;

6. The primary vertex was located within the target;

7. The value of the χ^2/DOF for the secondary vertex was less than 3;

8. The value $|\cos\theta|$ was greater than 0.3;

9. The secondary vertex was downstream of the primary vertex;

10. Various L/σ_L cuts were satisfied.

These cuts were performed on 200,000 events generated by the ROGUE Monte Carlo program. The efficiency after each successive cut, as well as relative percentages are displayed in Table 4.9. From these studies, the overall efficiency for finding the D_s^+ meson via the $\phi^0\pi^+$ decay mode in the E687 data with all of the cuts and with $L/\sigma_L > 3$, is roughly 14%. The efficiency of the DVERT algorithm for this decay state was approximately 90%, while the target cuts excluded very few events in the Monte Carlo. It should be noted that the efficiency for kaon identification derived from MC simulation was approximately 10% higher than the efficiency derived from kaon identification studies using reconstructed ϕ^0's ($\rightarrow K^+K^-$) in the data sample. This could lower the overall efficiency somewhat.

Table 4.9: EFFICIENCY STUDY

CUT	% OF TOTAL	RELATIVE EFFICIENCY
Master gate	89.2	89.2
Master gate and 2nd level trigger	46.5	52.1
Čerenkov identification	34.3	73.8
ϕ^0 cut	31.4	91.4
DVERT succeeds	27.9	90.0
Target cut	27.3	98.0
$\chi^2/DOF(secondary) < 3$	25.4	93.0
$\lvert\cos(\theta)\rvert > 0.3$	25.2	97.0
$L/\sigma_L > 0.$	20.2	79.4
$L/\sigma_L > 1.$	17.8	88.8
$L/\sigma_L > 2.$	15.5	87.4
$L/\sigma_L > 3.$	13.6	87.4
$L/\sigma_L > 4.$	11.9	88.0
$L/\sigma_L > 5.$	10.5	88.0
$L/\sigma_L > 6.$	9.3	88.1
$L/\sigma_L > 7.$	8.2	88.1
$L/\sigma_L > 8.$	7.2	88.5
$L/\sigma_L > 9.$	6.4	88.6

CHAPTER 5

LIFETIME ANALYSIS

In this chapter is presented a measurement of the lifetime of the D_s^+ meson (via the $\phi^0\pi^+$ mode), as well as the lifetime of the D^+ meson (via the Cabibbo-suppressed mode, $\phi^0\pi^+$). The lifetime measurement technique is first studied and formulated. The results of the measurement are then examined.

5.1 Lifetime Measurement Technique

In the previous chapter, the D_s^+ and D^+ signals were obtained from the data. The effective mass distribution that resulted when all of the analysis cuts were applied was shown in Fig. 4.10, while the associated proper time distribution for these events was displayed in Fig. 4.11. The technique implemented to obtain the lifetimes of the D_s^+ and D^+ mesons was to use a maximum likelihood fit utilizing the effective mass (m_i) and proper time (t_i) values of each event [28].

5.1.1 Maximum Likelihood Method

The maximum likelihood method is a powerful technique for determining unknown parameters from a small number of events [29]. Consider $Y_i(c^*, \theta_i)$ as the probability of obtaining a value of the parameter c^* given a data point θ_i. If each event is obtained in an independent fashion, then the joint probability, $\mathcal{F}$, for obtaining a

value c^* from N data points, $(\theta_1, \theta_2, \ldots, \theta_N)$ is

$$\mathcal{F} = \prod_{i=1}^{N} Y_i(c^*, \theta_i). \tag{5.1}$$

For mathematical facility, the multiplication is changed to a summation giving,

$$\mathcal{L} = \log \mathcal{F} = \sum_{i=1}^{N} \log Y_i(c^*, \theta_i). \tag{5.2}$$

This is useful since the minimum or maximum of a function is the same value as the minimum or maximum of the logarithm of that function.

We want to maximize the function $\mathcal{L}$, but can also equivalently minimize the negative of this function. So the following is chosen to be minimized,

$$\mathcal{L} = -\log \mathcal{F} = -\sum_{i=1}^{N} \log Y_i(c^*, \theta_i). \tag{5.3}$$

To switch from the abstract to a concrete example, we consider the D_s^+ meson lifetime. For a large set of proper time measurements of the lifetime of the D_s^+ meson, $(t_1, t_2, \ldots, t_N)$, the probability of observing a proper time t_i given the lifetime τ is,

$$f_i = \frac{1}{\tau} \exp \frac{-t_i}{\tau}. \tag{5.4}$$

We can then use the maximum likelihood technique to determine the most probable value of the lifetime. Using the maximum likelihood formalism, a function $\mathcal{F}$ will be minimized where $f_i = Y_i$, $\tau = c^*$ and $t_i = \theta_i$. Therefore,

$$\mathcal{F} = \prod_{i=1}^{N} \frac{1}{\tau} \exp \frac{-t_i}{\tau} \tag{5.5}$$

and,

$$\log \mathcal{F} = \sum_{i=1}^{N} \log \frac{1}{\tau} - \sum_{i=1}^{N} \frac{t_i}{\tau} \tag{5.6}$$

with,

$$\mathcal{L} = -\log \mathcal{F} = -\sum_{i=1}^{N} \log \frac{1}{\tau} + \sum_{i=1}^{N} \frac{t_i}{\tau} \tag{5.7}$$

Now $\mathcal{L}$ is minimized with respect to τ:

$$\frac{\partial \mathcal{L}}{\partial \tau} = 0 \tag{5.8}$$

or,

$$\frac{\partial \mathcal{L}}{\partial \tau} = \frac{N}{\tau} - \frac{\sum t_i}{\tau^2} = 0. \tag{5.9}$$

Solving for τ gives,

$$\tau = \frac{\sum t_i}{N}. \tag{5.10}$$

The most likely value of the lifetime is the *average* value of the proper times. This result was tested on 100,000 ROGUE Monte Carlo events. Given an input D_s^+ lifetime of 0.436 picoseconds, the average proper time was 0.436 picoseconds. If the analysis cuts were applied to this MC data set including the $L/\sigma_L > 3$ cut, the average proper time was 0.68 picoseconds.

This disparity is a clear indication that a simple average of the proper time distribution for the $\phi^0\pi^+$ events with $L/\sigma_L > 3$ will not a produce an accurate D_s^+ lifetime. Furthermore considering that:

- The geometrical acceptance of the spectrometer has excluded D_s^+ particles with low momentum values;
- The $L/\sigma_L > 3$ cut has removed the short lived D_s^+ ;
- The short lived D_s^+ particles may have had their daughter particles absorbed in the target;
- The microstrip detector may not be able to reconstruct vertices in certain Z-coordinate positions;
- The events in the D_s^+ mass range contained only 104 or so events as well as another 40 background events,

one cannot consider the data set a large sample of unbiased proper time measurements; therefore, the likelihood function $\mathcal{F}$ must be modified.

5.1.2 Construction of the Likelihood Function

Examining Fig. 4.10 once again, it is clear that the $\phi^0\pi^+$ ($L/\sigma_L > 3$) sample can be divided into three classifications:

1. D_s^+ events (Ds); events in the mass range 1.94 GeV/c^2 to 1.99 GeV/c^2 .
2. D^+ events (D); events in the mass range 1.85 GeV/c^2 to 1.90 GeV/c^2 .
3. Background events (BG); events in the mass ranges of 1.7 GeV/c^2 to 2.1 GeV/c^2 , including some fraction of the D_s^+ and D^+ events.

The likelihood function then contains three terms: one associated with the D_s^+ events, one associated with the D^+ events and another associated with the background events:

$$\mathcal{F}(m_i,t_i) = \mathcal{F}(m_i,t_i)_{D_s} + \mathcal{F}(m_i,t_i)_D + \mathcal{F}(m_i,t_i)_{BG} \tag{5.11}$$

with,

$$\mathcal{F}(m_i,t_i)_{D_s} = \frac{N_{D_s}}{\sigma_{D_s}\sqrt{2\pi}} \exp\left(\frac{-(m_i-\mu_{D_s})^2}{\sigma_{D_s}^2}\right)\frac{1}{\tau_{D_s}} \exp\left(\frac{-t_i}{\tau_{D_s}}\right) \tag{5.12}$$

and,

$$\mathcal{F}(m_i,t_i)_D = \frac{N_D}{\sigma_D\sqrt{2\pi}} \exp\left(\frac{-(m_i-\mu_D)^2}{\sigma_D^2}\right)\frac{1}{\tau_D} \exp\left(\frac{-t_i}{\tau_D}\right) \tag{5.13}$$

and finally,

$$\mathcal{F}(m_i,t_i)_{BG} = A(1+B\cdot m_i)\left(\exp\frac{-t_i}{\tau_1} + C\exp\frac{-t_i}{\tau_2}\right). \tag{5.14}$$

For both the D_s^+ and D^+ terms, there is a Gaussian function for the mass and the decay function for the proper time. The background term has a linear polynomial

term for the mass and the sum of two exponentials for its proper time parameterization.

Background Proper Time Parameterization

A single exponential function was first studied for the background proper time parameterization since previous charmed meson lifetime measurements parameterized the background proper time with this function [30][31][32]. However, this was not adequate. A comparison is made of three parameterizations of the background proper time in Fig. 5.1. These parameterizations included: the sum of two exponentials, one exponential and an exponential with a power. The background events were $\phi^0\pi^+$ events ($L/\sigma_L > 3$) in the mass range, 1.7 GeV/c^2 to 1.85 GeV/c^2 . As clearly seen in Fig. 5.1, a double exponential rather than a single exponential or exponential with a power fits the distribution most accurately. In Fig. 5.2 is exhibited the results of a double exponential fit of the form,

$$bg(t_i) = \exp\frac{-t_i}{\tau_1} + C\exp\frac{-t_i}{\tau_2}, \tag{5.15}$$

(with $\tau_1 = 0.077$ picoseconds; $\tau_2 = 0.47$ picoseconds and C = 0.039) applied to the background proper time distribution in four background mass regions. Clearly a double exponential of this form nicely parameterizes the background proper time distribution in all mass ranges.

A double exponential function may offer some insight into the nature of the background. A value of $\tau_1 = 0.077$ picoseconds is very similar to the E687 experiment's proper time resolution of 0.07 picoseconds (for the D_s^+ , $D^+ \rightarrow \phi^0\pi^+$ events) measured and discussed in the last section of this chapter. A value of 0.47 picoseconds for the second background lifetime parameter, τ_2, may indicate that misidentified charm decays are contributing to the background. If one of the tracks identified as kaon consistent by the Čerenkov algorithm was a actually a pion, a

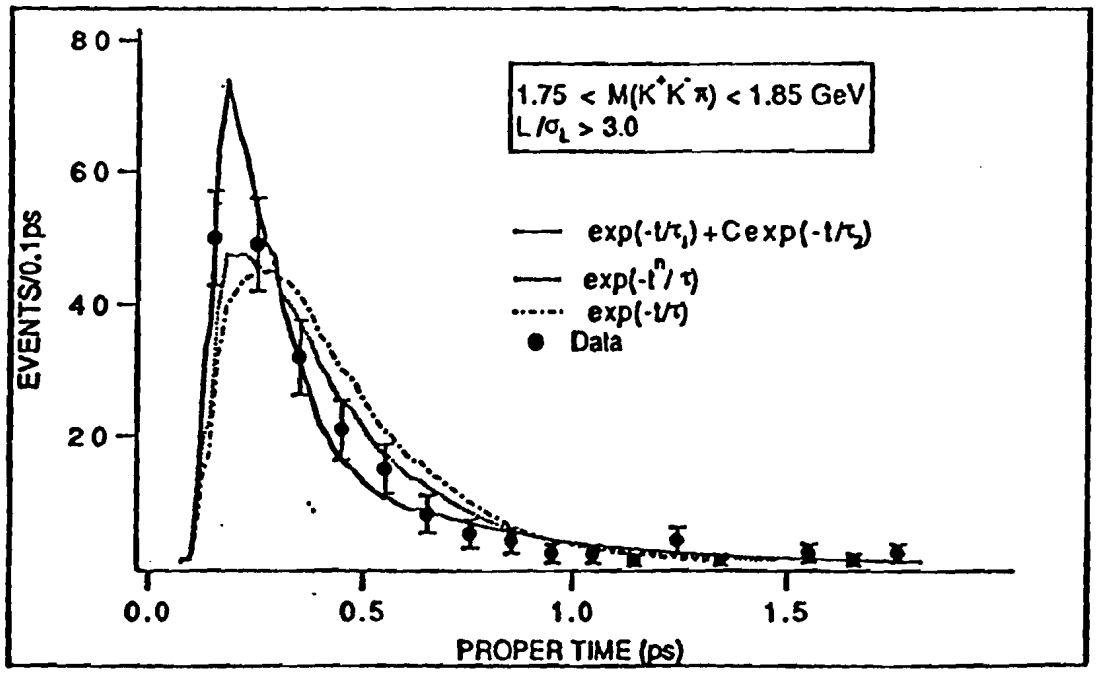

Figure 5.1: The Background Mass Region (1.75 GeV/c^2 to 1.85 GeV/c^2) Proper Times Fit to Three Different Functions.

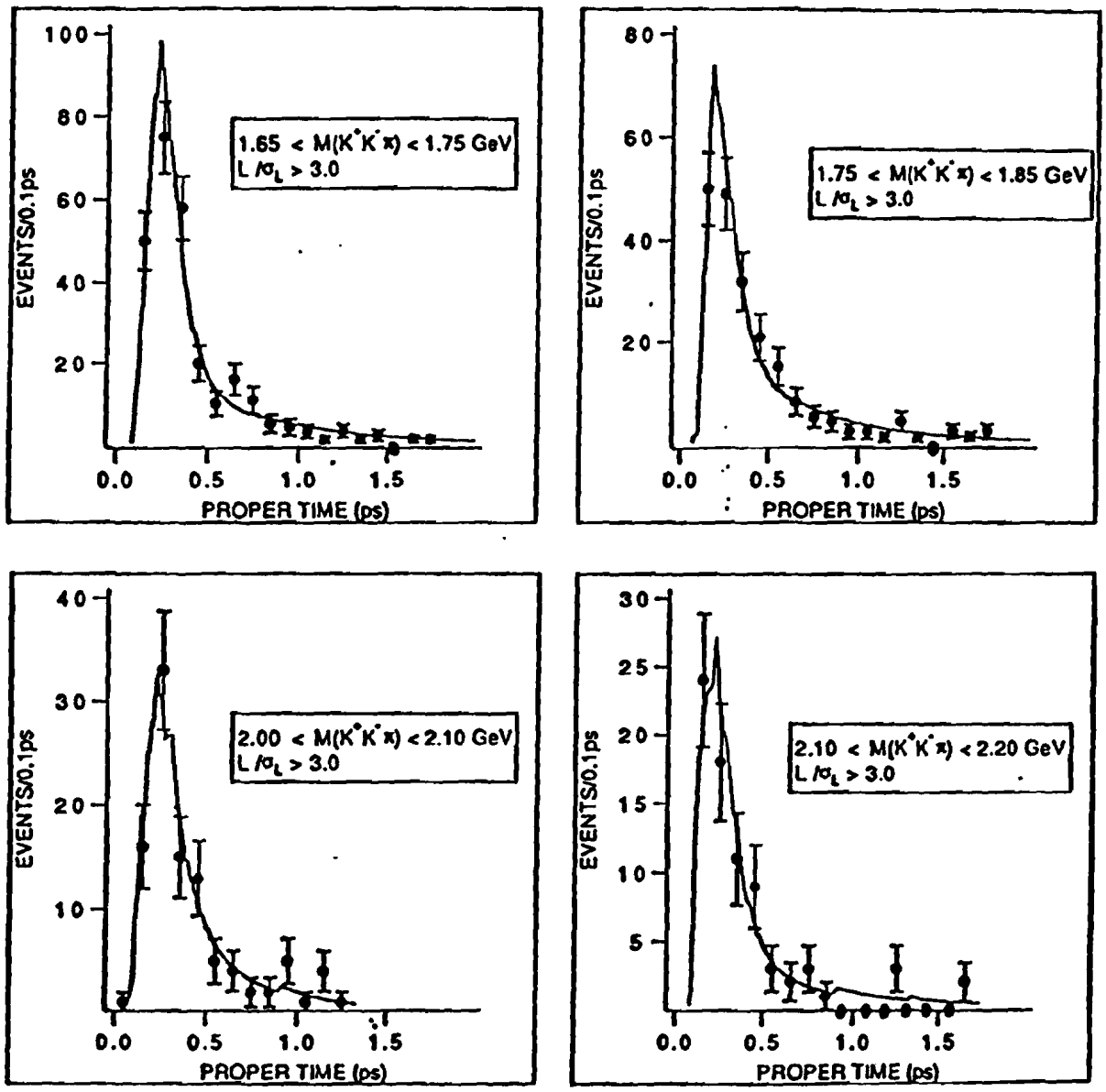

Figure 5.2: The Background Event Time Distribution for Four Mass Regions ($L/\sigma_L >$ 3) Fit to a Double Exponential.

decay such as, $D^+ \rightarrow K^-\pi^+\pi^-$ may have occurred; or one of the kaon-identified tracks could be a proton from the decay, $\Lambda_c^+ \rightarrow pK^-\pi^+$. Analysis cuts chosen to maximize the $D_s^+ \rightarrow \phi\pi^+$ signal will have certainly suppressed such events, but a small number might still remain. This may be reflected in the small value of the constant, C, which weights the "charm-like" background contribution far less than the time resolution contribution in the background proper time parameterization.

To study the background, some 200,000 Monte Carlo events were generated using ROGUE in which a ficticious particle with a mass of 1.8 GeV/c^2 and zero lifetime was generated and then required to decay into $\phi^0\pi^+$ followed by the decay of the ϕ^0 into K^+K^-. These events were then reconstructed and all cuts which were required of the data were applied. A total of 354 events survived with a $\phi^0\pi^+$ mass in the region 1.8 $\pm$ 0.01 GeV/c^2 and $L/\sigma_L > 3$. The reconstructed proper time distribution for these events is shown in Fig. 5.3 along with the proper time distribution for the background events from the data in the 1.8 GeV/c^2 region. Normalized to the same area, the two samples are very similar. Thus one does not need misidentified charm to account for the background.

Because of the similarity of the Monte Carlo distribution and the data, it was not surprising that the Monte Carlo event distribution could not be fit with either a single exponential or a Gaussian centered at zero proper time as shown in Fig. 5.4. However the distribution could be fit with a double exponential as shown in Fig. 5.5.

Normalization

The function $\mathcal{F}(m_i, t_i)$ was normalized over mass and proper time as required by the maximum likelihood technique. This was essential so that the function $\mathcal{F}(m_i, t_i)$ behaves as a probability distribution. The function $\mathcal{L}(m_i, t_i)$ to be minimized was

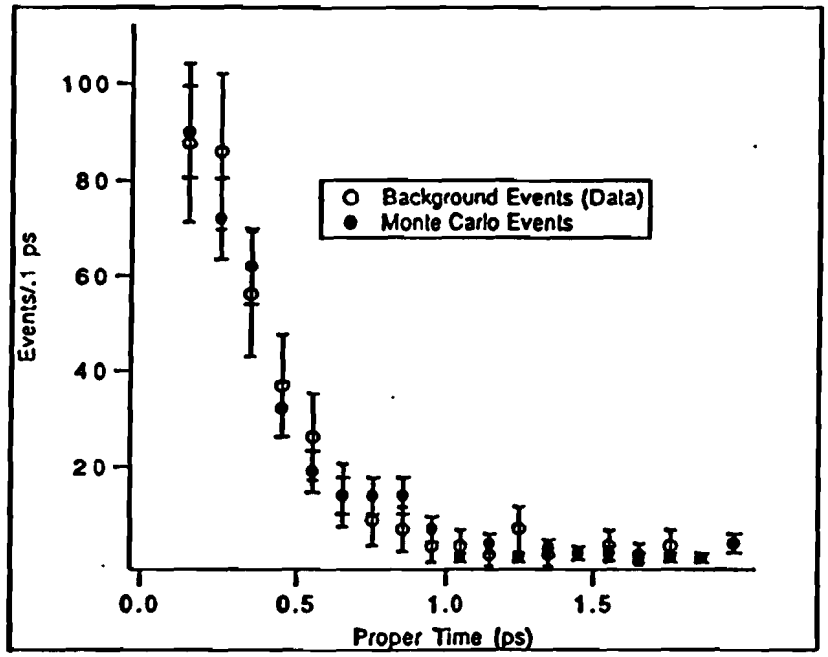

Figure 5.3: Proper Time Distribution of Monte Carlo Events and of Background Events from the Data.

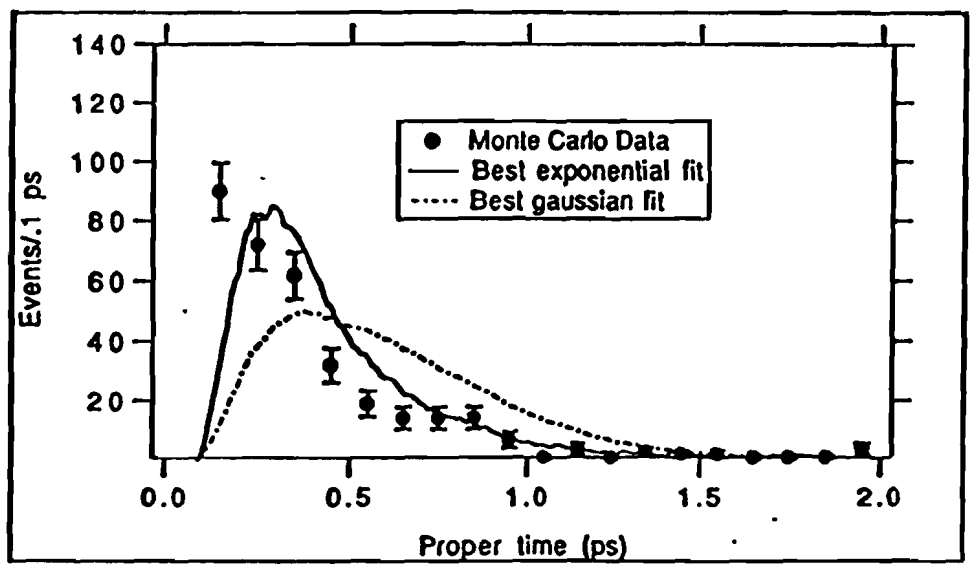

Figure 5.4: Monte Carlo Data with Maximum Likelihood Fits Using an Exponential Distribution and a Gaussian Distribution.

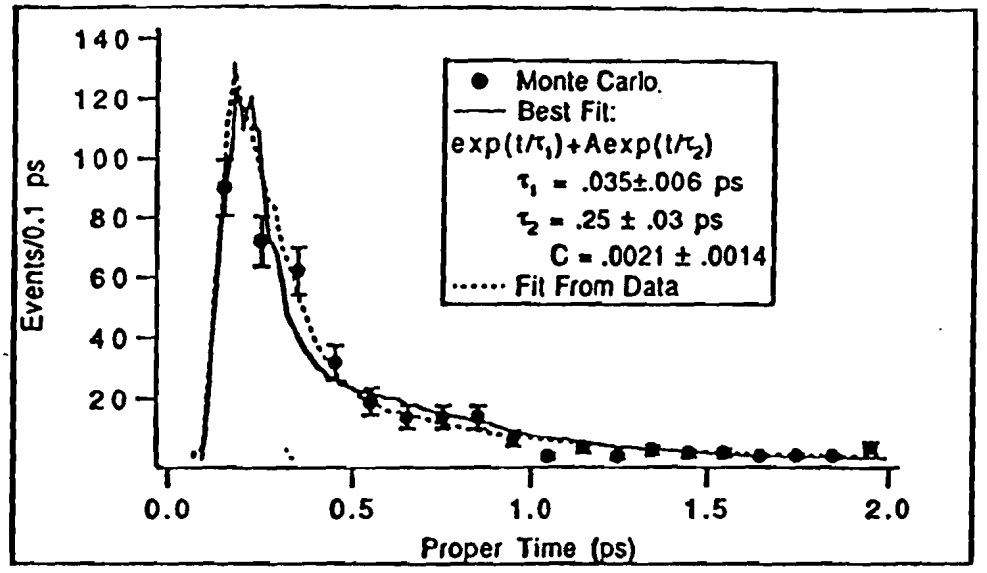

Figure 5.5: Monte Carlo Events with the Maximum Likelihood Fit Using a Sum of Two Exponentials. (Also shown is the best two-exponential fit to the background data in the 1.8 GeV/c^2 region).

then,

$$\mathcal{L}(m_i, t_i) = -\sum_{i=1}^{N} \log\left(\frac{\mathcal{F}(m_i, t_i)}{\int\int \mathcal{F}(m_i, t_i) dm dt}\right). \tag{5.16}$$

The limits of integration over mass were simply the mass limits chosen in the invariant mass plot. A range of 1.7 GeV/c^2 to 2.1 GeV/c^2 was chosen as shown in Fig. 4.10. This choice was made simply to accommodate the D^+ and D_s^+ signal regions and also allow some background bands on the both sides of the signal regions. The final section of this chapter discusses how the choice of these limits affected the D_s^+ and D^+ lifetime measurements.

Unlike the limits of the mass integral, the limits of integration on the proper time varied on an event-by-event basis. Given the proper time as,

$$t = \frac{Lm}{p}, \tag{5.17}$$

the error in this quantity would be approximated by,

$$\frac{\sigma_t}{t} = \sqrt{\left(\frac{\sigma_L}{L}\right)^2 + \left(\frac{\sigma_p}{p}\right)^2}. \tag{5.18}$$

Since the average momentum of the D_s^+ and D^+ was over 60 GeV/c and the error in this momentum was of the order 0.1 GeV/c , the quantity $(\sigma_p/p)^2$ is negligible in comparison to $(\sigma_L/L)^2$. This gives,

$$\frac{\sigma_t}{t} = \frac{\sigma_L}{L}, \tag{5.19}$$

or,

$$\sigma_t = t\left(\frac{\sigma_L}{L}\right). \tag{5.20}$$

With the analysis cut $L/\sigma_L > 3$ being equivalent to requiring that $t_i > 3\sigma_t$, the minimum limit of integration, $\tau_{\min}$, becomes equal to $3\sigma_t$. The variable σ_t varied event by event since both t_i and σ_L/L vary. The choice of $\tau_{\min}$ and how it influenced the D_s^+ and D^+ lifetimes is also discussed in the last section of this chapter.

Just as the lower limit of integration for the proper time varied on an event-by-event basis, so did the upper time limit. The upstream face of TR1 set the upper limit in decay length or proper time ($\tau_{\max}$). This is because decays downstream of TR1 would not satisfy the master gate (Chapter 3) and therefore would not be recorded on tape. (Any decays occurring within TR1 most likely resulted from charged particles interacting with the hadronic matter of the trigger counter and were also excluded as discussed in the previous chapter.) The value of $\tau_{\max}$ varied since the momentum of each particle was needed to determine this quantity. This assignment of the $\tau_{\max}$ variable excluded few events. In a study of 50,000 ROGUE Monte Carlo events, only a small number decayed beyond the nominal Z-coordinate position of TR1. Once again, the effect of the $\tau_{\max}$ variable will be discussed in the section on errors in this chapter.

With the assignment of $\tau_{\min}$ and $\tau_{\max}$ integration limits on the proper time, the likelihood function has been modified to take into account the short lived D_s^+ and D^+ events removed by the L/σ_L cut and the long lived D_s^+ and D^+ events that cannot be reconstructed downstream of the trigger counter TR1. But the influence of the geometrical acceptance of the spectrometer and various analysis cuts on the D_s^+ and D^+ lifetime measurements must also be incorporated into the likelihood function. Similarily the absorption of secondaries from short lived D_s^+ and D^+ must be considered. Both of these corrections are incorporated into the likelihood function by the addition of an acceptance function, $f(t_i)$.

Proper Time Acceptance Function

This acceptance function, $f(t_i)$, was calculated in the following manner. A large sample of Monte Carlo events was analyzed with all cuts, except the L/σ_L cut, and then studied to determine how the input proper time distribution varied as a function of these cuts. After all cuts were applied, the resulting input input proper time distribution was divided by the original distribution to determine $f(t_i)$. The original input Monte Carlo proper time distribution fit to an exponential is shown in Fig. 5.6. The input proper time fit gave a D_s^+ lifetime value of 0.436 picoseconds, a value equal to the standard value.

The absorption of kaons and pions from D_s^+ and D^+ decays will be most severe for short lived D_s^+ and D^+ since the decay particles must traverse more of the target material as shown in Fig. 5.7. The number of D_s^+ and D^+ mesons absorbed by the target material would be negligible due to their short path length. Only absorption of the daughter kaons and pions was considered.

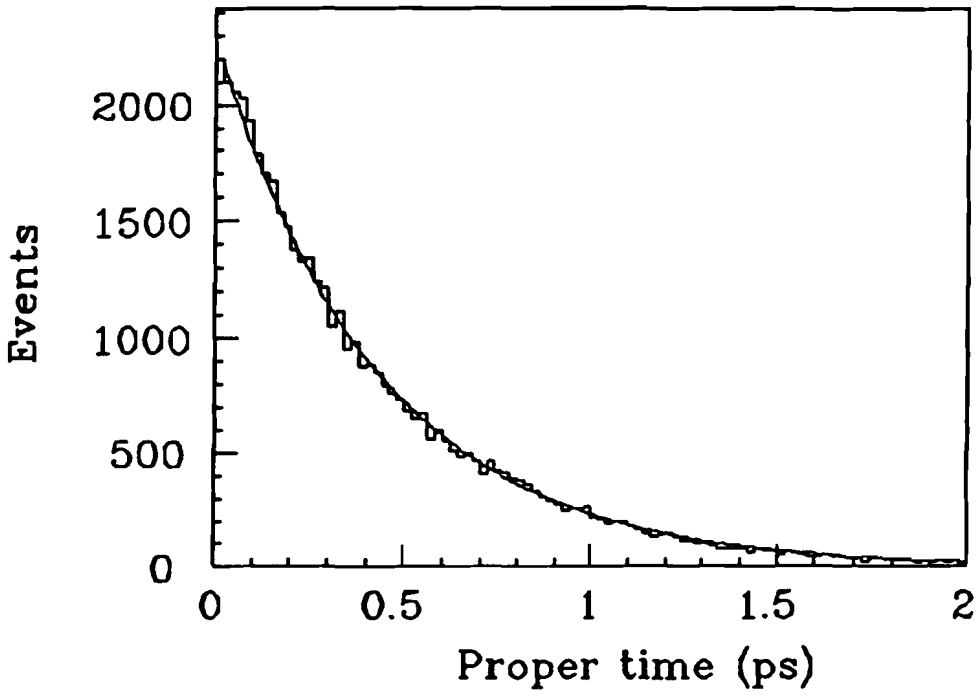

Figure 5.6: Input Monte Carlo Proper Time Distribution.

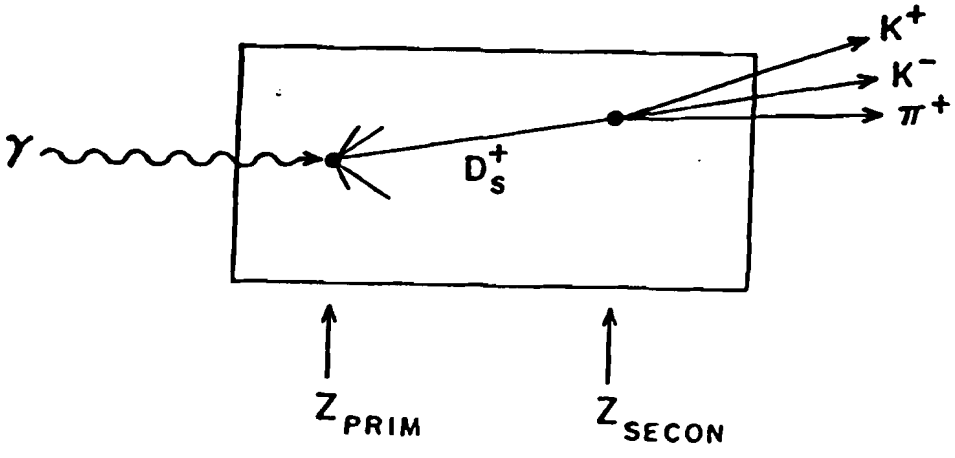

Figure 5.7: Decays in the Target Region.

The probability that a daughter $K^{\pm}$ or $\pi^{\pm}$ of a D_s^+ or D^+ survives in the target is reduced by the factor,

$$\exp -(\alpha_{abs}\Delta L), \tag{5.21}$$

where ΔL is the distance the particle travelled in the target and α_{abs} is an absorption coefficient depending on two factors:

1. The density of atoms in the target (ρ);

2. The absorption cross section for that particle (σ_{abs})

where,

$$\alpha_{abs} = \rho\sigma_{abs}. \tag{5.22}$$

The absorption cross section, σ_{abs}, is a function of momentum, particle type and target material [33], while ρ depends on the target material. As mentioned in chapter 2, the data were obtained with both beryllium and silicon targets; therefore, separate efficiency functions, $f(t_i)$'s, were used. And as also discussed in chapter 2, there were actually three targets: one with four stacks of beryllium (4BE), another with five stacks of beryllium (5BE) and a silicon target (SILI). It is interesting to note that α_{abs} is nearly equal for beryllium and silicon. Although the absorption cross sections for K's and π's in silicon are nearly 2.5 times greater than those in beryllium, the density of atoms in silicon compared to beryllium is 2.5 times reduced. The beryllium targets tended to have a greater absorption probability since the average ΔL's were larger than in the silicon target. This is because the beryllium targets were somewhat longer than the silicon target as displayed in Fig. 2.9.

The quantity ΔL will be approximated as ΔZ because the opening angles of the tracks are so small. This is shown in Fig. 5.8 which plots a comparison of the

X-coordinate and Y-coordinates positions of tracks at the secondary vertex to the X- and Y-coordinates of the same tracks as they exited the target. This was done for each of the three targets. Few were outside the target region as seen in this figure.

The absorption contribution to the acceptance function was calculated by retaining only those D_s^+ events where none of the daughter particles were absorbed in the target. As mentioned above, the absorption affected the shorter lived D_s^+ most greatly. However, it is not a severe effect as shown in Fig. 5.9 and Fig. 5.10 which plot the probability of survival as a function of the proper time in the 5BE and SILI targets. A comparison of these plots shows that absorption was noticeably more severe in beryllium target where decay paths were longer than in the silicon target[1].

The proper time acceptance function also had to incorporate the efficiencies of each of the analysis cuts discussed in chapter 4. Some cuts may affect the proper time measurement by excluding particles with certain proper time values. The analysis cuts that may affect the proper time measurement are:

- The gating requirements (both master gate and second level trigger) had to be satisfied for the event [MG+2nd];
- The possibility that secondary π's and K's (from D_s^+ and D^+ decays) were absorbed in the target was examined [ABSORB];
- Čerenkov requirements were imposed on the π's and K's [CER];
- The ϕ^0 mass cut (1.01 GeV/c^2 < M_{KK} < 1.03 GeV/c^2 and both kaons required to link) was imposed [PHI];

[1] Once again, this is due to the increased length of the beryllium targets compared to the silicon.

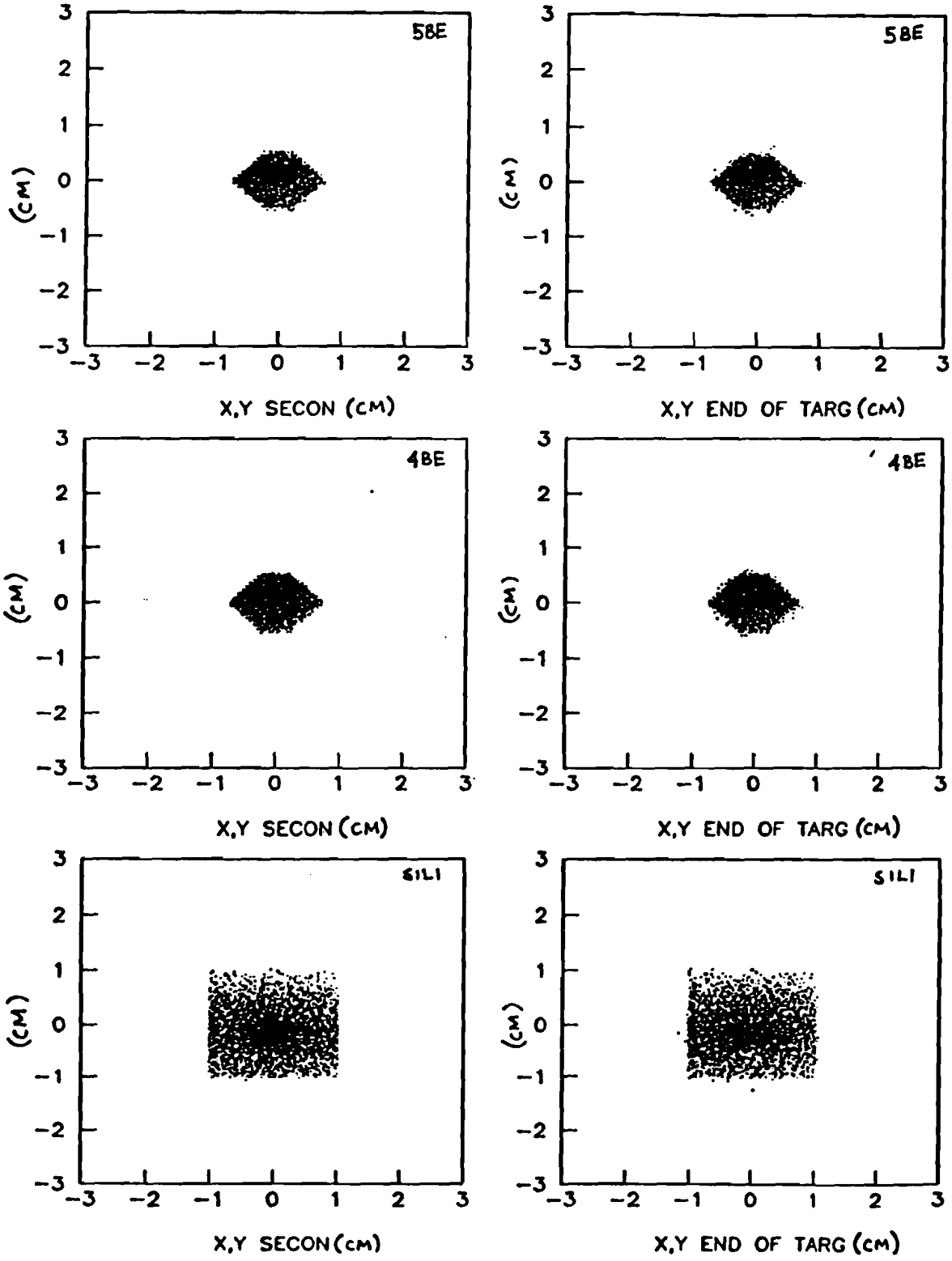

Figure 5.8: The X-, Y- coordinate Positions of Tracks at the Secondary Vertex and at the Exit of the Target for each Target.

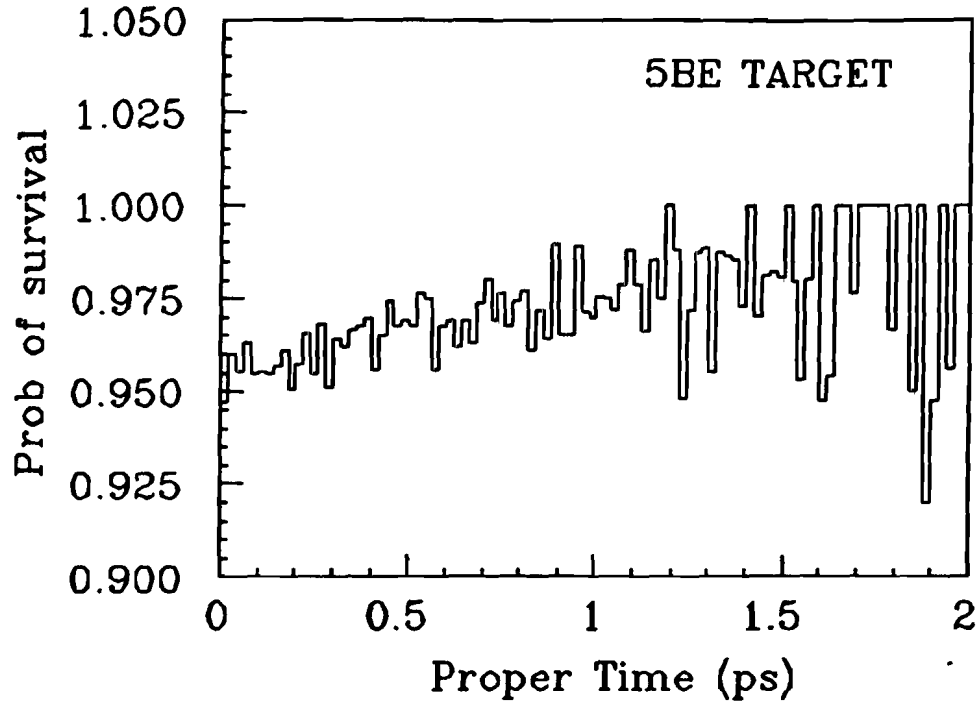

Figure 5.9: The Probability of Survival (No Absorption) as a Function of Proper Time in the 5BE Target.

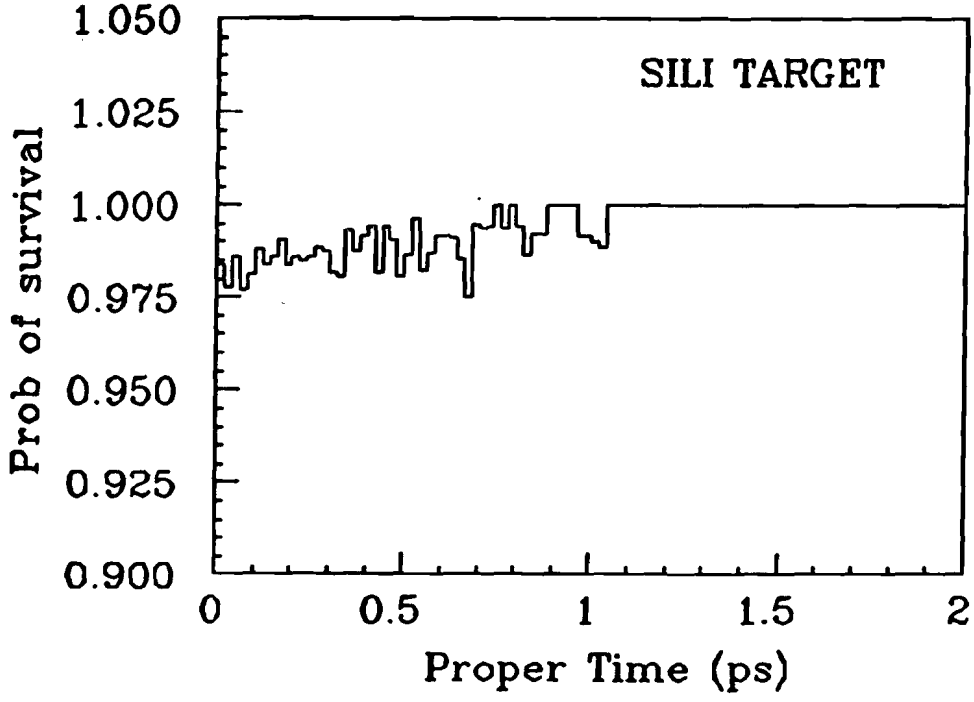

Figure 5.10: The Probability of Survival (No Absorption) as a Function of Proper Time in the SILI Target.

- DVERT was required to determine a primary and secondary vertex for the event [DVERT];
- The primary vertex was required to be located in the target and no secondary vertices were in or downstream of TR1 [TARG];
- χ^2/DOF requirements were imposed on the secondary vertex (χ^2/DOF < 3) [CHI];
- The value of $\cos\theta$, where θ was the angle between one of the kaons and the pion in the rest frame of the ϕ^0, was required to be greater than 0.3 [COS].

The relative efficiencies as a function of proper time for a 5BE target sample of MC events are exhibited in Fig. 5.11 and Fig. 5.12. In each figure is displayed how each analysis cut (not necessarily uncorrelated) tends to affect the proper time distribution and reconfirm the efficiency studies of the previous chapter. (This was done for all three target configurations but only the 5BE plots are presented.)

The overall acceptance function, $f(t_i)$, for each of the three target configurations is displayed in Fig 5.13. Showing a slight increase in acceptance at higher proper times, the efficiency functions were fit with second order polynomials of the form:

$$\mathrm{P0}(1 + \mathrm{P1} \cdot t_i + \mathrm{P2} \cdot t_i^2) \tag{5.23}$$

In Table 5.1 are displayed the fit parameters as well as the errors in these parameters.

The function $\mathcal{F}(m_i, t_i)$ was modified now that an acceptance function had been determined. Both the D_s^+ and D^+ terms of the likelihood function are modified with the addition of the efficiency function. Since we are not concerned about the lifetime of the background, this modification is ignored for the background events.

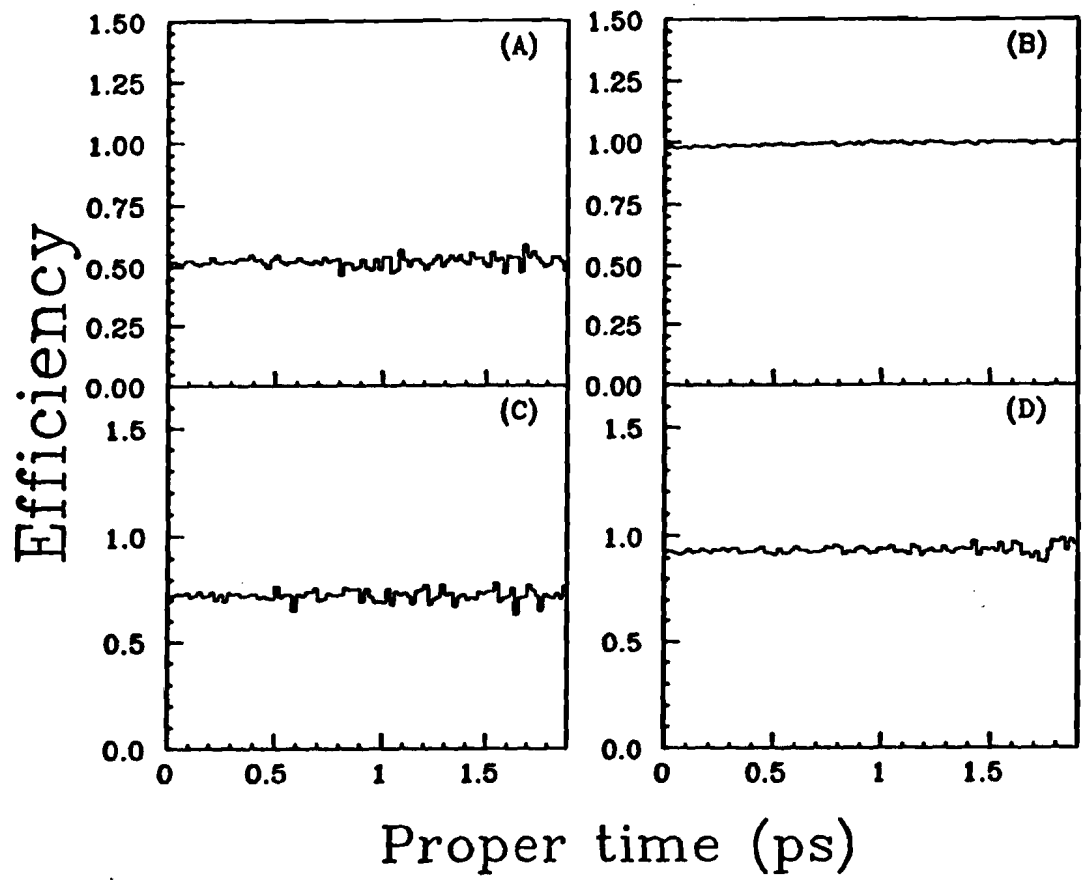

Figure 5.11: Efficiency Study (Part I): (A) MG+2nd/MG; (B) ABSORB/MG+2nd; (C) CER/ABSORB; (D) PHI/CER, as a Function of Proper Time.

Table 5.1: ACCEPTANCE POLYNOMIAL COEFFICIENTS

COEFFICIENT	5BE TARGET	4BE TARGET	SILI TARGET
P0	0.1603 ± .0019	0.1677 ± .0021	0.1642 ± .0019
P1	-0.0264 ± .0156	-0.0750 ± .0398	0.0118 ± .0376
P2	0.0777 ± .0243	0.0956 ± 0.0230	0.0434 ± .0220

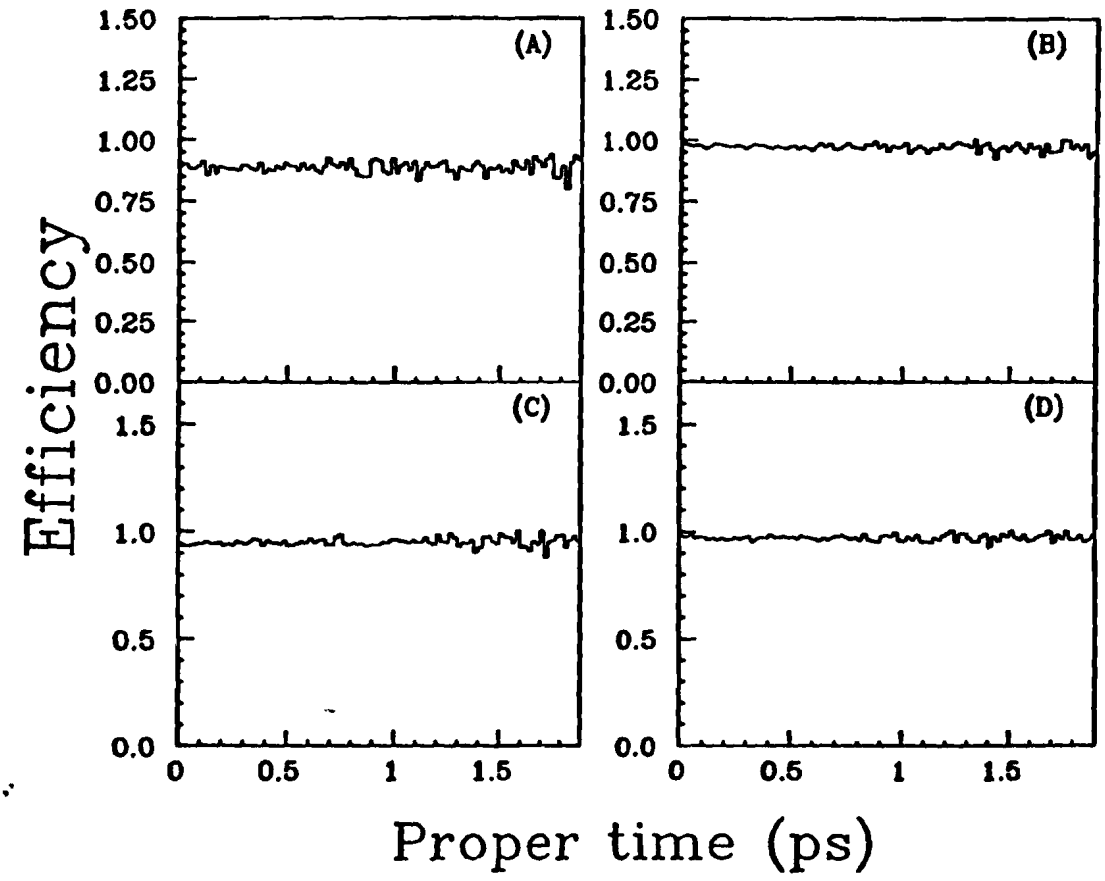

Figure 5.12: Efficiency Study (Part II): (A) DVERT/PHI; (B) TARG/DVERT; (C) CHI/TARG; (D) COS/CHI, as a Function of Proper Time.

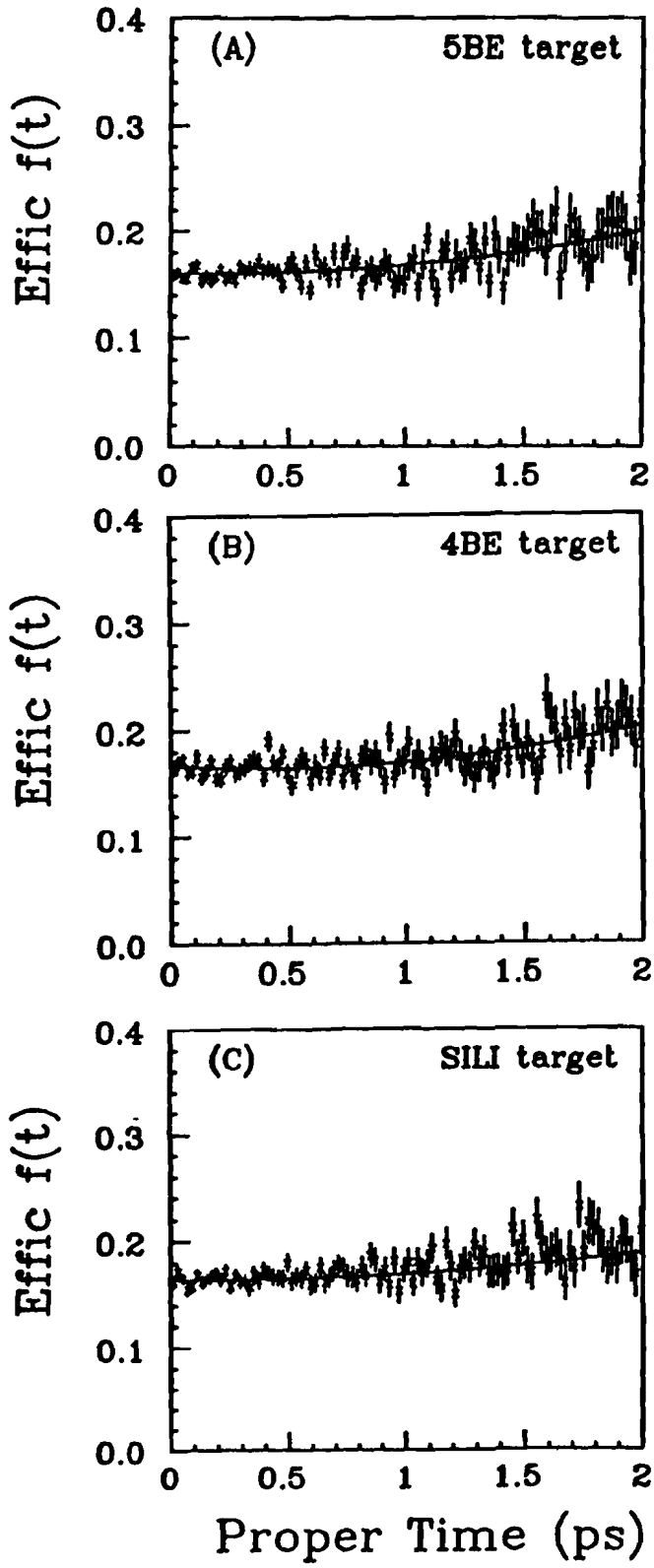

Figure 5.13: Proper Time Acceptance Functions for all 3 Target Configurations.

The components of the likelihood function then became:

$$\mathcal{F}(m_i,t_i)_{D_s} = \frac{N_{D_s}}{\sigma_{D_s}\sqrt{2\pi}} \exp\left(\frac{-(m_i-\mu_{D_s})^2}{\sigma_{D_s}^2}\right)\frac{f(t_i)}{\tau_{D_s}} \exp\left(\frac{-t_i}{\tau_{D_s}}\right) \tag{5.24}$$

and

$$\mathcal{F}(m_i,t_i)_{D} = \frac{N_{D}}{\sigma_{D}\sqrt{2\pi}} \exp\left(\frac{-(m_i-\mu_{D})^2}{\sigma_{D}^2}\right)\frac{f(t_i)}{\tau_{D}} \exp\left(\frac{-t_i}{\tau_{D}}\right) \tag{5.25}$$

The background likelihood function, $\mathcal{F}(m_i,t_i)_{BG}$, remained the same.

The efficiency function $f(t_i)$ depended on two factors, the target type for the event and the value of t_i measured. No parameters of the $f(t_i)$ function were varied in the final minimization. The run number for each event was examined to assign the associated $f(t_i)$ for that target type. The addition of the acceptance function and its effect on the D_s^+ and D^+ lifetimes will be discussed in the next section of this chapter.

The Final Fit

The function $\mathcal{F}(m_i,t_i)$ (Equation 5.11) contained 13 parameters: (1) N_{D_s}, the relative number of D_s^+ events; (2) μ_{D_s}, the mean mass of the D_s^+ ; (3) σ_{D_s}, the width of the D_s^+ signal; (4) A, a background mass coefficient; (5) B, the second background mass coefficient; (6) C, the background lifetime coefficient; (7) N_D, the relative number of D^+ events; (8) μ_D, the mean mass of the D^+ ; (9) σ_D, the width of the D^+ signal; (10) τ_{D_s}, the lifetime of the D_s^+ meson; (11) τ_D, the lifetime of the D^+ meson; (12) τ_1, a background lifetime and (13) τ_2, a second background lifetime. Minimizing $\mathcal{L}(m_i,t_i)$ with respect to these thirteen parameters would be a formidible task, but was simplified by using the CERN minimizing routine, MINUIT [34].

MINUIT can find the minimum of a multi-parameter function and analyze the behavior of that function around the minimum [34]. The routine begins by minimizing the function using a SIMPLEX routine [35] and then performs another

```
1.00AREA1        1.00       .01
2.00MASS1       1.966     0.001
3.00SIGMA1      0.010     0.001   0.006   0.012
4.00COEFF1       2.83      0.01
5.00COEFF2    -0.4184    0.001
6.00COEFF       0.137     0.001
7.00AREA2       0.40        .01
8.00MASS2       1.872     0.001
9.00SIGMA2      0.008     0.001
10.0TIME1       0.500     0.001
11.0TIME2       1.000     0.001
12.0TIM3A       .0777     0.001
13.0TIM3B       0.400     0.001

FIX       1.0
ERROR DEF 0.5
SIMPLEX
MIGRAD    1000.
CALL FCN  3.0
EXIT
```

Figure 5.14: MINUIT Command File

minimization called MIGRAD [36] in which proper errors are determined.

Listed in Fig. 5.14 is the command file for the MINUIT routine. It begins by listing the parameters, starting values and the step size of variation. Parameter(1), the relative number of D_s^+ events, was fixed at 1.00 to normalize the fit. Limits were placed on σ_{D_s}. The limits were necessary for the fit to converge but the final value was not pushed to the upper or lower limits. Aside from these modifications, all other parameters were allowed to vary with no limits placed on these values.

5.2 Lifetime Measurement Results

After the likelihood function had been determined and MINUIT implemented for maximization, the results of the likelihood fit were examined. Some important elements of the fit, such as the background proper time parameterization, the proper

Table 5.2: FIT PARAMETER RESULTS

PARAMETER	VALUE	ERROR (±)
N_{D_s}	1.00	*fixed*
μ_{D_s}	1.966	0.001
σ_{D_s}	0.0073	0.0011
A	2.827	0.547
B	-0.418	0.014
C	0.137	0.032
N_D	0.398	0.101
μ_D	1.872	0.001
σ_D	0.0057	0.0013
τ_{D_s}	0.496	0.059
τ_D	0.897	0.129
τ_1	0.112	0.011
τ_2	0.532	0.073

time acceptance function and the proper time variable were studied to determine their effect on the lifetime measurements. This section concludes with a comparison of the results of each fit.

5.2.1 The Standard Function

The *standard* likelihood function will refer to the likelihood function that contains both an acceptance function, $f(t_i)$, and a double exponential for the background proper time parameterization. The *standard* function was minimized with respect to all twelve parameters [2]. The function MIGRAD was required to converge giving the values and errors in those values for the twelve parameters as shown in Table 5.2. For the proper determination of the errors on the parameters, it was essential that MIGRAD converge [34]. The final value of the likelihood function was $\mathcal{L} = 4077.7$.

[2]The 13 parameters were reduced to 12 when N_{D_s} was kept constant at 1.

The results of Table 5.2 appeared reasonable; but in order to test the validity of the fit, the likelihood function was plotted and compared to the data. Since the likelihood function, $\mathcal{L}(m_i, t_i)$, was a function of two variables, one of these variables was integrated out in order to examine the other.

This was done in Fig. 5.15, where in Fig. 5.15(A) is plotted the maximized likelihood function on the invariant mass plot after the proper time was integrated out of the function. Likewise in Fig. 5.15(B) of this plot is displayed the proper time fit after mass was integrated out of the function. Figure 5.15(C) is a fit of the proper times in the D_s^+ mass region (1.94 GeV/c^2 to 1.99 GeV/c^2), while in Fig. 5.15(D) is plotted the same for the D^+ (1.85 GeV/c^2 to 1.90 GeV/c^2). (In all plots, the errors for each entry are simply tabulated as $\sqrt{\mathrm{N}}$.)

The likelihood fit for two background regions above and below the signal region, (1.70 GeV/c^2 to 1.85 GeV/c^2) and (1.99 GeV/c^2 to 2.1 GeV/c^2), is examined in Fig. 5.16. In Fig. 5.16(E) of this plot is shown the first background region's proper time fit, while in Fig. 5.16(F) is exhibited the same for the second background region.

It should be noted that the irregularities evident in some of the proper time fits are a consequence of the integration limits on the individual t_i's.

5.2.2 $f(t_i)$ Study

By removing the acceptance proper time function from the likelihood function, its effect on the lifetime results and the final fits was studied. The function, $f(t_i)$, was not removed from the likelihood function but simply set equal to unity making the likelihood function appear as in equations 5.12 to 5.14.

The fit results for ($f(t_i) = 1$) are shown in Table 5.3. The mass and signal

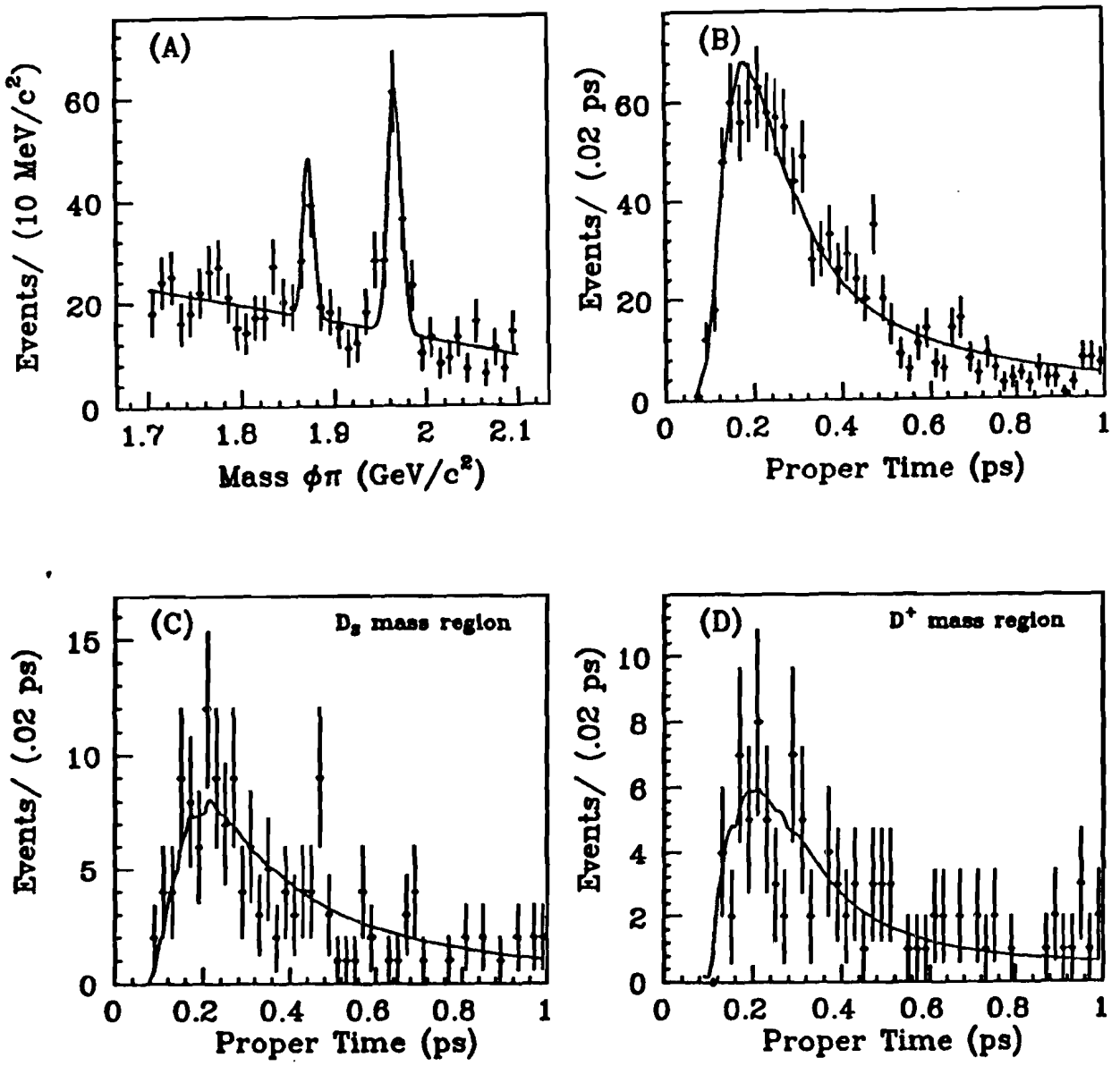

Figure 5.15: Fits to the Data ($f(t_i)$ included and double exponential background proper time parameterization.)

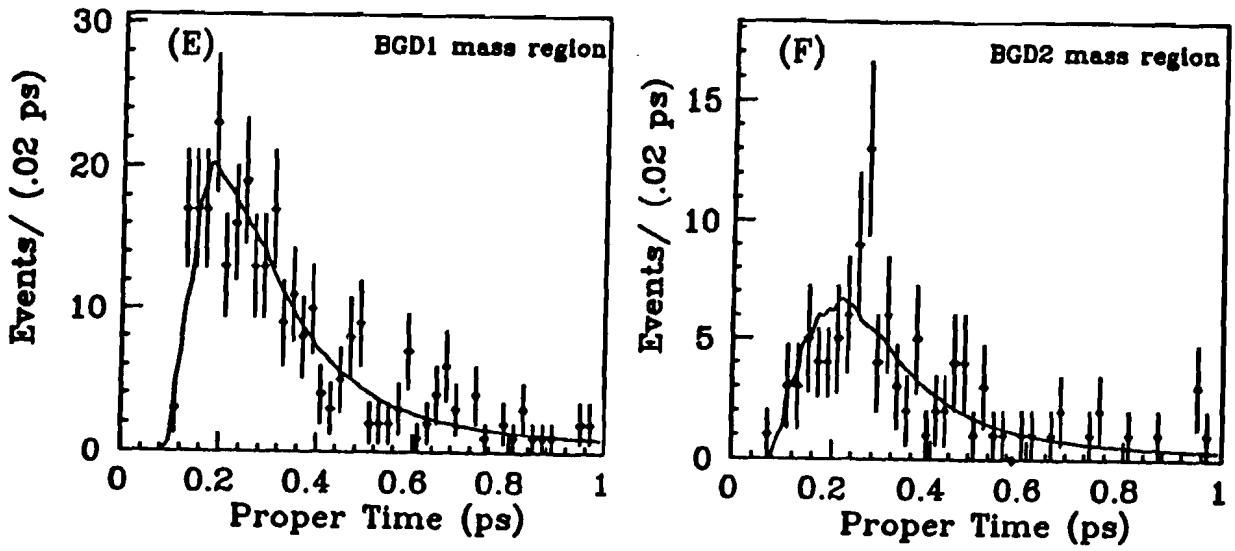

Figure 5.16: Fits to Background Proper Times ($f(t_i)$ included and double exponential background proper time parameterization.)

widths of the charmed particles were consistent with the previous fit. Most of the background constants varied slightly. The most important change was in the increase of the D_s^+ and D^+ lifetimes. Taking the proper time acceptance function into account changed the D_s^+ lifetime by -0.03 picoseconds (-5.7%) and the D^+ lifetime by -0.19 picoseconds (-17%). The final value of the likelihood function, $\mathcal{L} = 4078.1$, was slightly worse than when the correct $f(t_i)$ was included.

The fits to various parts of the data set also did not vary by large amounts from the previous fits. In a similar manner to Fig. 5.15 and Fig. 5.16, the fits to the signal and background regions are shown in Fig. 5.17 and Fig. 5.18, respectively.

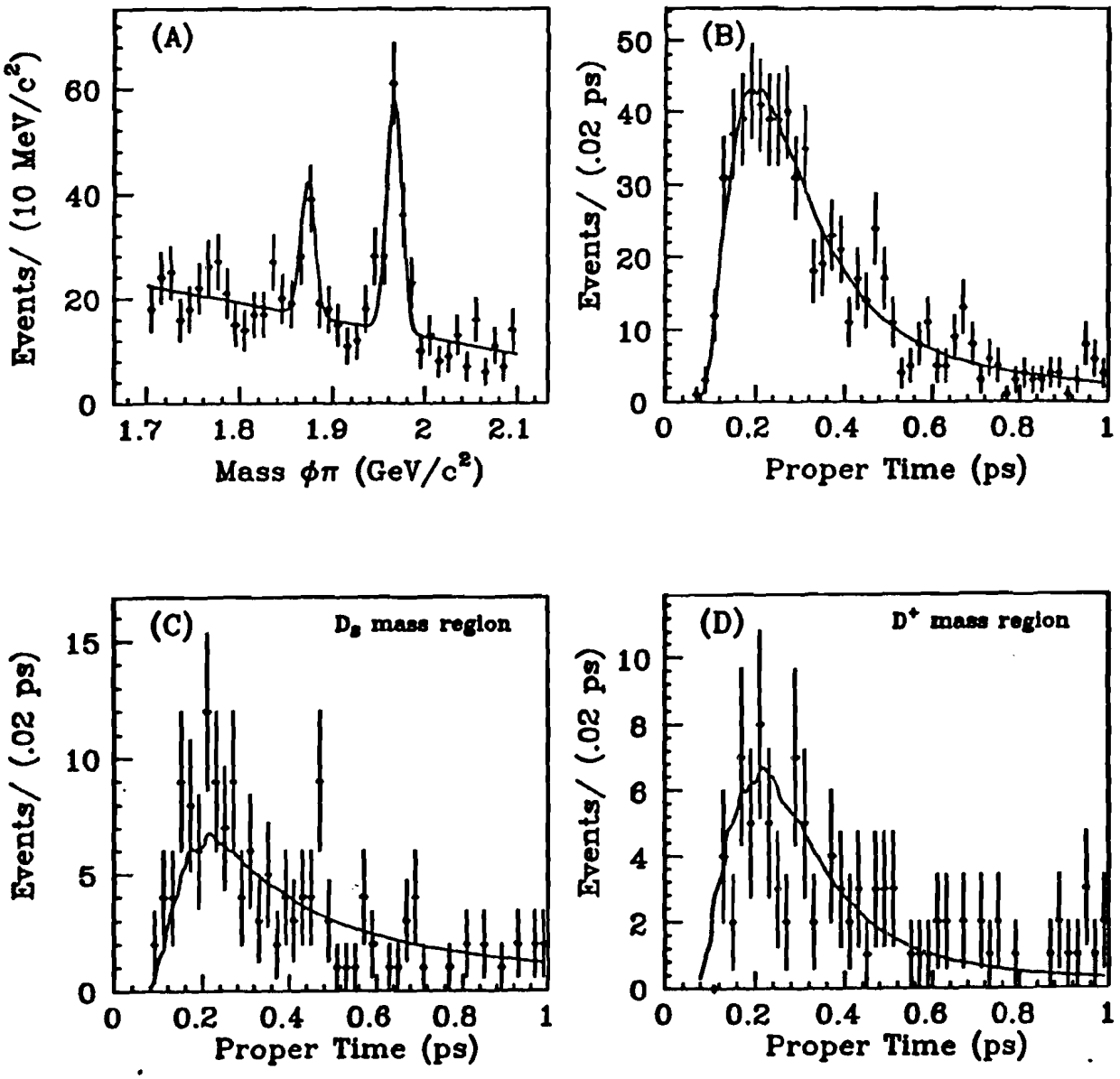

Figure 5.17: Fits to the Data ($f(t_i)$ removed and double exponential background proper time parameterization.)

Table 5.3: FIT PARAMETER RESULTS ($f(t_i)$ =1)

PARAMETER	VALUE	ERROR (±)
N_{D_s}	1.00	*fixed*
μ_{D_s}	1.966	0.001
σ_{D_s}	0.0073	0.0011
A	17.53	3.33
B	-0.418	0.014
C	0.137	0.032
N_D	0.425	0.106
μ_D	1.872	0.001
σ_D	0.0057	0.0013
τ_{D_s}	0.534	0.070
τ_D	1.088	0.192
τ_1	0.113	0.011
τ_2	0.531	0.072

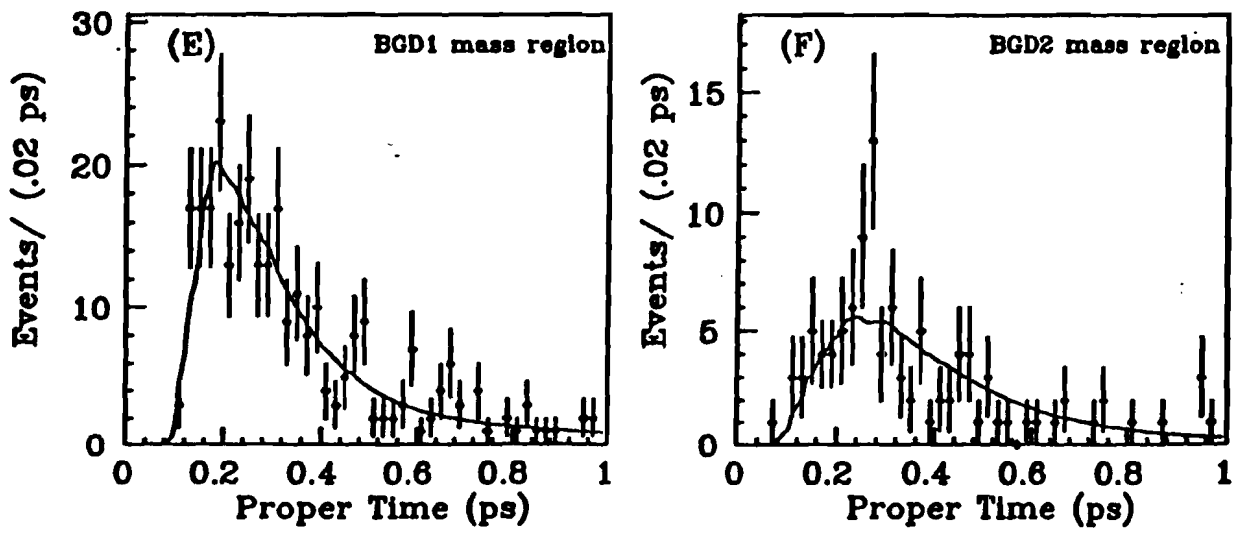

Figure 5.18: Fits to Background Proper Times ($f(t_i)$ removed and double exponential background proper time parameterization.)

Table 5.4: FIT PARAMETER RESULTS (single exponential BG proper time function)

PARAMETER	VALUE	ERROR (±)
N_{D_s}	1.00	*fixed*
μ_{D_s}	1.966	0.001
σ_{D_s}	0.0083	0.0010
A	1.925	0.342
B	-0.419	0.013
C	0.000	*fixed*
N_D	0.423	0.112
μ_D	1.872	0.002
σ_D	0.0076	0.0012
τ_{D_s}	0.531	0.061
τ_D	0.932	0.133
τ_1	0.221	0.009
τ_2	0.000	*fixed*

5.2.3 Single Exponential Background

If the acceptance proper time function, $f(t_i)$, was reinserted into the likelihood function but instead of a double exponential, a single exponential of the form,

$$bg(t_i) = \exp \frac{-t_i}{\tau_1}, \tag{5.26}$$

was used for the background proper time parameterization, the fit produced the values of Table 5.4. The value of the likelihood function, $\mathcal{L} = 4136.1$, was far worse than in the previous two fits.

As in the previous two fits, the final fits to the data and background are shown in Fig. 5.19 and Fig. 5.20. In all of the proper time fits, it was clear that a single exponential did not adequately fit the background proper time distribution. The χ^2/DOF of these plots compared to the other fits is discussed after the next section.

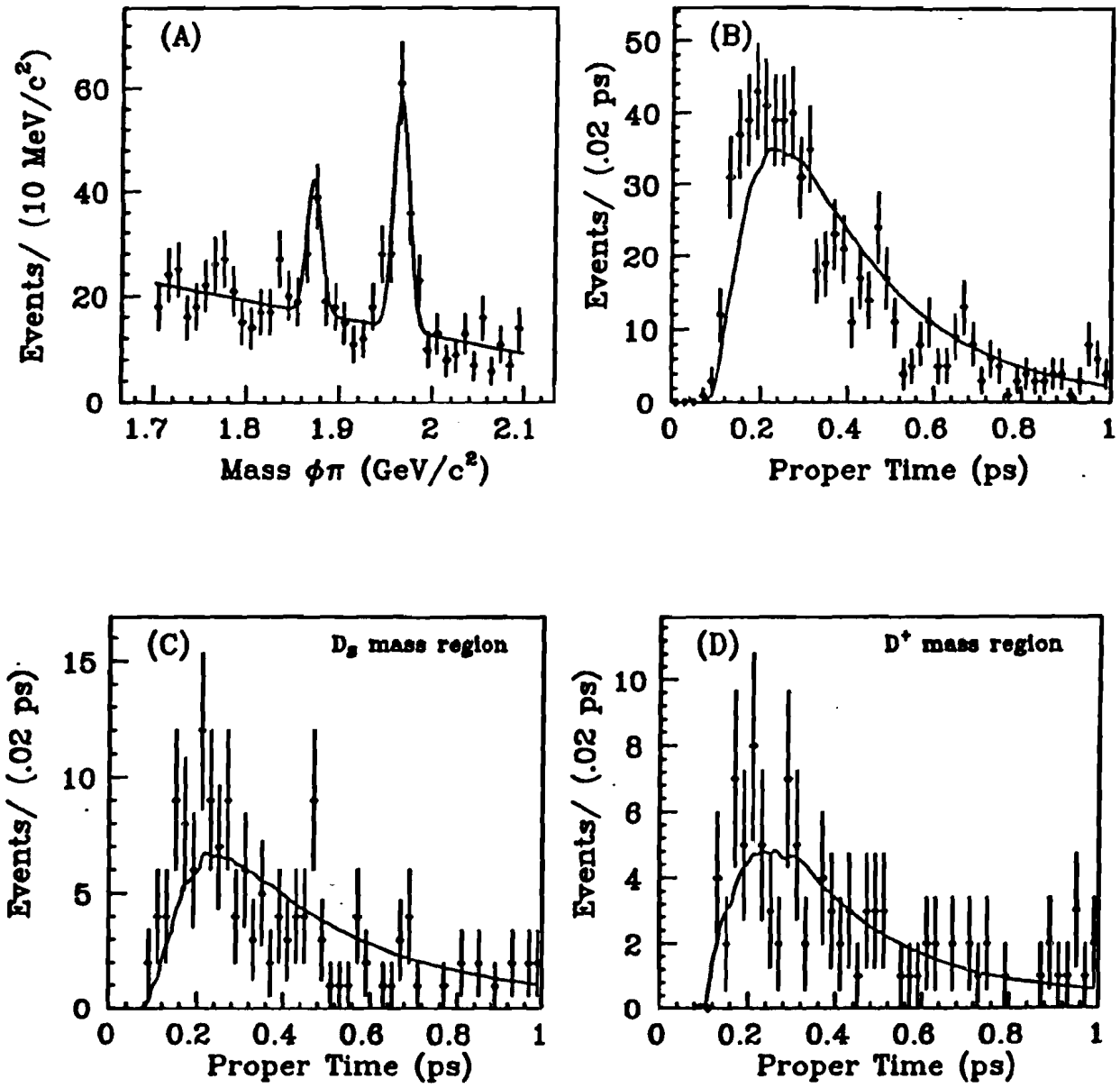

Figure 5.19: Fits to the Data ($f(t_i)$ included and single exponential background proper time parameterization.)

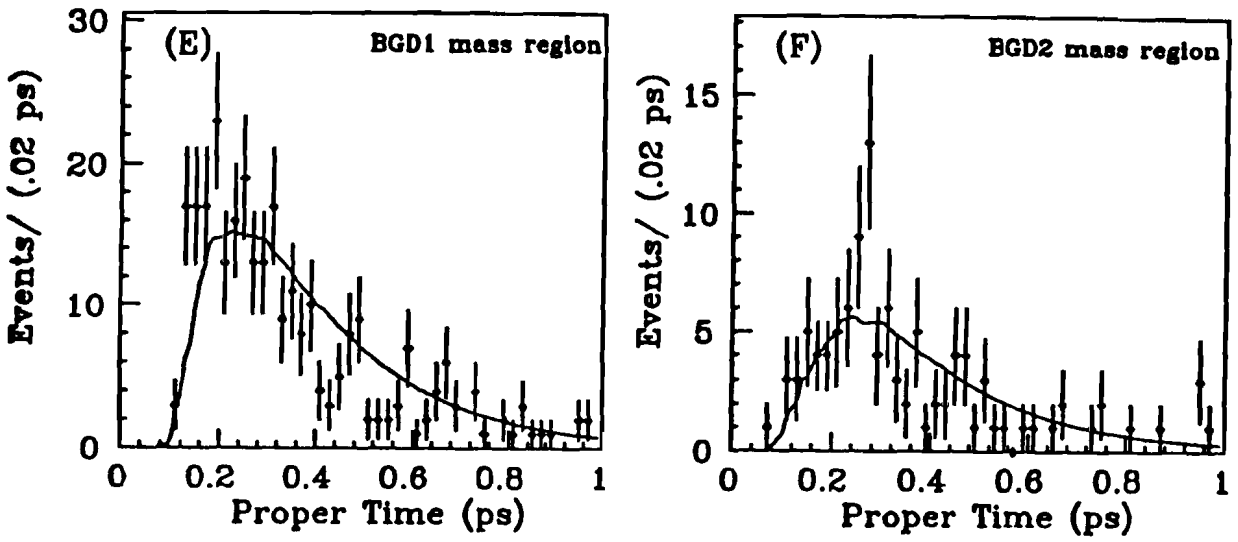

Figure 5.20: Fits to Background Proper Times ($f(t_i)$ included and single exponential background proper time parameterization.)

5.2.4 Parameterization in t'

Rather than parameterizing the proper time with the variable t, the variable t' is often chosen. The variable t' is defined as,

$$t' = t - 3\sigma_\tau. \tag{5.27}$$

With this variable choice, the limits of proper time integration varied between zero and τ'_{max} where,

$$\tau'_{max} = \tau_{max} - 3\sigma_\tau. \tag{5.28}$$

Although this choice of proper time variables produced asthetically pleasing proper time distributions, it had two major flaws.

First, it assumed that the error in the proper time, σ_t, was constant as a function of proper time. This was not the case as shown in Fig. 5.21. These results were obtained from Monte Carlo studies examining the value of σ_τ as a function of proper time. This figure also shows that the error in the proper time is approximately 0.07

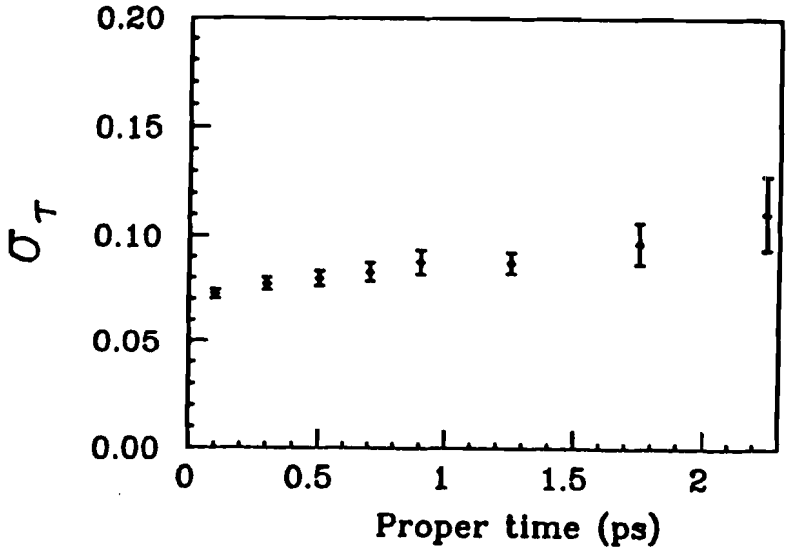

Figure 5.21: Error in the Proper Time as a Function of Proper Time.

picoseconds. Since σ_τ is not constant as a function of proper time, the variable dt becomes

$$dt = dt' - 3d\sigma_\tau. \tag{5.29}$$

This result makes a simple change of variables between t and t' mathematically difficult when calculating normalizations.

Second, the choice of t' made the determination of the acceptance proper time function, $f(t'_i)$, imprecise, since the error in the proper time, σ_t, could not be adequately simulated in the Monte Carlo.

Nonetheless, the proper time was parameterized in terms of this variable to examine the consistency of results. The likelihood function for the variable t' contained no acceptance proper time function but did include a double exponential for the background proper time. In Table 5.5 are displayed the results of the fit. The t' likelihood function had a final value of 4133.2, a result significantly worse than that for the t distribution with $f(t_i)$ removed. The final fits to the data are shown

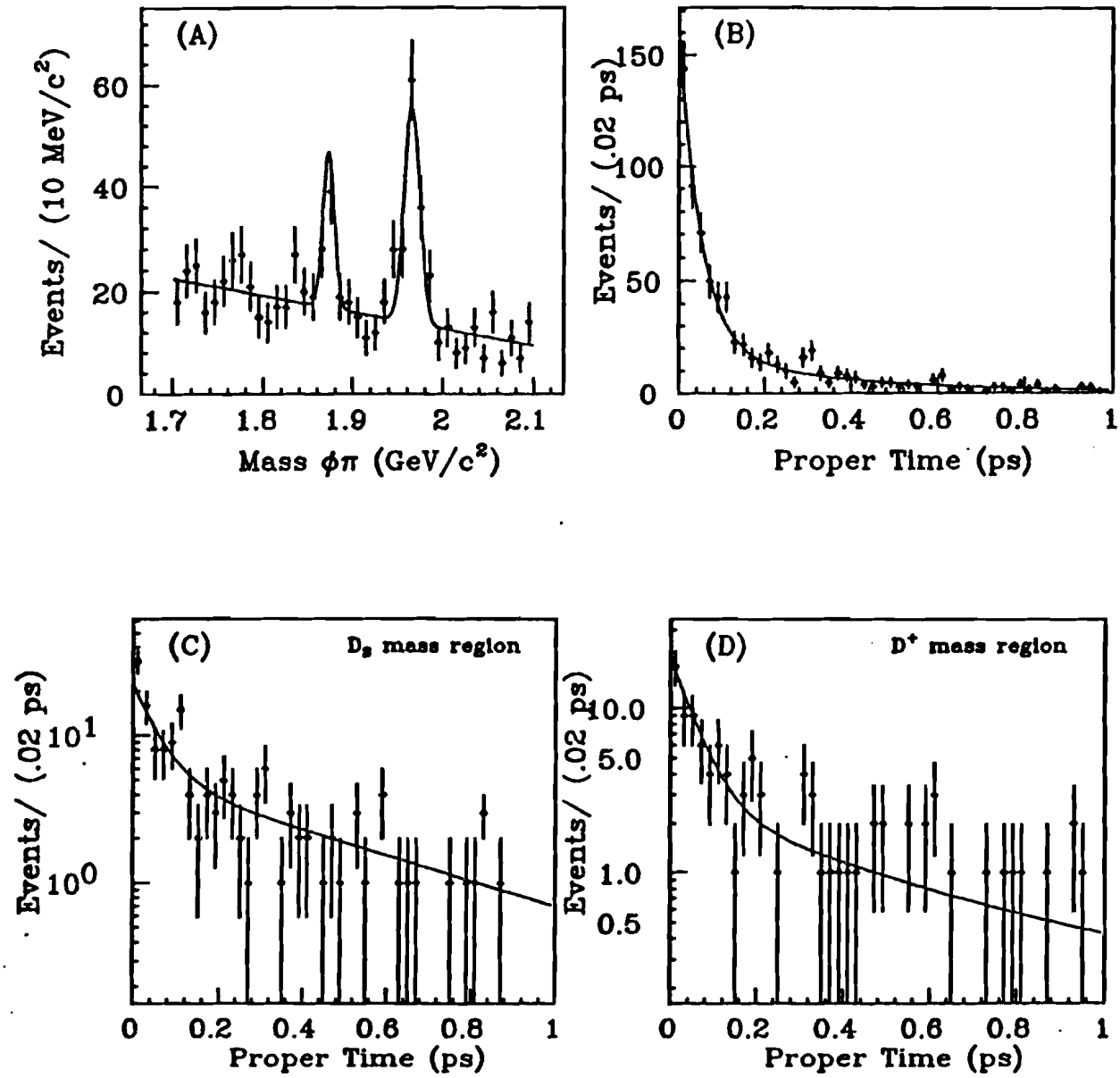

Figure 5.22: Fits to the Data in t' ($f(t_i)$ removed and double exponential background proper time.)

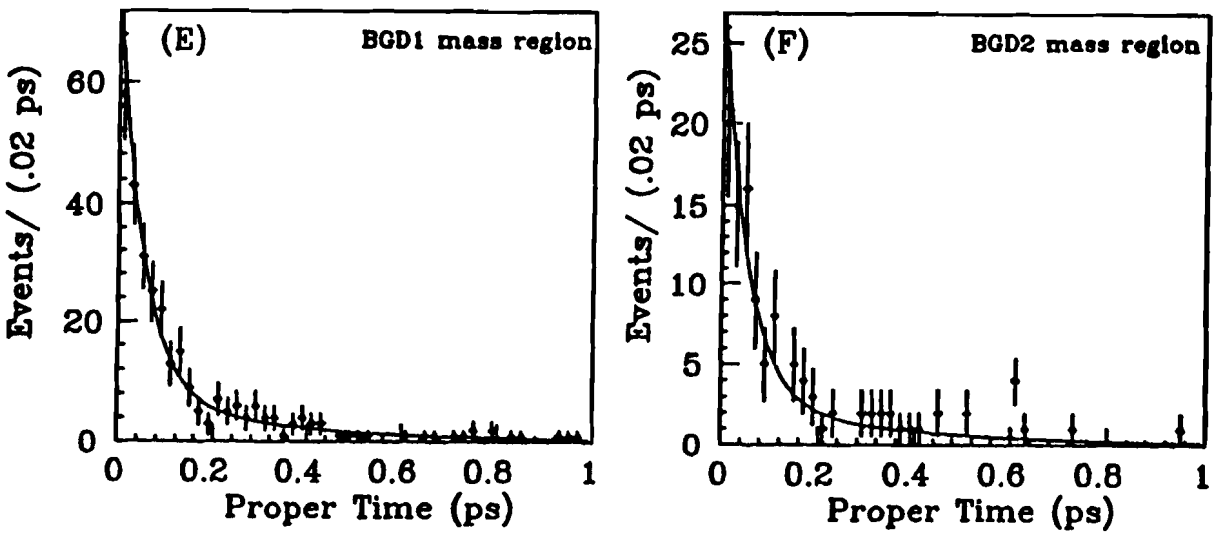

Figure 5.23: Fits to Background Proper Times in t' ($f(t_i)$ removed and double exp. background proper time.)

in Fig. 5.22 and Fig. 5.23.

5.2.5 Comparison of Results

The four previous fits of the likelihood function to the mass and proper time distributions can be categorized as shown in Table 5.6. The fits to the mass and proper time for both the signal and background regions were defined as shown in Table 5.7. The χ^2/DOF values for each of the plots of each fit are compared in Table 5.9. In all four cases, the χ^2/DOF values for the mass plots (A) are similar. This was expected since no variations of the likelihood functions involved the mass contribution of the function. The single exponential parameterization of the background proper times (FIT II) has χ^2/DOF's greater than any of the double exponential fits.

The degree of freedom for each fit was the number of bins in the histogram minus the number of free parameters in the fit. For example, the mass histogram had 40 bins and the fit to the mass distribution had 5 free parameters (σ_{D_s}, μ_{D_s},

Table 5.5: FIT PARAMETER RESULTS (t' distribution ($f(t') = 1$; double exp. background)).

PARAMETER	VALUE	ERROR (±)
N_{D_s}	1.00	*fixed*
μ_{D_s}	1.966	0.001
σ_{D_s}	0.0085	0.0010
A	4.063	0.461
B	-0.419	0.013
C	0.689	0.082
N_D	0.546	0.094
μ_D	1.872	0.002
σ_D	0.0064	0.0010
τ_{D_s}	0.533	0.067
τ_D	1.093	0.183
τ_1	0.052	0.004
τ_2	0.332	0.025

N_D, μ_D and σ_D)[3]. Therefore, the number of degrees of freedom of that fit was 35. The number of DOF for each fit is listed in Table 5.8

The final values of the minimized likelihood functions for each parameterization are compared in Table 5.10. Here both the *standard* and FIT I parameterizations produced the lowest minimum values. The FIT II and FIT III final parameterizations produced significantly higher final values.

In Table 5.11 are presented the D_s^+ and D^+ lifetime results for each likelihood function parameterization. The values are all consistent but the fits with $f(t_i)$ removed produced higher lifetimes as expected.

Because of technique and final fit, the *standard* values of 0.50 ± 0.06 picoseconds for the lifetime of the D_s^+ meson and 0.90 ± 0.13 picoseconds for the lifetime of the D^+ meson were chosen as the quoted lifetimes of this analysis.

[3]The number of parameters should have been six but N_{D_s} was kept constant in the fit.

Table 5.6: COMPARISONS OF 4 FITS

NAME	PROPER TIME	$f(t_i)$ used?	BG PROPER TIME PARAMETERIZATION
standard	t	yes	double exponential
FIT I	t	no	double exponential
FIT II	t	yes	single exponential
FIT III	t'	no	double exponential

Table 5.7: FIT PLOTS

PLOT ID	DEFINITION
(A)	Fit of mass for total mass region
(B)	Fit of proper time for total mass region
(C)	Fit of proper time for D_s^+ mass region (1.94 to 1.99 GeV/c^2)
(D)	Fit of proper time for D^+ mass region (1.85 to 1.89 GeV/c^2)
(E)	Fit of proper time for background mass region I (1.70 to 1.85 GeV/c^2)
(f)	Fit of proper time for background mass region II (1.99 to 2.1 GeV/c^2)

Table 5.8: DOF FOR EACH FIT

FIT	NO. OF BINS	NO. OF FREE PARAMETERS	DOF
(A)	40	5	35
(B)	50	5	45
(C)	50	1	49
(D)	50	1	49
(E)	50	3	47
(F)	50	3	47

Table 5.9: χ^2/DOF COMPARISONS

FIT	χ^2/DOF(*standard*)	χ^2/DOF(FIT I)	χ^2/DOF(FIT II)	χ^2/DOF(FIT III)
(A)	1.92	1.89	1.84	1.96
(B)	1.69	1.38	3.39	1.58
(C)	1.14	1.18	1.72	1.30
(D)	1.00	0.90	1.08	0.67
(E)	0.97	0.97	2.21	0.66
(F)	0.64	0.64	0.99	0.79

Table 5.10: FINAL LIKELIHOOD FUNCTION VALUES

PARAMETERIZATION	LIKELIHOOD FUNCTION VALUE
standard	4077.7
FIT I	4078.1
FIT II	4136.1
FIT III	4133.2

Table 5.11: LIFETIME RESULT COMPARISONS (IN PICOSECONDS)

LIFETIME	*standard*	FIT I	FIT II	FIT III
D_s^+	0.50 ± 0.06	0.53 ± 0.07	0.52 ± 0.06	0.54 ± 0.07
D^+	0.90 ± 0.13	1.09 ± 0.19	0.93 ± 0.13	1.10 ± 0.18

5.3 Errors in the Lifetime Results

The uncertainties in the lifetime measurements were then studied with the systematic errors yet to be determined. Once again, the *standard* values of the lifetimes produced by this analysis are $\tau(D_s) = 0.50 \pm 0.06$ picoseconds and $\tau_D = 0.90 \pm 0.13$ picoseconds.

5.3.1 Statistical Errors

The statistical error in the lifetime measurement for a background-free sample of N decays is approximately [37],

$$\delta\tau = \sqrt{\frac{\tau^2 + (\delta t)^2}{N}}, \tag{5.30}$$

where τ is the measured lifetime and δt is the experimental resolution in the proper time.

The experimental resolution was obtained by plotting the difference, *difft* $= t_{mc} - t_{recon}$, the difference between the input proper time and the reconstructed proper time as found in the Monte Carlo data. As shown in Fig. 5.24 where *difft* is fit with a Gaussian function plus an exponential. The exponential component was needed to fit a slight assymmetry for positive values of *difft*. The width of the fit is 0.07 picoseconds. This reconfirms the results of Fig. 5.21.

Given an experimental resolution of 0.07 picoseconds in the proper time, 104 events and a lifetime measurement of 0.50 picoseconds for the D_s^+ , $\delta\tau$ is estimated to be 0.05 picoseconds. For the D^+ measurement with 50 events and a measured lifetime of 0.90 picoseconds, this calculation gave 0.13 picoseconds. Both of these results are similar to the errors of $\pm$ 0.06 picoseconds (D_s^+) and $\pm$ 0.13 picoseconds (D^+) determined by MINUIT.

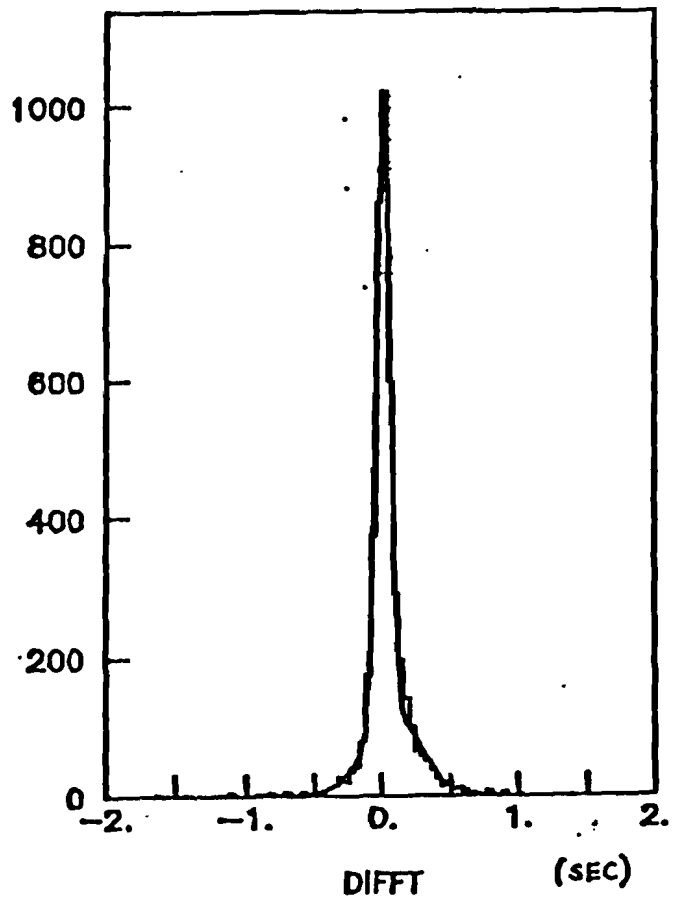

Figure 5.24: Distribution of The Difference between Input and Reconstructed Proper Times for Monte Carlo Data.

5.3.2 Systematic Errors

Systematic errors were estimated from various studies on the data and Monte Carlo data sets. This was accomplished by the following five methods.

I. Monte Carlo

Nearly 50,000 ROGUE Monte Carlo events were generated with $D_s^+ \rightarrow \phi\pi \rightarrow (K^+K^-)\pi^+$. Given an input D_s^+ lifetime of 0.436 picoseconds, the input proper time distribution produced a lifetime of 0.436 picoseconds as shown in Fig. 5.6. Analysis cuts were then performed on the MC data set to examine the analysis technique and experimental calibration. The associated proper time distributions for various L/σ_L cuts were studied. A likelihood function, F_i, was constructed of the form,

$$F_i = \frac{\frac{1}{\tau}\exp\frac{-t_i}{\tau}}{\int_{\tau_{min_i}}^{\tau_{max_i}} \frac{1}{\tau}\exp\frac{-t_i}{\tau}}, \tag{5.31}$$

since no background was involved in the plots. This function was then maximized to determine the D_s^+ lifetime.

The results of the fits of the D_s^+ proper times from the Monte Carlo for various cuts on the variable L/σ_L is presented in Fig. 5.25. These values are somewhat higher than the input lifetime. This is not surprising since the likelihood function has no acceptance correction. If an acceptance function, $\tilde{f}(t_i)$,[4] is included, then the likelihood function becomes,

$$F_i = \frac{\frac{1}{\tau}\tilde{f}(t_i)\exp\frac{-t_i}{\tau}}{\int_{\tau_{min_i}}^{\tau_{max_i}} \frac{1}{\tau}\tilde{f}(t_i)\exp\frac{-t_i}{\tau}}. \tag{5.32}$$

These results are plotted in Fig. 5.26 showing much greater agreement. Clearly the likelihood function technique is accurate in the determination of the D_s^+ lifetime

[4]Compared to previous $f(t_i)$ functions, this $\tilde{f}(t_i)$ contained no contribution from absorption of decay particles in the target.

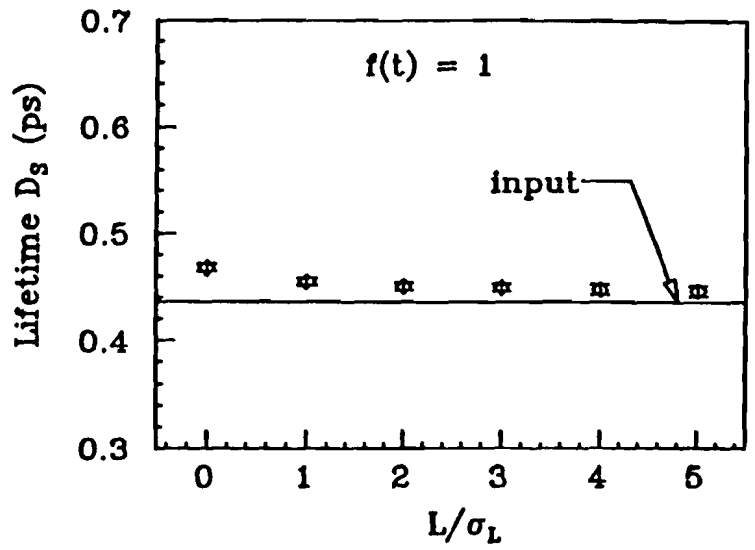

Figure 5.25: Calculated D_s^+ Lifetimes from Monte Carlo.

in MC data. The Monte Carlo seems to be accurate in its modelling of the reconstructed proper times.

II. Large L/σ_L Cuts on the Data

A study of the data events with $L/\sigma_L > 5$ and higher was useful for a few reasons. First, the background proper time parameterization could be ignored in these nearly "background free" event samples allowing an examination of the effect of the background parameterization on the D_s^+ and D^+ lifetime measurements. Second, a variation of the L/σ_L cuts at these higher values showed how a few remaining background events were affecting the measurement, although not considered in the likelihood function. Finally one could study how larger values of τ_{min} and resulting smaller event samples were influencing the lifetime measurement.

In Fig. 5.27 are exhibited four mass plots for the $\phi\pi^+$ events with $L/\sigma_L > 5$, > 6, > 7 and > 8. The D_s^+ events were selected with a mass cut of 1.94 GeV/c^2 to 1.99 GeV/c^2 , while the D^+ events were in the range 1.85 GeV/c^2 to 1.90 GeV/c^2 .

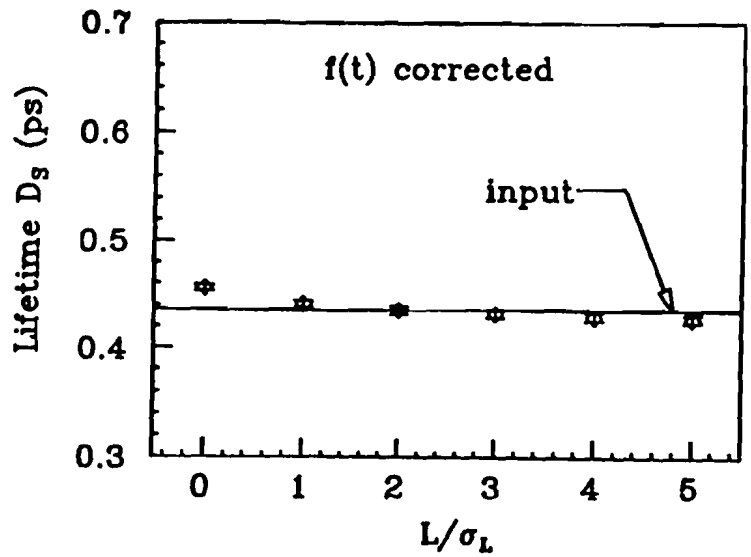

Figure 5.26: Calculated D_s^+ Lifetimes from Monte Carlo with $f(t_i)$ Correction.

In Fig. 5.28 are displayed the fit results of the D_s^+ lifetime for these L/σ_L values as compared to the *standard* value. The acceptance function $f(t_i)$ (absorption and acceptance included) was incorporated into these fits. This plot shows a fairly stable D_s^+ lifetime, although it has some tendency to increase with higher L/σ_L .

In Fig. 5.29 are displayed the fit results for the D^+ . Here a continuous increase in the D^+ lifetime is seen. This may be due to short lived background contamination at lower L/σ_L values. Except for the D^+ lifetime at $L/\sigma_L > 5$, the results of Fig. 5.29 are consistent with the *standard* value of the D^+ lifetime.

III. Mass Range

The mass range of the fit (1.7 GeV/c^2 to 2.1 GeV/c^2) was originally chosen to exhibit signal regions and also allow some background bands on both sides of these regions. Opening the mass range to a larger spread would facilitate the background proper time parameterizaton, while tightening the mass cut would make this more difficult. The two mass ranges chosen to study this were (1.4 GeV/c^2 to 2.4

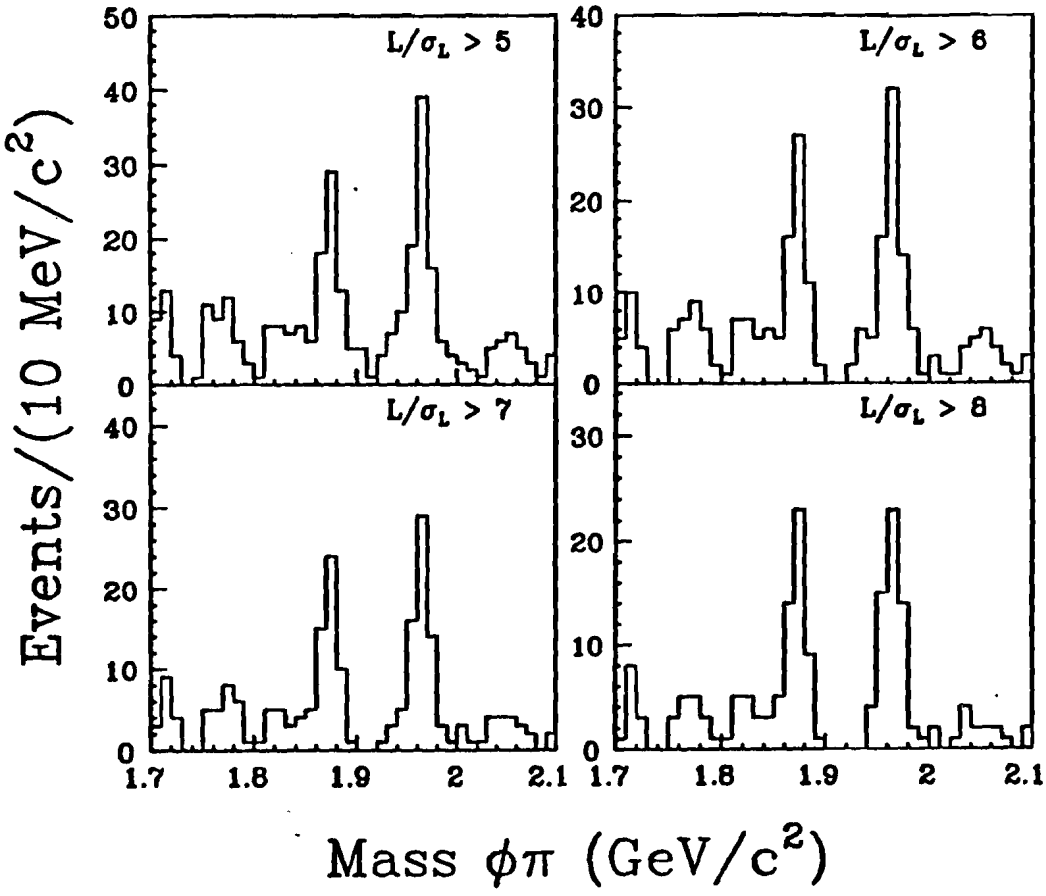

Figure 5.27: $\phi^0\pi^+$ Mass Plots with Higher Values of L/σ_L .

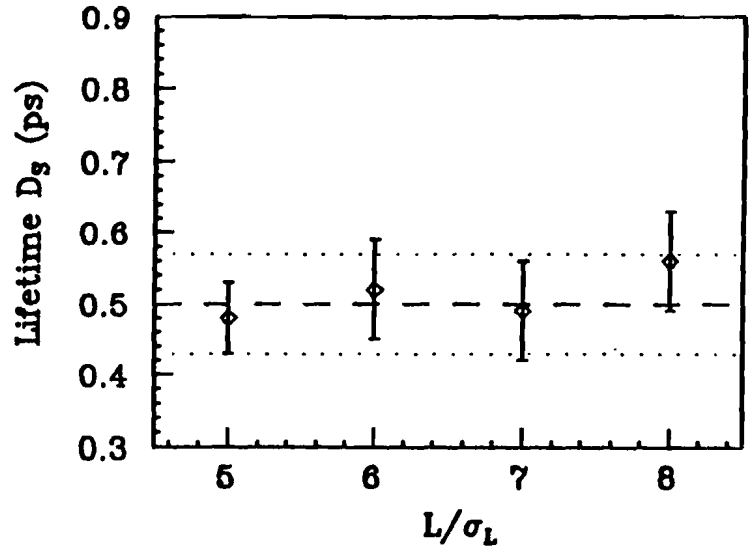

Figure 5.28: D_s^+ Lifetime Measurements for High L/σ_L Values (background ignored).

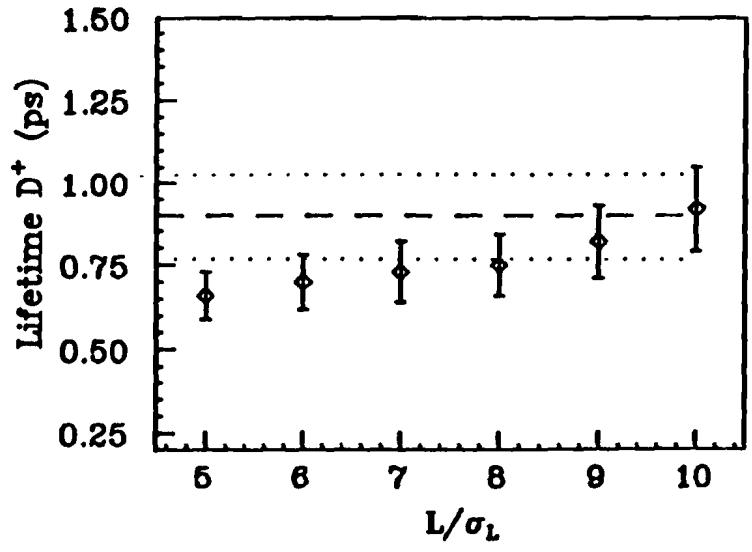

Figure 5.29: D^+ Lifetime Measurements for High L/σ_L Values (background ignored).

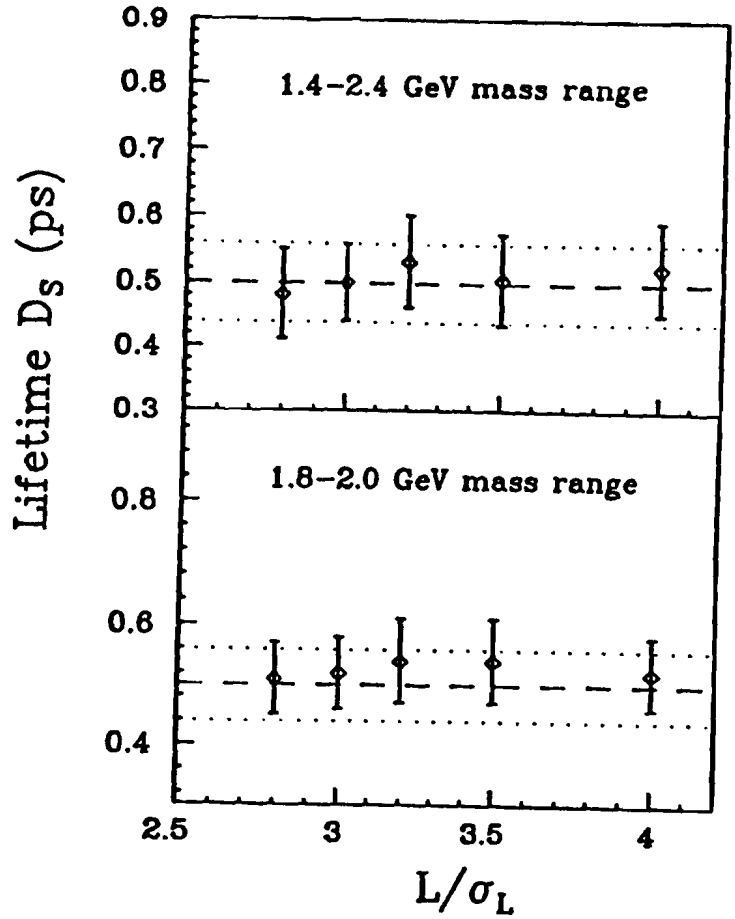

Figure 5.30: Calculated D_s^+ Lifetimes of Different Mass Ranges and Values of L/σ_L .

GeV/c^2) and (1.8 GeV/c^2 to 2.0 GeV/c^2). Since nearly no background side bands were present in the (1.8 GeV/c^2 to 2.0 GeV/c^2) plot, the background parameters were kept constant in the fit.

In Fig. 5.30 is plotted the measured D_s^+ lifetime as a function of the L/σ_L cut for both the large and small mass ranges. These fits to mass and proper time were done with the full likelihood fit (the *standard* fit). The D^+ lifetime is plotted in a similar manner in Fig. 5.31. Both samples produced consistent results.

IV. Taumax

By varying the maximum decay distance, the values of τ_{max} could be varied. This was accomplished by assigning various values to the downstream Z-coordinate

limit of the D_s^+ and D^+ decay vertices. Given the nominal Z-coordinate decay limit at TR1 (+2.5 cm), the following other Z-coordinate decay limits were chosen, +2.5 cm, +2.3 cm, +2.0 cm and +1.7 cm. No Z-coordinate decay limits downstream of TR1 were chosen [5]. The values of the D_s^+ and D^+ lifetimes (for various values of L/σ_L) obtained from the data as a function of the Z-coordinate decay limit are shown in Fig. 5.32. These choices of the Z-coordinate decay limit do not seem to affect the lifetime measurements in any major sense. This can be understood by examining Fig. 4.15 which shows the values of L, the separation between primary and secondary vertices. Most of these distances were less than 2.0 centimeters.

V. L/σ_L Cuts with the Full Fit

One final way to examine the D_s^+ and D^+ lifetimes was to apply the full fit ($f(t_i)$ included and double exponential background proper time) to the $\phi\pi^+$ event samples with L/σ_L cuts greater than the standard, $L/\sigma_L > 3$. As required previously, the background parameters had to be kept constant for nearly background free L/σ_L plots. The measured D_s^+ lifetimes for various L/σ_L cuts compared to the *standard* value are displayed in Fig. 5.33. In Fig. 5.34 are similarly displayed the measured D^+ lifetimes for various L/σ_L cuts.

5.3.3 Conclusions

From these studies it was estimated that the systematic errors in the D_s^+ and D^+ lifetime measurements were about ± 0.03 picoseconds and ± 0.05 picoseconds, respectively. Thus the final lifetime measurement yields,

$$\tau(Ds) = 0.50 \pm 0.06 \pm 0.03 \text{ picoseconds} \tag{5.33}$$

[5] In a study of 50K ROGUE events, only a handful decayed beyond the nominal Z position of TR1.

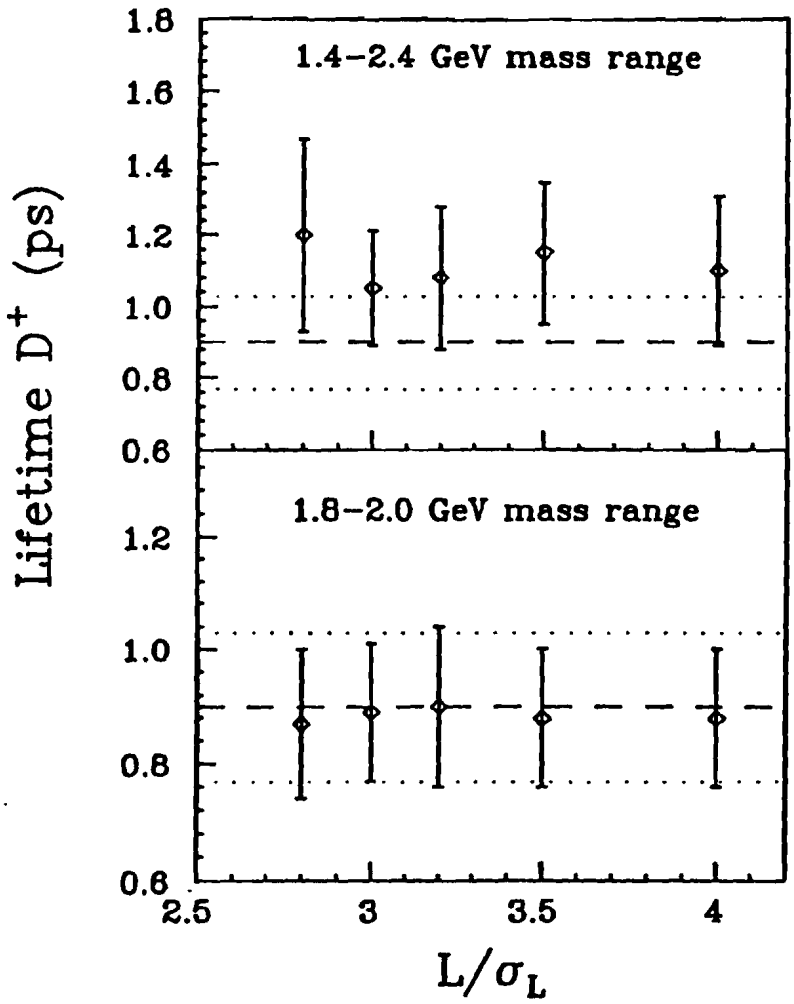

Figure 5.31: Calculated D^+ Lifetimes of Different Mass Ranges and Values of L/σ_L .

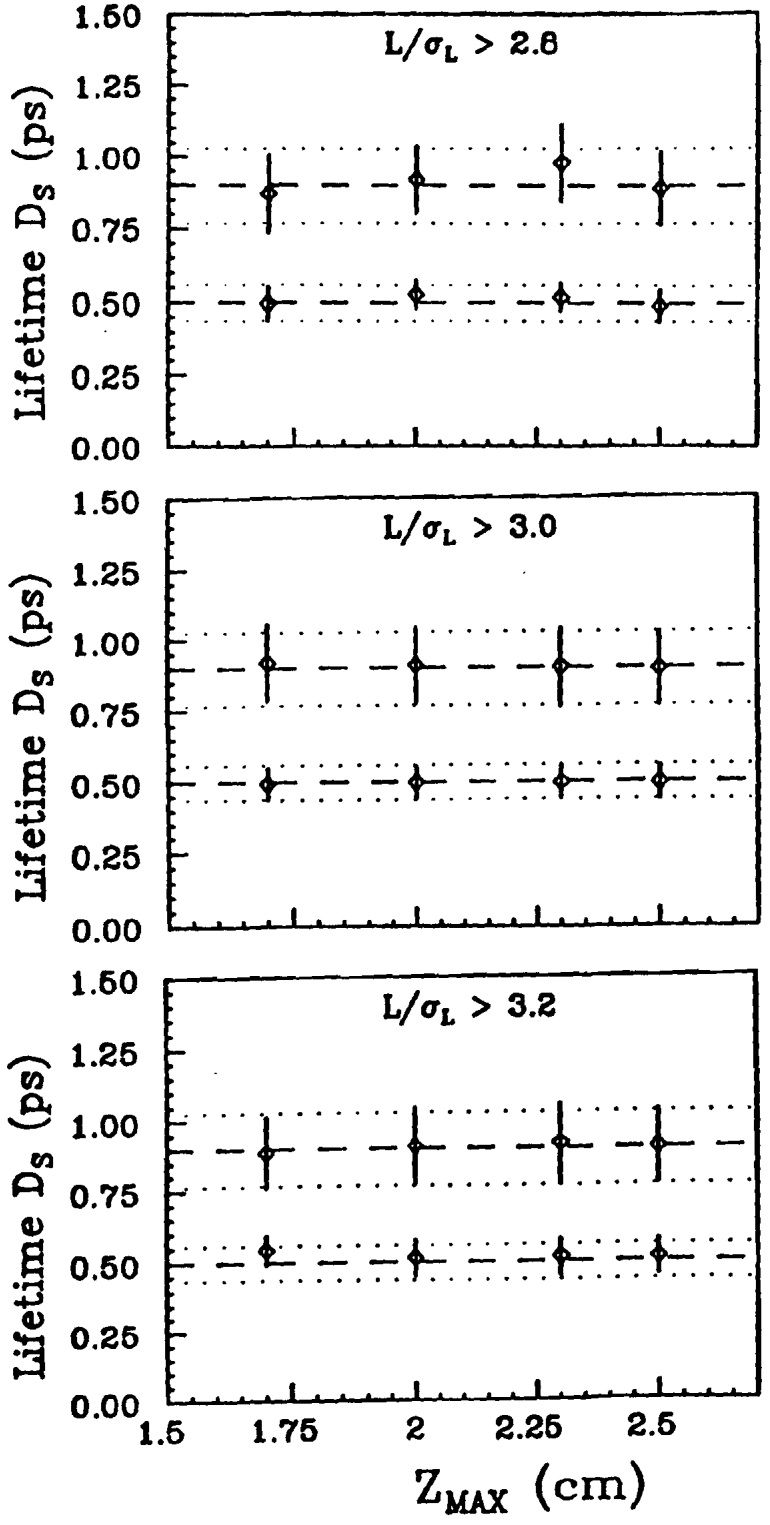

Figure 5.32: Calculated D_s^+ and D^+ Lifetimes as a Function of Z-coordinate Decay Limits.

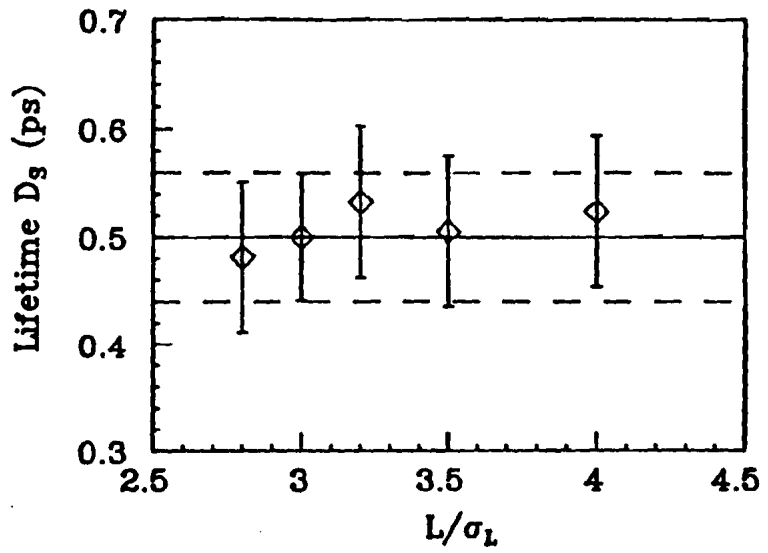

Figure 5.33: D_s^+ Lifetimes as a Function of L/σ_L cut (full fit).

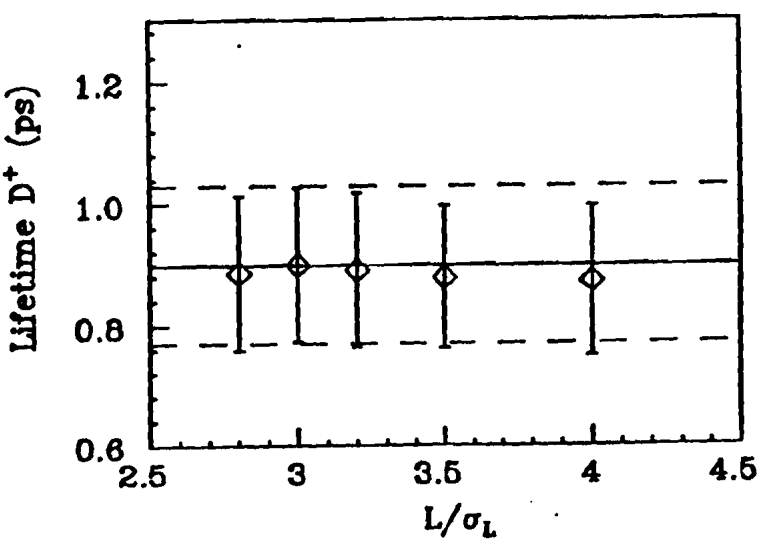

Figure 5.34: D^+ Lifetimes as a Function of L/σ_L cut (full fit).

and

$$\tau(D^+) = 0.90 \pm 0.13 \pm 0.05 \text{ picoseconds} \tag{5.34}$$

These values are compared to the lifetime measurements of other experiments in the final chapter of this thesis.

CHAPTER 6

BRANCHING RATIO ANALYSIS

Two relative branching ratio measurements are described in this chapter. These ratios are the branching ratio BR($D_s^+ \rightarrow \phi^0\pi^+\pi^-\pi^+$) relative to BR($D_s^+ \rightarrow \phi^0\pi^+$) and BR($D^+ \rightarrow \phi^0\pi^+\pi^-\pi^+$) relative to BR($D^+ \rightarrow \phi^0\pi^+$). The analysis cuts used to select the events are first discussed. The chapter is concluded with a description of the relative branching measurement technique and associated results.

6.1 Analysis Cuts

A search was made for D_s^+ and D^+ events that decayed to $\phi^0\pi^+\pi^-\pi^+$. The decay mode $D_s^+ \rightarrow \phi^0\pi^+\pi^-\pi^+$ is also Cabibbo-favored but should be somewhat suppressed by phase space factors (in comparison to $D_s^+ \rightarrow \phi^0\pi^+$). Similarly, the mode $D^+ \rightarrow \phi^0\pi^+\pi^-\pi^+$ is Cabibbo-suppressed and would be further suppressed by phase space factors in comparison to $D^+ \rightarrow \phi^0\pi^+$.

Since the decay mode $D_s^+ \rightarrow \phi^0\pi^+$ is the best established decay mode of the D_s^+, and since absolute branching ratios are difficult to determine, branching ratios of the other modes of the D_s^+ meson are measured relative to this mode. As yet there is no absolute branching ratio measurement of the mode $D_s^+ \rightarrow \phi^0\pi^+$, but indirect arguments indicate a value of approximately 4% [38][39][40]. Recent results utilizing the decay $D_s^+ \rightarrow \phi^0 l^+\nu$ (where l^+ is a lepton and ν is the associated neutrino) put

this value at $3.1 \pm 0.6^{+0.9}_{-0.6} \pm 0.6\%$, where the first error is statistical, the second is systematic and the third error is the systematic uncertainty due to the predicted value of $\mathrm{BR}(D_s^+ \rightarrow \phi^0 l^+ \nu)$ [41].

The search for $D_s^+ \rightarrow \phi^0 \pi^+ \pi^- \pi^+$ began with many of the same analysis cuts as the $\phi^0 \pi^+$ analysis, but a few modifications were made. To reduce the combinatoric background, a somewhat more stringent Čerenkov requirement was made on pion candidate tracks. Unlike the $\phi^0 \pi^+$ analysis, a vertex requirement was imposed on the primary vertex. Specifically these cuts required that:

1. Kaons were identified as tracks having ISTATP = 4, 12. Tracks with an ISTATP value of 7 and momentum greater than 60 GeV/c were also assumed to be kaon tracks. (These are the same kaon identification requirements as in the $\phi^0 \pi^+$ analysis.)

2. The mass of the K^+K^- pair was required to be (1.01 GeV/c^2 $< M_{K^+K^-} <$ 1.03 GeV/c^2). This too was the same ϕ^0 cut as in the $\phi^0 \pi^+$ analysis.

3. Two out of three pions were required to be identified as either "pion definite" or "electron/pion ambiguous" (ISTATP = 2 or 3). The third pion candidate track was required not to be identified as an electron, kaon or proton (ISTATP $\neq$ 1, 4, 8, 12) [1].

4. The confidence level for the primary vertex fit was required to be greater than 3%.

5. The primary vertex was required to be in the target region and the secondary vertex was required to be downstream of the primary vertex.

[1] These are the same Čerenkov requirements on the π^+ as in the $\phi^0 \pi^+$ analysis.

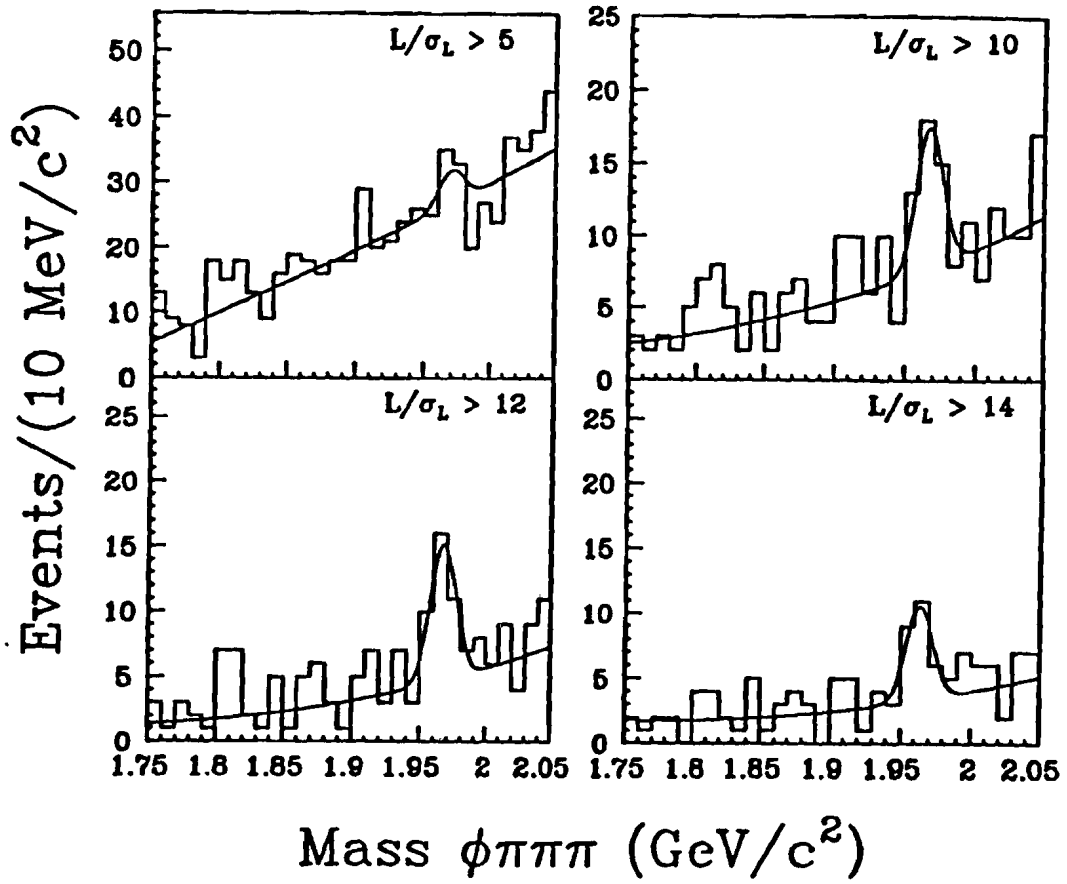

Figure 6.1: Fitted Invariant Mass Plot of $\phi^0\pi^+\pi^-\pi^+$ Events as a Function of the L/σ_L Cut.

6. The separation between primary and secondary vertices (divided by the error in this quantity) was required to have a value of $L/\sigma_L >$ N, where N was typically a large number (compared to those used in the $\phi^0\pi^+$ analysis) to reduce the combinatoric background further.

The invariant mass distribution for $\phi^0\pi^+\pi^-\pi^+$ events passing the analysis cuts is plotted as a function of the L/σ_L cut in Fig 6.1. The signal was fit with a Gaussian, while the background mass distribution was fit with a second order polynomial.

The $\phi^0\pi^+\pi^-\pi^+$ events that passed a cut of $L/\sigma_L > 12$ were chosen for the

Table 6.1: $D_s^+ \to \phi^0\pi^+\pi^-\pi^+$ FIT RESULTS

L/σ_L	NO. OF EVENTS	MASS (GeV/c^2)	σ (GeV/c^2)	S/B
> 5	12.1 ± 10.8	1.967 ± 0.003	0.009 ± 0.005	0.1
> 10	21.8 ± 8.1	1.967 ± 0.003	0.007 ± 0.004	0.6
> 12	20.8 ± 6.7	1.967 ± 0.003	0.008 ± 0.003	1.1
> 14	16.1 ± 5.8	1.967 ± 0.003	0.007 ± 0.003	0.9

$D_s^+ \to \phi^0\pi^+\pi^-\pi^+$ branching ratio measurement. The fit to these events yielded a substantial event yield and a high ratio of signal to background as seen in Table 6.1, where event yield, mass, signal width and the ratio of signal to background of the D_s^+ signal region for each plot of Fig. 6.1 are listed.

As seen from Table 6.1, the $D_s^+ \to \phi^0\pi^+\pi^-\pi^+$ events with $L/\sigma_L > 12$ (as well as those for the other L/σ_L cuts) had a mean mass of 1.967 ± 0.003 GeV/c^2 and a width of 0.008 ± 0.003 GeV/c^2 . These results were very similar to the $D_s^+ \to \phi^0\pi^+$ ($L/\sigma_L > 3$) fit results (where $\bar{m}_{D_s} = 1.967 \pm 0.002$ GeV/c^2 and $\sigma_{D_s} = 0.011 \pm 0.003$ GeV/c^2). The D_s^+ masses were consistent, but the width of the D_s^+ was somewhat narrower for $\phi^0\pi^+\pi^-\pi^+$ events compared to $\phi^0\pi^+$ events.

The fitting routine was required to fit two possible signal regions (D_s^+ , D^+) in the $\phi^0\pi^+\pi^-\pi^+$ mass distribution. No $D^+ \to \phi^0\pi^+\pi^-\pi^+$ events were found. If the D^+ mass and signal width were fixed in the fit, the plot in Fig. 6.2 resulted. This constrained fit on the $\phi^0\pi^+\pi^-\pi^+$ ($L/\sigma_L > 12$) events yielded a signal of 4.9 ± 3.1 ($D^+ \to \phi^0\pi^+\pi^-\pi^+$) events.

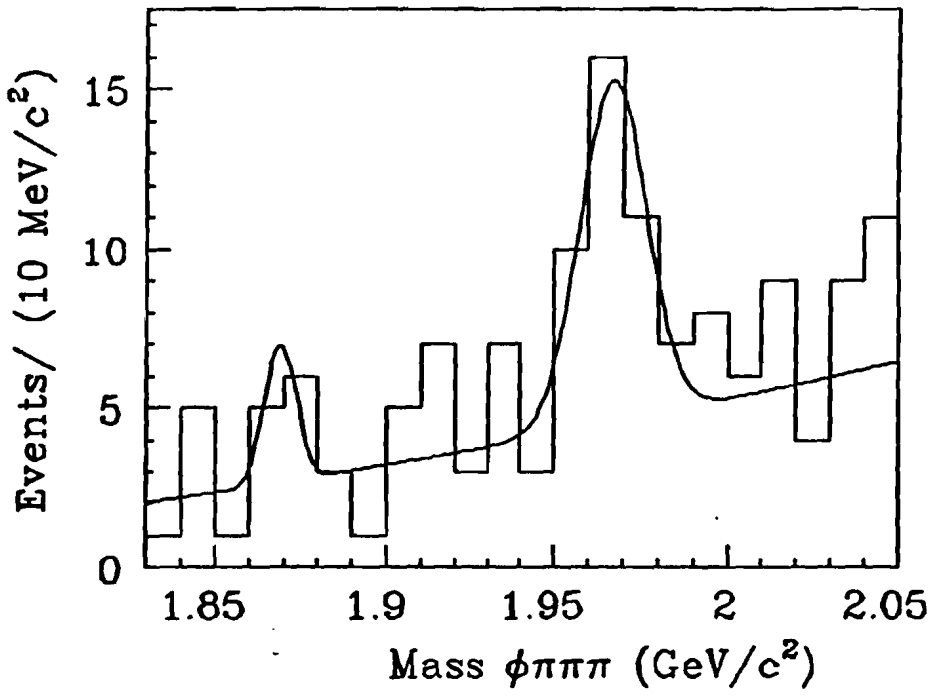

Figure 6.2: Fitted Invariant Mass Plot of $\phi^0\pi^+\pi^-\pi^+$ (D^+ mass and signal width constrained).

6.2 Branching Ratio Analyses

6.2.1 $\mathrm{BR}(D_s^+ \to \phi^0\pi^+\pi^-\pi^+)/\mathrm{BR}(D_s^+ \to \phi^0\pi^+)$ Measurement

The relative branching ratio was determined from the observed event yields in the data sample and from the efficiency of extracting that mode as determined by Monte Carlo (MC) studies. Using the same technique as Chapter 4, the efficiency was determined by applying the same analysis cuts used for the data to a large sample (20,000) of MC generated events. The number of events remaining after each successive cut was then used to calculate this efficiency. The Monte Carlo data set was generated according to: $\gamma g \to D_s^+ \bar{C} \to \phi^0\pi^+\pi^-\pi^+\bar{C} \to K^+K^-\pi^+\pi^-\pi^+\bar{C}$ [2]. Just as in Chapter 4, the analysis cuts applied to the MC data set began with the requirements of the master gate and second level trigger and concluded with L/σ_L cuts. The $D_s^+ \to \phi^0\pi^+\pi^-\pi^+$ analysis cuts as well as their associated efficiencies and the errors in these efficiencies are listed in Table 6.2.

The efficiency for extracting $D_s^+ \to \phi^0\pi^+$ from a Monte Carlo data set was presented in Chapter 4. As a reminder, the MC efficiency for finding $D_s^+ \to \phi^0\pi^+$ events with $L/\sigma_L > 3$ (and all other analysis cuts) was 13.6 ± 0.1%. The number of D_s^+ events (data), associated efficiencies (MC) and errors in the efficiencies for each decay mode are listed in in Table 6.3.

The relative branching ratio is then calculated as,

$$\frac{\mathrm{BR}(D_s^+ \to \phi^0\pi^+\pi^-\pi^+)}{\mathrm{BR}(D_s^+ \to \phi^0\pi^+)} = \frac{N(D_s^+ \to \phi^0\pi^+\pi^-\pi^+)}{N(D_s^+ \to \phi^0\pi^+)} \cdot \frac{\epsilon(\phi^0\pi^+)}{\epsilon(\phi^0\pi^+\pi^-\pi^+)} \tag{6.1}$$

producing a result of:

$$\frac{\mathrm{BR}(D_s^+ \to \phi^0\pi^+\pi^-\pi^+)}{\mathrm{BR}(D_s^+ \to \phi^0\pi^+)} = 0.58 \pm 0.21 \pm 0.10. \tag{6.2}$$

[2] The $\bar{C}$ or 'charmbar' particle was discussed in Chapter 4.

Table 6.2: EFFICIENCY STUDY OF $D_s^+ \to \phi^0\pi^+\pi^-\pi^+$

CUT	% OF TOTAL	$\sigma(\epsilon)$ %
Master gate	89.8	0.9
Master gate and 2nd level trigger	44.5	0.6
ϕ^0 cut	41.3	0.5
Čerenkov requirements on π's	30.6	0.4
DVERT succeeds	26.6	0.4
Target cuts	26.2	0.4
CL(primary vertex) > 0.03	21.0	0.4
$L/\sigma_L > 0$	16.8	0.3
$L/\sigma_L > 5$	9.9	0.2
$L/\sigma_L > 10$	5.9	0.2
$L/\sigma_L > 12$	4.7	0.2
$L/\sigma_L > 14$	3.4	0.1

Table 6.3: EVENT COUNT AND EFFICIENCIES FOR D_s^+

MODE	NO. OF EVENTS (DATA)	EFFICIENCY (MC) (%)	$\sigma(\epsilon)$ %
$D_s^+ \to \phi^0\pi^+$	103.7 ± 14.8	13.6	0.1
$D_s^+ \to \phi^0\pi^+\pi^-\pi^+$	20.8 ± 6.7	4.7	0.2

The systematic error was estimated by varying the L/σ_L cut on the $\phi^0\pi^+\pi^-\pi^+$ events and calculating the quotient of branching ratios. The value of 0.58 ± 0.20 ± 0.10 is compared to the world average of this quantity in the next chapter.

6.2.2 BR($D^+ \rightarrow \phi^0\pi^+\pi^-\pi^+$)/BR($D^+ \rightarrow \phi^0\pi^+$) Measurement

The ratio of branching ratios for the D^+ events was calculated in a similar manner as the D_s^+ ratio. Since the number of $D^+ \rightarrow \phi^0\pi^+\pi^-\pi^+$ data events was nearly consistent with zero, the upper limit (90% confidence level) for this ratio was calculated. Once again, the Monte Carlo efficiency for extracting this D^+ mode was determined by applying all of the analysis cuts to a comparable MC data set. The Monte Carlo data set used in this case was $\gamma g \rightarrow D^+ \bar{C} \rightarrow \phi^0\pi^+\pi^-\pi^+\bar{C} \rightarrow K^+K^-\pi^+\pi^-\pi^+\bar{C}$. The $D^+ \rightarrow \phi^0\pi^+\pi^-\pi^+$ analysis cuts as well as their associated efficiencies and errors in the efficiencies are listed in Table 6.4.

Assuming that the measurements of the event yields follow a Gaussian distribution, the number of $D^+ \rightarrow \phi^0\pi^+\pi^-\pi^+$ events (N′) for a 90% confidence level calculation (N′ = N + 1.64σ) becomes 10.0 ± 3.1 [29]. For reference, the number of D^+ events (data), the associated efficiencies (MC) and the errors in these efficiencies are listed in Table 6.5.

The ratio of branching ratios for the D^+ is then calculated as,

$$\frac{\mathrm{BR}(D^+ \rightarrow \phi^0\pi^+\pi^-\pi^+)}{\mathrm{BR}(D^+ \rightarrow \phi^0\pi^+)} = \frac{N(D^+ \rightarrow \phi^0\pi^+\pi^-\pi^+)}{N(D^+ \rightarrow \phi^0\pi^+)} \cdot \frac{\epsilon(\phi^0\pi^+)}{\epsilon(\phi^0\pi^+\pi^-\pi^+)} \tag{6.3}$$

producing a result of:

$$\frac{\mathrm{BR}(D^+ \rightarrow \phi^0\pi^+\pi^-\pi^+)}{\mathrm{BR}(D^+ \rightarrow \phi^0\pi^+)} < 0.60 \text{ (90\% CL)}. \tag{6.4}$$

This result is compared to the world average in the next chapter.

Table 6.4: EFFICIENCY STUDY OF $D^+ \rightarrow \phi^0\pi^+\pi^-\pi^+$

CUT	% OF TOTAL	$\sigma(\epsilon)$ %
Master gate	89.0	0.9
Master gate and 2nd level trigger	42.7	0.6
ϕ^0 cut	40.0	0.5
Čerenkov requirements on π's	29.1	0.4
DVERT succeeds	25.6	0.4
Target cuts	22.6	0.4
CL(primary vertex) > 0.03	21.9	0.4
$L/\sigma_L > 0$	18.9	0.3
$L/\sigma_L > 5$	11.4	0.3
$L/\sigma_L > 10$	7.1	0.2
$L/\sigma_L > 12$	5.6	0.2
$L/\sigma_L > 14$	4.0	0.2

Table 6.5: EVENT COUNT AND EFFICIENCIES FOR D^+

MODE	NO. OF EVENTS (DATA)	EFFICIENCY (MC)(%)	$\sigma(\epsilon)$ %
$D^+ \rightarrow \phi^0\pi^+$	49.6 ± 9.7	16.8	0.3
$D^+ \rightarrow \phi^0\pi^+\pi^-\pi^+$	4.9 ± 3.1	5.6	0.2

CHAPTER 7

CONCLUSIONS

In this final chapter, the measurement results of this dissertation are first recapitulated. The results are then compared to the world averages and individual experiments. The chapter is concluded with some comments on these measurements.

7.1 Recapitulation of Results

The D_s^+ and D^+ lifetime results are listed in Table 7.1. In this table are listed the lifetime, decay mode and number of events. These results were obtained in a photoproduction experiment (Fermilab experiment E687) with $\langle E_\gamma \rangle \approx 220$ GeV. The branching ratio results are recapitulated in a similar manner in Table 7.2.

Table 7.1: LIFETIME RESULTS

PARTICLE	LIFETIME (ps)	MODE	NO. OF EVENTS
D_s^+	0.50±0.06±0.03	$\phi^0\pi^+$	104±15
D^+	0.90±0.13±0.05	$\phi^0\pi^+$	50±10

Table 7.2: BRANCHING RATIO RESULTS

RATIO	VALUE	NO. OF EVENTS
$\frac{BR(D_s^+ \to \phi\pi\pi\pi)}{BR(D_s^+ \to \phi\pi)}$	0.58±0.20±0.10	21±7 ($D_s^+ \to \phi^0\pi^+\pi^-\pi^+$)
$\frac{BR(D^+ \to \phi\pi\pi\pi)}{BR(D^+ \to \phi\pi)}$	< 0.60 (90% CL)	5±3 ($D^+ \to \phi^0\pi^+\pi^-\pi^+$)

7.2 Comparisons to Other Measurements

In this section, both the lifetimes and branching ratios are compared to the world averages and individual experimental results.

7.2.1 Lifetimes

In Table 7.3 is listed the world average value for the D_s^+ lifetime [6] along with the experimental results used to determine that average. Included in this table are the number of D_s^+ events and the beam characteristics of each experiment [42][43][44][14][45][46][47][48][49]. The last two entries of this table are recent D_s^+ lifetime measurements [50][51], including the results of this analysis, that are not currently included in the world average calculation.

This comparison shows that the D_s^+ lifetime measurement in this analysis is consistent with the world average. Another high statistics photoproduction experiment with $\langle E_\gamma \rangle \approx 145$ GeV (Fermilab experiment E691) listed in the table measured a D_s^+ lifetime of $0.47 \pm 0.04 \pm 0.02$ ps from a sample of 230 D_s^+ decays. These decays were roughly equal samples of $D_s^+ \to \phi^0\pi^+$ and $D_s^+ \to \overline{K^{*0}}K^+$. The lifetime measurement on a partial data set of 61 $D_s^+ \to \phi^0\pi^+$ decays produced a value of $0.49^{+0.08}_{-0.07}$ ps [52]. This result is very similar to the E687 result of 0.50 ± 0.06 ps for the $\phi^0\pi^+$ mode of the D_s^+ . (The E691 result for 38 $D_s^+ \to \overline{K^{*0}}K^+$ events was a D_s^+ lifetime

Table 7.3: D_s^+ LIFETIME MEASUREMENTS

$\tau(D_s^+)$ (ps)	EVENTS	BEAM TYPE	REF. NO.
$0.445^{+0.035}_{-0.029}$	*world average*		
$0.469^{+0.102}_{-0.086}$	54	π^-Cu (230 GeV)	42
$0.31^{+0.24}_{-0.20} \pm 0.05$		e^+e^- (E^{ee}_{cm}=29 GeV)	43
$0.56^{+0.13}_{-0.12} \pm 0.08$		e^+e^- (E^{ee}_{cm}=10 GeV)	44
$0.47 \pm 0.04 \pm 0.02$	230	photoproduction ($\langle E_\gamma \rangle \approx$ 145 GeV)	14
$0.33^{+0.10}_{-0.06}$	21	200 GeV π, K, p	45
$0.57^{+0.36}_{-0.26} \pm 0.09$	9	e^+e^- (E^{ee}_{cm}=35-44 GeV)	46
$0.47 \pm 0.22 \pm 0.05$	141	e^+e^- (E^{ee}_{cm}=10 GeV)	47
$0.35^{+0.24}_{-0.18} \pm 0.09$	17	$e^+e^- \to \phi\pi X$	48
$0.26^{+0.16}_{-0.09}$	6	ν wideband	49
$0.50 \pm 0.06 \pm 0.03$	104	photoproduction ($\langle E_\gamma \rangle \approx$ 220 GeV)	50
$0.33^{+0.12}_{-0.08} \pm 0.03$	15	photoproduction ($E_\gamma >$ 50 GeV)	51

of $0.46^{+0.10}_{-0.08}$ ps.) The E691 value of $0.47 \pm 0.04 \pm 0.02$ ps for the D_s^+ lifetime is the result for the combined sample.

Although statistically inferior in event yield, the lifetime measurement of the 50 Cabibbo-suppressed $D^+ \to \phi^0\pi^+$ decays in this analysis produced a D^+ lifetime consistent with the world average. In a similar manner as for the D_s^+ lifetime results, the world average and associated experimental results for the D^+ lifetime are presented in Table 7.4 [42][43][44][14][53][54][55][47][56][57][58][49][59][60]. Once again, the last two entries in the table are recent results [50][51] including the D^+ lifetime result of this analysis not included in the world average.

It should be noted that most of the D^+ lifetime results were measured for the Cabibbo-favored mode, $D^+ \to K^-\pi^+\pi^+$. This analysis measured the $D^+ \to \phi^0\pi^+$ lifetime only as a consistency check for the D_s^+ lifetime measurement. A D^+ lifetime result from experiment E687 using the $D^+ \to K^-\pi^+\pi^+$ mode will be available later.

Table 7.4: D^+ LIFETIME MEASUREMENTS

$\tau(D^+)$ (ps)	EVENTS	BEAM TYPE	REF. NO.
1.062 ± 0.028	*world average*		
$1.05^{+0.077}_{-0.072}$	317	π^-Cu (230 GeV)	42
$0.92^{+0.17}_{-0.13} \pm 0.16$		e^+e^- (E^{ee}_{cm}=29 GeV)	43
$1.05 \pm 0.08 \pm 0.07$		e^+e^- (E^{ee}_{cm}=10 GeV)	44
$1.090 \pm 0.03 \pm 0.025$	3000	photoproduction ($\langle E_\gamma \rangle \approx 145$ GeV)	14
$0.50^{+0.15}_{-0.10} \pm 0.19$	27	photoproduction	53
$1.12^{+0.14}_{-0.11}$	149	π^-p and pp	54
$1.09^{+0.19}_{-0.15}$	59	200 GeV π and K	55
$1.14 \pm 0.16 \pm 0.07$	526	e^+e^- (E^{ee}_{cm}=10 GeV)	47
1.09 ± 0.14	74	πBe (200 GeV)	56
$0.86 \pm 0.13^{+0.07}_{-0.03}$	48	SLAC γp (20 GeV)	57
$0.89^{+0.38}_{-0.27} \pm 0.13$	23	e^+e^- (E^{ee}_{cm}=29 GeV)	58
$1.11^{+0.44}_{-0.29}$	28	ν wideband	49
$1.06^{+0.36}_{-0.24}$	28	πBe (200 GeV)	59
$0.95^{+0.31}_{-0.19}$	70	CERN γSi	60
$0.90 \pm 0.13 \pm 0.05$	50	photoproduction ($\langle E_\gamma \rangle \approx 220$ GeV)	50
$1.03 \pm 0.08 \pm 0.06$	200	photoproduction ($E_\gamma > 50$ GeV)	51

Table 7.5: MEASUREMENTS OF $R_1 = \frac{BR(D_s^+ \to \phi^0\pi^+\pi^-\pi^+)}{BR(D_s^+ \to \phi^0\pi^+)}$

VALUE	EVENTS	EXPERIMENTAL CONDITIONS	REF. NO.
0.48 ± 0.20	*world average*		
$0.42 \pm 0.13 \pm 0.07$	19	photoproduction ($\langle E_\gamma \rangle \approx 145$ GeV)	61
$1.11 \pm 0.37 \pm 0.28$	62	e^+e^- (E_{cm}^{ee}=10 GeV)	62
$0.58 \pm 0.20 \pm 0.10$	21	photoproduction ($\langle E_\gamma \rangle \approx 220$ GeV)	

7.2.2 Branching Ratios

The world average [6] of the ratio,

$$R_1 = \frac{BR(D_s^+ \to \phi^0\pi^+\pi^-\pi^+)}{BR(D_s^+ \to \phi^0\pi^+)} \tag{7.1}$$

and the experimental results used to calculate that average are shown in Table 7.5. The last entry of that table is the measurement of R_1 produced in this analysis and not included in the world average. This result is consistent with the world average as well as with both experimental results. The details of the event samples used to calculate the world average of R_1 can be found elsewhere [61][62].

The ratio,

$$R_2 = \frac{BR(D^+ \to \phi^0\pi^+\pi^-\pi^+)}{BR(D^+ \to \phi^0\pi^+)}, \tag{7.2}$$

cannot be compared to current results but by using the following branching ratio [6],

$$D^+ \to \phi^0\pi^+ \times BR(\phi^0 \to K^+K^-) = (2.9 \pm 0.6) \times 10^{-3}, \tag{7.3}$$

one can calculate the quantity, $BR(D^+ \to \phi^0\pi^+\pi^-\pi^+) \times BR(\phi^0 \to K^+K^-)$. Using the results of this analysis, one obtains,

$$BR(D^+ \to \phi^0\pi^+\pi^-\pi^+) \times BR(\phi^0 \to K^+K^-) < 1.74 \times 10^{-3} \text{ (90\% CL)}. \tag{7.4}$$

Table 7.6: VALUES OF BR($D^+ \rightarrow \phi^0\pi^+\pi^-\pi^+$) $\times$ BR($\phi^0 \rightarrow K^+K^-$)

EXPERIMENT	LIMIT
world average	$< 1 \times 10^{-3}$
E687	$< 1.74 \times 10^{-3}$

The limit on this quantity from this analysis along with the world average value [6] are shown in Table 7.6.

7.3 Final Comments

The lifetime results of this analysis will certainly increase the world average for the D_s^+ lifetime somewhat while decreasing the statistical errors on this quantity. This continues support for the notion that the D_s^+ lifetime may possibly be longer than the D^0 lifetime. The measurement of charmed meson semi-leptonic branching ratios will also address this question.

The decay mode, $D_s^+ \rightarrow \phi^0\pi^+\pi^-\pi^+$, has been documented. Greater statistics will be needed to establish firm evidence for the Cabibbo-suppressed decay, $D^+ \rightarrow \phi^0\pi^+\pi^-\pi^+$. This may occur in the current data run of experiment E687 which will produce a data set more than five times greater than that used in this analysis.

BIBLIOGRAPHY

[1] J.J. Sakurai, Ann. Phys. 11, 1 (1960).

[2] T.H. Bauer, R.D. Spital and D.R. Yennie, Rev. Mod. Phys. 50, No. 2, 261 (1978).

[3] L.M. Jones and H.W. Wyld, Phys. Rev. D17, 759 (1978).

[4] N. Cabibbo, Phys. Rev. Lett. 10, 531 (1963).

[5] I.I. Bigi, Nucl. Phys. B7A (*Proc. Suppl.*), 318 (1989).

[6] Review of Particle Properties, Particle Data Group, Phys. Rev. B239 (1990).

[7] S.P. Rosen, Phys. Rev. Lett. 44, 4 (1980).

[8] I.I. Bigi, SLAC Publication No. 4349 (1987).

[9] A.J. Buras, J.M. Gerard, R. Rückl, Nucl. Phys. B268, 16 (1986).

[10] H. Sawayangi, K. Fujii, T. Okazaki and S. Okubo, Phys. Rev. D27, 2107, (1983).

[11] N. Bilic, B. Guberina and J. Trampetic, Nucl. Phys. B248, 261 (1984).

[12] L.L. Chen, H.Y. Cheng, Phys. Rev. D36, 137 (1987).

[13] B. Blok, M.A. Shifman, Sov. J. Nucl. Phys. 45, 135, 301, 522 (1987).

[14] J.R. Raab *et al.*, Phys. Rev. D37, 2391 (1988).

[15] S. Holmes, W. Lee and J. Wiss, Ann. Rev. Nuc. Part. Sci. 35, 397 (1985).

[16] J.R. Stanford, Ann. Rev. Nucl. Sci. 26, 151 (1976).

[17] Fermi National Accelerator Laboratory, "Tevatron II Facilities Handbook" FERMILAB (1986).

[18] J. Butler *et al.*, "Design for a New Wide-Band Neutral Beam for the Tevatron," FERMILAB note TM-963, 6020.00.

[19] J. Butler, "High Energy Photoproduction" (lecture series presented at the University of Mexico) (1989).

[20] P.L. Frabetti *et al.*, "Description and Performance of the Fermilab E687 Spectrometer" (1990) (*to be submitted to Nucl. Instr. Meth.*).

[21] C.W. Bogart, Ph.D. thesis, University of Colorado (1990) (*unpublished*).

[22] R. Yoshida, Ph.D. thesis, Northwestern University (1990) (*unpublished*).

[23] R. Gardner, Ph.D. thesis, University of Notre Dame (1991). (*unpublished*).

[24] M. Zanabria *et al.*, "Čerenkov Algorithm," E687 internal memo (1989).

[25] J. Cunningham, " Čerenkov Analysis Performance in Monte Carlo D_s^+ Events," internal memo (Notre Dame), UNDHEP89-2 (1989).

[26] J. Wiss and R. Culbertson, "DVERT," E687 internal memo (1989).

[27] K. Lingel, "ROGUE/CHAT/GENERIC," E687 internal memo (1989).

[28] L. Lyons and D.H. Saxon, Rep. Prog. Phys. 52, 1015 (1989).

[29] L. Lyons, *Statistics for Nuclear and Particle Physicists,* Cambridge University Press (1986).

[30] J. Raab, Ph.D. thesis, University of California at Santa Barbara (1987).

[31] H. Becker *et al.*, Phys. Lett. 184B, 277 (1987).

[32] R. Bailey *et al.*, Z. Phys. 28C, 357 (1985).

[33] S. Denisov *et al.*, Nucl. Phys. B61, 62 (1973).

[34] MINUIT, FERMILAB publication PM0020 (1985).

[35] J.A. Nelder and R. Mead, Comput. J. 7, 308 (1970).

[36] R. Fletcher, Comput. J. 13, 317 (1970).

[37] J.D. Jackson *et al.*, *Annual Review of Nuclear and Particle Science*, Annual Reviews Inc. (1989).

[38] C. Chen *et al.*, Phys. Rev. Lett. 62, 634 (1983).

[39] H. Albrecht *et al.*, Phys. Lett. 195, 102 (1987).

[40] M. Derrick *et al.*, Phys. Rev. Lett. 54, 2568 (1988).

[41] J. Alexander *et al.*, CLEO publication CLEO90-9, CLNS90/1003 (1990).

[42] S. Barlag *et al.*, Z. Phys. C46, 563 (1990).

[43] D. Averill *et al.*, Phys. Rev. D39, 123 (1989).

[44] H. Albrecht *et al.*, Phys. Lett. B210, 267 (1988).

[45] H. Becker *et al.*, Phys. Lett. B184, 277 (1987).

[46] W. Braunschweig *et al.*, Z. Phys. C35, 317 (1987).

[47] S.E. Csorna *et al.*, Phys. Lett. B191, 318 (1987).

[48] C. Jung *et al.*, Phys. Rev. Lett. 56, 1775 (1986).

[49] N. Ushida *et al.*, Phys. Rev. Lett. 56, 1767 (1986).

[50] P.L. Frabetti *et al.*, "Measurement of Λ_c^+ and D_s^+ Lifetimes" (1990) (*submitted to Phys. Lett. B*).

[51] M.P. Alverez, R. Barate *et al.*, Z. Phys. C47, 539 (1990).

[52] J.C. Anjos, J.A. Appel *et al.*, Phys. Rev. Lett. 58, 1818 (1987).

[53] M.I. Adamovich *et al.*, Europhys. Lett. 4, 887 (1987).

[54] M. Aguilar-Benitez *et al.*, Phys. Lett. B193, 140 (1987).

[55] S. Barlag *et al.*, Z. Phys. C37, 17 (1987).

[56] H. Palka *et al.*, Z. Phys. C35, 151 (1987).

[57] K. Abe *et al.*, Phys. Rev D33, 1 (1986).

[58] L. Gladney *et al.*, Phys. Rev. D34, 2601 (1986).

[59] R. Bailey *et al.*, Z. Phys. C28, 357 (1985).

[60] E. Albini *et al.*, Phys. Lett. 110B, 339 (1982).

[61] J.C. Anjos *et al.*, Phys. Rev. Lett. 60, 897 (1988).

[62] H. Albrecht *et al.*, Phys. Lett. 153B, 343 (1985).